Test of Lorentz Symmetry with a ^{3}He/^{129}Xe Clock-Comparison Experiment

Dissertation
zur Erlangung des Grades

"Doktor der Naturwissenschaften"

am Fachbereich Physik, Mathematik und Informatik
der Johannes Gutenberg-Universität
in Mainz

Claudia Gemmel
geboren in Idar-Oberstein

Mainz, November 2010

Datum der mündlichen Prüfung: 28.01.2011

D77

Für meine Eltern

Falls Gott die Welt geschaffen hat, war seine Hauptsorge sicher nicht, sie so zu machen, dass wir sie verstehen können.

(Albert Einstein)

Zusammenfassung

Die minimale Standard Modell Erweiterung (SME) von Kostelecký und Mitarbeitern, die die allgemeine Behandlung von CPT- und Lorentz-Invarianz-Verletzungen parametrisiert, prognostiziert siderische Modulationen von atomaren Übergangsfrequenzen aufgrund der Drehung der Erde relativ zu einem Lorentz-verletzenden Hintergrundfeld. Eine Methode zur Suche nach diesen Modulationen ist das sogenannte Uhrenvergleichsexperiment, bei dem die Frequenzen zweier Uhren verglichen werden, die sich relativ zum Fixsternhimmel bewegen. In dieser Arbeit wird ein Experiment vorgestellt, bei dem polarisierte Proben von ^{3}He und ^{129}Xe Gas in einer Glaszelle als Uhren fungieren, deren Kernspinpräzessions-Frequenzen mit Hilfe von hochempfindlichen SQUID-Sensoren detektiert werden. Die Besonderheit dieses Experimentes ist die Tatsache, dass die Spins frei präzedieren, mit transversalen Relaxationszeiten T_2^* von bis zu 4.4 h für ^{129}Xe und 14.1 h für ^{3}He.

Um auf Lorentz-verletzende Effekte empfindlich zu sein, wird der Einfluss von äußeren Magnetfeldern aufgehoben durch Bildung der gewichteten Phasendifferenz $\Delta\Phi = \Phi_{\mathrm{he}} - \frac{\gamma_{\mathrm{he}}}{\gamma_{\mathrm{xe}}}\Phi_{\mathrm{xe}}$. Die Lorentz-verletzenden SME-Parameter des Neutrons, $\tilde{b}^{\mathrm{n}}_{\mathrm{X}}$ und $\tilde{b}^{\mathrm{n}}_{\mathrm{Y}}$, werden aus einem χ^2-Fit an die Phasendifferenz-Daten von 7 Spinpräzessions-Messungen mit einer Länge von 12 bis 16 Stunden ermittelt. Die abschnittsweise definierte Fitfunktion enthält einen Sinus- und einen Kosinus-Term zur Parametrisierung der siderischen Modulation, sowie 7 Offset-Terme, 7 lineare Terme und $7 \cdot 2$ mit $T^*_{2,\mathrm{he}}$ und $T^*_{2,\mathrm{xe}}$ abfallende exponentielle Terme, die den jeweiligen Einzelmessungen zugeordnet sind. Der lineare Term in der gewichteten Phasendifferenz ist im Wesentlichen auf Abweichungen der gyromagnetischen Verhältnisse von ihren Literaturwerten aufgrund von chemischen Verschiebungen zurückzuführen, während die exponentiellen Terme von Phasenverschiebungen herrühren, die durch Entmagnetisierungsfelder in der nicht ideal sphärischen Messzelle bedingt sind.

Die aus dem χ^2-Fit ermittelte Grenze für den Parameter $\tilde{b}^{\mathrm{n}}_{\perp} = \sqrt{(\tilde{b}^{\mathrm{n}}_{\mathrm{X}})^2 + (\tilde{b}^{\mathrm{n}}_{\mathrm{Y}})^2}$ ist $3.7 \cdot 10^{-32}$ GeV, bei einem Konfidenzniveau von 95%. Dieser Wert ist nicht durch das Signal-Rausch-Verhältnis limitiert, sondern durch die starken Korrelationen zwischen den Fitparametern, die durch eine stückweise ähnliche Zeitstruktur der gewichteten Phasendifferenz und der siderischen Phasenmodulation im Fitmodell bedingt sind. Um die Korrelationen zu reduzieren und damit die Sensitivität von zukünftigen Experimenten zu erhöhen, muss die Zeitstruktur der gewichteten Phasendifferenz geändert werden, was durch eine Erhöhung der ^{129}Xe Relaxationszeit realisiert werden kann. Neben der Reduzierung der Korrelationen würde dies auch zu längeren Messzeiten und damit zu einer zusätzlichen Steigerung der Sensitivität führen.

Abstract

The minimal Standard Model Extension (SME) of Kostelecký and coworkers, which parametrizes the general treatment of CPT- and Lorentz invariance violation, predicts sidereal modulations of atomic transition frequencies as the Earth rotates relative to a Lorentz-violating background field. One method to search for these modulations is the so-called clock-comparison experiment, where the frequencies of co-located clocks are compared as they rotate with respect to the fixed stars. In this work an experiment is presented where polarized ^{3}He and ^{129}Xe gas samples in a glass cell serve as clocks, whose nuclear spin precession frequencies are detected with the help of highly sensitive SQUID sensors inside a magnetically shielded room. The unique feature of this experiment is the fact that the spins are precessing freely, with transverse relaxation times T_2^* of up to 4.4 h for ^{129}Xe and 14.1 h for ^{3}He.

To be sensitive to Lorentz-violating effects, the influence of external magnetic fields is canceled via the weighted ^{3}He/^{129}Xe phase difference, $\Delta\Phi = \Phi_{\mathrm{he}} - \frac{\gamma_{\mathrm{he}}}{\gamma_{\mathrm{xe}}}\Phi_{\mathrm{xe}}$. The Lorentz-violating SME parameters for the neutron, $\tilde{b}^{\mathrm{n}}_{\mathrm{X}}$ and $\tilde{b}^{\mathrm{n}}_{\mathrm{Y}}$, are determined out of a χ^2 fit on the phase difference data of 7 spin precession measurements of 12 to 16 hours length. The piecewise defined fit model contains a sine and a cosine term to describe the sidereal modulation, as well as 7 offset terms, 7 linear terms and $7 \cdot 2$ exponential terms decreasing with $T^*_{2,\mathrm{he}}$ and $T^*_{2,\mathrm{xe}}$, which are assigned to the respective measurement. The linear term in the weighted phase difference mainly arises from deviations of the gyromagnetic ratios from their literature values due to chemical shifts, while the exponential terms reflect the phase shifts resulting from demagnetization fields in the non-ideally spherical sample cell.

The result of the χ^2 fit constrains the parameter $\tilde{b}^{\mathrm{n}}_{\perp} = \sqrt{(\tilde{b}^{\mathrm{n}}_{\mathrm{X}})^2 + (\tilde{b}^{\mathrm{n}}_{\mathrm{Y}})^2}$ to be $< 3.7{\cdot}10^{-32}$ GeV at the 95% confidence level. This value is not limited by the signal-to-noise ratio, but by the strong correlations between the fit parameters, which are caused by a piecewise similar time structure of the weighted phase difference and the sidereal phase modulation in the fit model. To reduce the correlations and therewith improve the sensitivity of future experiments, it will be necessary to change the time structure of the weighted phase difference, which can be realized by increasing the ^{129}Xe relaxation time. Besides the reduction of the correlations, this would also lead to longer observation times and therewith an additional increase in sensitivity.

Contents

List of Figures

List of Tables

Chapter 1

Introduction: Beyond the Standard Model

The Standard Model of particle physics (SM), which is a relativistic quantum field theory, describes very well the characteristics of the particles known so far, and 3 of the 4 known fundamental interactions are included: the electromagnetic, weak and strong interaction. By contrast, the gravitation is described as a geometric property of spacetime by Einstein's General Relativity (GR), which is a classical theory. Both the SM and GR are founded on a fundamental principle called *CPT symmetry*, which means the invariance under CPT transformations, i.e., the simultaneous transformation of charge (C, interchange of particle and antiparticle), parity (P, space-inversion) and time (T, time-reversal). Another important symmetry is the *Lorentz symmetry*, i.e., the invariance under Lorentz transformations, which was first postulated by Einstein in Special Relativity in 1905. Lorentz symmetry states that the physics of any system does not change under rotations or boosts of the laboratory. One can distinguish between the *observer Lorentz transformation*, which describes rotations or boosts of the observer, and the *particle Lorentz transformation*, i.e., a transformation of the experiment with respect to an inertial frame [43]. The observer Lorentz transformation can be described as a transformation of the coordinates of the Lorentz vector x^ν into x'^μ:

$$x'^\mu = \Lambda^\mu{}_\nu \, x^\nu + a^\nu \, . \tag{1.1}$$

The particle Lorentz transformation, in contrast, can be expressed as

$$U(\Lambda, a)\Psi(x)U^{-1}(\Lambda, a) = \Psi(\Lambda x + a) \, , \tag{1.2}$$

where $\Psi(x)$ is the wave function that describes the system and $U(\Lambda, a)$ a transformation matrix that contains rotations, boosts and translations. For a system that is Lorentz-invariant, both transformations are identical and do not change the physics of the system. In Lorentz-violating theories, however, they are distinct, and only the observer Lorentz symmetry is maintained in principle, while particle transformations may be limited to a given subset of Lorentz transformations [80]. In most of the Lorentz violating theories the existence of a privileged reference frame is predicted. Nowadays we have a rather unique choice for this preferred frame: the frame where the Cosmic Microwave Background (CMB) looks isotropic (see Sec. 1.2). In principle, the experimental tests of Lorentz Symmetry are modern analogues of the Michelson-Morley experiment, i.e., they can be seen as searches for "the new aether".

Although the SM and GR are very successful in describing all physical phenomena observed so far, and no experimental evidence exists that contradicts one of these models, efforts are taken to find a more fundamental theory that gives a complete description of nature and combines quantum theory and gravity into a theory of "Quantum Gravity". While a lot of work has been done in the Quantum Gravity field during the past forty years, there exists still no completely satisfactory theory. One of the big problems is the fact that General Relativity is not only a theory of gravity, but also a theory of spacetime itself. Hence a theory of Quantum Gravity has to master the challenge of finding a description of the quantum nature of space and time.

Promising approaches for such a "theory of everything" are for example *String Theory* and *Loop Quantum Gravity*. String Theory is based on the idea that particles can be described as one-dimensional objects that are called "strings". The vibrational modes of the strings then represent, for instance, the mass or the charge of a particle. In contrast to String Theory, Loop Quantum Theory is a so-called background independent theory, i.e., the geometry of spacetime is not fixed. The main prediction is the discreteness of geometrical properties such as area and volume, which becomes important at the Planck scale [71], the energy scale where an overlap of General Relativity and quantum field theory is expected. In General Relativity, the important constants are the speed of light c and Newton's gravitational constant G, while in quantum field theory the speed of light appears together with the reduced Planck constant $\hbar$. Therefore, it is reasonable to assume that a theory of Quantum Gravity comprises all three constants c, G and $\hbar$ [4]. Using these constants one can for example define units of length and energy, the *Planck length* $l_{\mathrm{P}} = \sqrt{\frac{\hbar G}{c^3}} \approx 10^{-35}$ m and the *Planck energy* $E_{\mathrm{P}} = \sqrt{\frac{\hbar c^5}{G}} \approx 10^{20}$ GeV. Both for

String Theory and Loop Quantum Gravity, it has been shown that Lorentz violation can be induced at an energy near the Planck scale [46, 73]. But what kind of experiments have to be performed to search for Lorentz violation? At first sight, it seems to be impossible to reach this energy scale experimentally. If one wanted to build an accelerator that reaches Planck energy, it would have to be bigger than our solar system [29]. Nevertheless, there is hope that effects of Lorentz violation could be measured indirectly in experiments of extraordinary sensitivity at *low energies*. These experiments look for small shifts in the atomic energy levels that are expected to be strongly suppressed by some power of the ratio E/E_{P}, where E is a typical energy scale of the atom and E_{P} the Planck energy. In recent years, many experiments that search for Lorentz violation have been performed in different sectors. Some examples are presented in Sec. 1.3. A very successful method is the so-called clock-comparison experiment, where the frequencies of co-located clocks are compared as they rotate with respect to the fixed stars. These kind of experiment was originally proposed by Hughes [35] and Drever [24] and is therefore also called "Hughes-Drever type experiment".

The most general theoretical treatment of Lorentz violation is the so-called *minimal Standard Model Extension* (short: SME) worked out by Kostelecký and coworkers, that will be presented in the next section. In Sec. 1.2, the Cosmic Microwave Background (CMB) is considered as a preferred frame that could cause Lorentz-violating effects.

1.1 The minimal Standard Model Extension

The minimal Standard Model Extension (SME) is a general theoretical framework that includes Lorentz- and CPT-violating terms and allows to compare the results of different experiments searching for Lorentz violation [44]. The SME is a low-energy effective field theory[1] that possesses all important properties of the Standard Model, like gauge symmetry[2], renormalizability and energy-momentum conservation. It predicts small shifts in the atomic energy levels that vary periodically due to the Earth rotating relative to a Lorentz-violating background tensor field.

The Lagrangian of the SME for a particle with spin $I = \frac{1}{2}$ is the one of the Standard Model, extended by terms that violate Lorentz invariance and CPT (the Einstein summation

[1] An effective field theory is an approximate theory that only takes into account the degrees of freedom for some low-energy scale Λ, i.e., those states with $m << \Lambda$ [61].

[2] In electromagnetism, as example, the *gauge transformation* is defined by $\Phi \rightarrow \Phi' = \Phi + \frac{\partial f}{\partial t}$ and $\vec{A} \rightarrow \vec{A}' = \vec{A} - \vec{\nabla} f$, where $(\Phi, \vec{A})$ are the electromagnetic potentials. A theory whose physical predictions are not changed by such a transformation is called *gauge invariant*, and the corresponding symmetry *gauge symmetry* [49].

convention is used in the following):

$$\mathcal{L}_{SME} = \frac{1}{2} i \overline{\Psi} \Gamma_\nu \overleftrightarrow{\partial^\nu} \Psi - \overline{\Psi} M \Psi \tag{1.3}$$

$$\text{with} \quad \Gamma_\nu := \gamma_\nu + c_{\mu\nu}\gamma^\mu + d_{\mu\nu}\gamma_5\gamma^\mu + e_\nu + i f_\nu \gamma_5 + \frac{1}{2} g_{\lambda\mu\nu}\sigma^{\lambda\mu} \tag{1.4}$$

$$\text{and} \quad M := m + a_\mu \gamma^\mu + b_\mu \gamma_5 \gamma^\mu + \frac{1}{2} H_{\mu\nu}\sigma^{\mu\nu} \ . \tag{1.5}$$

Here m is the mass of the particle, γ^μ are the gamma-matrices (see, e.g., in [68]), $\gamma_5 \equiv \gamma^5 \equiv i\gamma^0\gamma^1\gamma^2\gamma^3$ and $\sigma^{\mu\nu} = \gamma^\mu\gamma^\nu - \gamma^\nu\gamma^\mu$, and a_μ, b_μ, c_μ, d_μ, e_μ, f_μ, $g_{\lambda\mu\nu}$, $H_{\mu\nu}$ are the components of the Lorentz-violating tensor-parameters. The terms with a_μ, b_μ, e_μ, f_μ, and $g_{\lambda\mu\nu}$ do violate Lorentz and CPT symmetry, while the others only violate Lorentz symmetry. For the tensor-parameters being zero, one gets again the known Lagrangian with γ_ν instead of Γ_ν and m instead of M.

From Eq. (1.3) one can derive the non-relativistic Hamilton operator $h = \hat{h} + \delta h$, where $\hat{h}$ is the usual Fouldy-Wouthuysen-Hamiltonian and δh the Lorentz-violating perturbation term:

$$\begin{aligned}
\delta h = {} & (a_0 - m c_{00} - m e_0) + (-b_\mathrm{j} + m d_{\mathrm{j}0} - \tfrac{1}{2} m \epsilon_{\mathrm{jkl}} g_{\mathrm{kl}0} + \tfrac{1}{2}\epsilon_{\mathrm{jkl}} H_{\mathrm{kl}})\sigma^\mathrm{j} + [-a_\mathrm{j} + m(c_{0\mathrm{j}} + c_{\mathrm{j}0}) + m e_\mathrm{j}]\tfrac{p_\mathrm{j}}{m} \\
& + [b_0 \delta_{\mathrm{jk}} - m(d_{\mathrm{kj}} + d_{00}\delta_{\mathrm{jk}}) - m\epsilon_{\mathrm{klm}}(\tfrac{1}{2} g_{\mathrm{mlj}} + g_{\mathrm{m}00}\delta_{\mathrm{jl}}) - \epsilon_{\mathrm{jkl}} H_{\mathrm{l}0}]\tfrac{p_\mathrm{j}}{m}\sigma^k \\
& + [m(-c_{\mathrm{jk}} - \tfrac{1}{2} c_{00}\delta_{\mathrm{jk}})]\tfrac{p_\mathrm{j} p_\mathrm{k}}{m^2} + \{[m(d_{0\mathrm{j}} + d_{\mathrm{j}0} - \tfrac{1}{2}(b_\mathrm{j} + m d_{\mathrm{j}0} + \tfrac{1}{2} m \epsilon_{\mathrm{jmn}} g_{\mathrm{mn}0} + \tfrac{1}{2}\epsilon_{\mathrm{jmn}} H_{\mathrm{mn}})]\delta_{\mathrm{kl}} \\
& + \tfrac{1}{2}(b_\mathrm{l} + \tfrac{1}{2} m \epsilon_{\mathrm{lmn}} g_{\mathrm{mn}0})\delta_{\mathrm{jk}} - m\epsilon_{\mathrm{jlm}}(g_{\mathrm{m}0\mathrm{k}} + g_{\mathrm{mk}0}\}\tfrac{p_\mathrm{j} p_\mathrm{k}}{m^2}\sigma^\mathrm{l} \, .
\end{aligned} \tag{1.6}$$

Here σ^j are the Pauli-matrices[3], p_j the momenta components, and δ_{ij} the Kronecker delta with $\delta_{\mathrm{ij}} = 1$ (0) for $i = j$ ($i \neq j$). The Levi-Civita symbol ϵ_{jkl} is defined as

$$\epsilon_{\mathrm{jkl}} = \begin{cases} 1 & \text{for i, j, k cyclical,} \\ -1 & \text{for i, j, k counter-cyclical,} \\ 0 & \text{else.} \end{cases}$$

The clock-comparison experiments are sensitive to the second term in Eq. (1.6), as will be seen later. To get the Hamiltonian for an atom, the perturbation Hamiltonians for every

[3]The Pauli-matrices are given by:

$$\sigma^1 = \begin{pmatrix} 0 & 1 \\ 1 & 0 \end{pmatrix}, \quad \sigma^2 = \begin{pmatrix} 0 & -i \\ i & 0 \end{pmatrix}, \quad \sigma^3 = \begin{pmatrix} 1 & 0 \\ 0 & -1 \end{pmatrix}$$

single particle (electrons, neutrons and protons) have to be added:

$$h' = \sum_w \sum_{N=1}^{N_w} \delta h_{w,N} \,, \tag{1.7}$$

where w stands for the proton, neutron or electron and N_w is the number of each particle.

The Lorentz-violating energy shift

The perturbative energy shift of the state $|F, m_\mathrm{F}\rangle$ is maintained by taking the expectation value of the perturbative Hamiltonian, $E_\mathrm{LV} = \langle F, m_\mathrm{F}| \, h' \, |F, m_\mathrm{F}\rangle$, where F is the quantum number of the total momentum $\vec{F} = \vec{I} + \vec{J}$ with the nuclear spin $\vec{I}$ and the electronic spin $\vec{J}$ ($\vec{J} = 0$ for ^{3}He and ^{129}Xe). In the calculation of the energy E_LV some terms vanish due to the properties of h' and of the states $|F, m_\mathrm{F}\rangle$. Furthermore, it follows from the Wigner-Eckart theorem that for particles like ^{3}He and ^{129}Xe with $F = I = \frac{1}{2}$ one can neglect the energy shifts that arise from an expectation value of a tensor of rank 2 (quadrupole shift). So the leading-order Lorentz-violating energy shift for an atom W with $F = I = \frac{1}{2}$ ($J = 0$) is given by

$$E_\mathrm{LV} = \langle F, m_\mathrm{F}| \, h' \, |F, m_\mathrm{F}\rangle = \hat{m}_\mathrm{F} E_\mathrm{d}^\mathrm{W} \,, \tag{1.8}$$

$$\text{where} \quad \hat{m_\mathrm{F}} := \frac{m_\mathrm{F}}{F} = \pm 1 \,, \tag{1.9}$$

and the dipolar energy shift

$$E_\mathrm{d}^\mathrm{W} = \sum_w (\beta_w \cdot \tilde{b}_3^w + \delta_w \cdot \tilde{d}_3^w + \kappa_w \cdot \tilde{g}_d^w) \,. \tag{1.10}$$

The (dimensionless) coefficients β_w, δ_w and κ_w appearing in Eq. (1.10) are linear combinations of expectation values of certain operators of the perturbation Hamiltonian (1.6) in the special state $|F, F\rangle$:

$$\beta_\mathrm{w} := -\sum_{\mathrm{N}=1}^{\mathrm{N_w}} \langle [\sigma^3]_{\mathrm{w,N}} \rangle \,, \tag{1.11}$$

$$\delta_\mathrm{w} := \frac{1}{m_\mathrm{w}^2} \sum_{\mathrm{N}=1}^{\mathrm{N_w}} \langle [p_3 \, p_\mathrm{j} \, \sigma^\mathrm{j}]_{\mathrm{w,N}} \rangle \,, \tag{1.12}$$

$$\kappa_\mathrm{w} := \frac{1}{2m_\mathrm{w}^2} \sum_{\mathrm{N}=1}^{\mathrm{N_w}} \langle [p_3 \, p_\mathrm{j} \, \sigma^\mathrm{j} - p_\mathrm{j} \, p_\mathrm{j} \, \sigma^3]_{\mathrm{w,N}} \rangle \,. \tag{1.13}$$

The subscript w, N on each operator means that it acts on particle N of type w. The quantities with tildes in Eq. (1.10) are combinations of the parameters for Lorentz violation appearing in (1.6),

$$\tilde{b}_3^{\mathrm{w}} := b_3^{\mathrm{w}} - m_{\mathrm{w}}\, d_{30}^{\mathrm{w}} + m_{\mathrm{w}}\, g_{120}^{\mathrm{w}} - H_{12}^{\mathrm{w}}\,, \tag{1.14}$$

$$\tilde{d}_3^{\mathrm{w}} := m_{\mathrm{w}}\, d_{03}^{\mathrm{w}} + \frac{1}{2} m_{\mathrm{w}}\, d_{30}^{\mathrm{w}} - \frac{1}{2} H_{12}^{\mathrm{w}}\,, \tag{1.15}$$

$$\tilde{g}_d^{\mathrm{w}} := m_{\mathrm{w}}\, (g_{102}^{\mathrm{w}} - g_{201}^{\mathrm{w}} + g_{120}^{\mathrm{w}}) - b_3^{\mathrm{w}}\,. \tag{1.16}$$

Now one can further simplify the above expressions with the help of the Schmidt nuclear shell model [55], where for ^{3}He as well as for ^{129}Xe the valence neutron is assumed to carry the entire spin of the nucleus. Thus for Eq. (1.10) only the neutron term remains:

$$E_{\mathrm{d}}^{\mathrm{n}} = \beta_{\mathrm{n}} \cdot \tilde{b}_3^{\mathrm{n}} + \delta_{\mathrm{n}} \cdot \tilde{d}_3^{\mathrm{n}} + \kappa_{\mathrm{n}} \cdot \tilde{g}_d^{\mathrm{n}}\,. \tag{1.17}$$

Moreover, if one assumes similar sizes of the Lorentz-violating parameters $\tilde{b}_3^{\mathrm{n}}$, $\tilde{d}_3^{\mathrm{n}}$ and $\tilde{g}_3^{\mathrm{n}}$, one can show that the second and third term of (1.17) are strongly suppressed compared to the first term. This can be seen when the coefficients β_{n}, δ_{n} and κ_{n} are calculated according to Eq. (1.11)-(1.13). By assuming that $\langle {p_1}^2 \rangle \approx \langle {p_2}^2 \rangle \approx \langle {p_3}^2 \rangle = \frac{1}{3}\langle p^2 \rangle$, we get

$$\beta_{\mathrm{n}} = -1\,, \quad \delta_{\mathrm{n}} = \frac{1}{3}\frac{\langle p^2 \rangle_{\mathrm{n}}}{m_{\mathrm{n}}^2} \quad \text{and} \quad \kappa_{\mathrm{n}} = -\frac{1}{3}\frac{\langle p^2 \rangle_{\mathrm{n}}}{m_{\mathrm{n}}^2}\,. \tag{1.18}$$

The mean quadratical momentum component $\langle p^2 \rangle_{\mathrm{n}}$ can be estimated with the help of Heisenberg's uncertainty principle $\Delta p \cdot \Delta x \approx \hbar$. With the size of the nucleus of some fm we get a momentum of $\Delta p = \mathcal{O}\,(100\,\mathrm{MeV})$. Together with the neutron mass of $m_{\mathrm{n}} \approx 1000\,\mathrm{MeV}$, one can see that $\frac{\langle p^2 \rangle_{\mathrm{n}}}{m_{\mathrm{n}}^2}$ is in the order of 10^{-2}. For this reason, the second and third term of Eq. (1.17) will be neglected in the following.

Temporal dependence of the parameters

The parameters for Lorentz violation from Eq. (1.11)-(1.13) are defined in the laboratory frame ($\hat{x}$, $\hat{y}$, $\hat{z}$). Since this frame rotates with the Earth, the components of the parameters vary in time with the periodicity of the Earth's rotation, $\Omega_{\mathrm{E}} \approx 2\pi/(23\text{ h }56\text{ min})$. The time dependence of the energy shift of Eq. (1.8) can be determined by introducing a nonrotating frame ($\hat{X}$, $\hat{Y}$, $\hat{Z}$), with the $\hat{Z}$ axis being equal to the Earth's rotation axis. The laboratory and the nonrotating frame are shown in Fig. 1.1 (for better visualization the origin of ($\hat{x}$, $\hat{y}$, $\hat{z}$) has

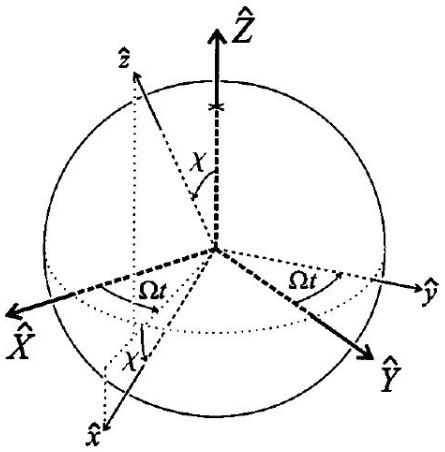

Figure 1.1: Laboratory ($\hat{x}$, $\hat{y}$, $\hat{z}$) and nonrotating frame ($\hat{X}$, $\hat{Y}$, $\hat{Z}$) to derive the temporal dependence of the parameters in the SME.

been set to the center of the Earth, so that it coincides with the origin of the nonrotating frame). In terms of equatorial coordinates (see Sec. 1.2), the $\hat{Z}$ axis has a declination of 90°, while $\hat{X}$ has both declination and right ascension 0°, and $\hat{Y}$ declination 0° and right ascension 90°. If the precession of the Earth's axis is neglected, this coordinate frame is constant in time. For the laboratory frame, the $\hat{z}$ axis corresponds to the quantization axis of the atoms in the specific experiment. A nonzero signal in a clock-comparison experiment requires a nonzero angle χ between $\hat{z}$ and $\hat{Z}$, i.e., the Earth's rotation axis. The time $t = 0$ is chosen such that $\hat{z}(t = 0)$ lies in the first quadrant of the $\hat{X} - \hat{Z}$ plane, while $\hat{x}$ lies in the plane spanned by $\hat{z}$ and $\hat{Z}$. The (non-relativistic) transformation between both coordinate systems is given by:

$$\begin{pmatrix} \hat{x} \\ \hat{y} \\ \hat{z} \end{pmatrix} = T \begin{pmatrix} \hat{X} \\ \hat{Y} \\ \hat{Z} \end{pmatrix} \quad \text{with } T = \begin{pmatrix} \cos\chi\cos(\Omega_{\mathrm{E}}t) & \cos\chi\sin(\Omega_{\mathrm{E}}t) & -\sin\chi \\ -\sin(\Omega_{\mathrm{E}}t) & \cos(\Omega_{\mathrm{E}}t) & 0 \\ \sin\chi\cos(\Omega_{\mathrm{E}}t) & \sin\chi\sin(\Omega_{\mathrm{E}}t) & \cos\chi \end{pmatrix} . \quad (1.19)$$

Now one can introduce the nonrotating-frame analogue of the parameter $\tilde{b}_3^{\mathrm{n}}$ in Eq. (1.14),

$$\tilde{b}_{\mathrm{J}} := b_{\mathrm{J}} - m \cdot d_{\mathrm{J0}} + \frac{1}{2} m \cdot \epsilon_{\mathrm{JKL}} \cdot g_{\mathrm{KLO}} - \frac{1}{2} m \cdot \epsilon_{\mathrm{JKL}} \cdot H_{\mathrm{KL}} , \quad (1.20)$$

where ϵ_{JKL} is again the Levi-Civita symbol. The spatial indices here are denoted by $J = X, Y, Z$ and the time index is denoted by 0. Now the transformation matrix (1.19)

can be used to determine the time dependence of the parameter $\tilde{b}_3^{\mathrm{n}}$ in the laboratory frame:

$$\tilde{b}_3^{\mathrm{n}} = \tilde{b}_{\mathrm{Z}} \cdot \cos\chi + \tilde{b}_{\mathrm{X}} \cdot \sin\chi \cos(\Omega_{\mathrm{E}} t) + \tilde{b}_{\mathrm{Y}} \cdot \sin\chi \sin(\Omega_{\mathrm{E}} t)\,. \tag{1.21}$$

The energy shift then becomes

$$E_{\mathrm{LV}} = \langle F, m_{\mathrm{F}} |\, h' \,| F, m_{\mathrm{F}} \rangle = E_0 + E_{1\mathrm{X}} \cos(\Omega_{\mathrm{E}} t) + E_{1\mathrm{Y}} \sin(\Omega_{\mathrm{E}} t) \tag{1.22}$$

$$\text{with} \quad E_{1\mathrm{X}}^{\mathrm{n}} \approx \hat{m}_{\mathrm{F}} \sin\chi(\beta_{\mathrm{n}} \tilde{b}_X^{\mathrm{n}}) \quad \text{and} \quad E_{1\mathrm{Y}}^{\mathrm{n}} \approx \hat{m}_{\mathrm{F}} \sin\chi(\beta_{\mathrm{n}} \tilde{b}_Y^{\mathrm{n}})\,, \tag{1.23}$$

where $\hat{m}_{\mathrm{F}}$ is given in Eq. (1.9) and β_{n} in Eq. (1.11). In our case, for $F = I = \frac{1}{2}$, we have $\hat{m}_{\mathrm{F}} = \pm 1$ and $\beta_{\mathrm{n}} = -1$, and hence

$$E_{1\mathrm{X}}^{\mathrm{n}}(m_{\mathrm{F}} = \pm\frac{1}{2}) = \mp \sin\chi\, \tilde{b}_{\mathrm{X}}^{\mathrm{n}}\,, \tag{1.24}$$

$$E_{1\mathrm{Y}}^{\mathrm{n}}(m_{\mathrm{F}} = \pm\frac{1}{2}) = \mp \sin\chi\, \tilde{b}_{\mathrm{Y}}^{\mathrm{n}}\,. \tag{1.25}$$

The Lorentz violating frequency shift corresponding to the difference between the energy levels with $m_{\mathrm{F}} = \pm\frac{1}{2}$ then becomes

$$\begin{aligned} h\nu_{\mathrm{LV}} = \Delta E_{\mathrm{LV}} &= \left| \langle\, 1/2, +1/2 \,|\, h' \,|1/2, +1/2\,\rangle - \langle\, 1/2, -1/2 \,|\, h' \,|1/2, +1/2\,\rangle \right| \\ &= |E_0 - \sin\chi\, \tilde{b}_{\mathrm{X}}^{\mathrm{n}}\, \cos(\Omega_{\mathrm{E}} t) - \sin\chi\, \tilde{b}_{\mathrm{Y}}^{\mathrm{n}}\, \sin(\Omega_{\mathrm{E}} t) \\ &\quad - (E_0 + \sin\chi\, \tilde{b}_{\mathrm{X}}^{\mathrm{n}}\, \cos(\Omega_{\mathrm{E}} t) + \sin\chi\, \tilde{b}_{\mathrm{Y}}^{\mathrm{n}}\, \sin(\Omega_{\mathrm{E}} t))| \\ &= 2\, \sin\chi\, \tilde{b}_{\mathrm{X}}^{\mathrm{n}}\, \cos(\Omega_{\mathrm{E}} t) + 2\, \sin\chi\, \tilde{b}_{\mathrm{Y}}^{\mathrm{n}}\, \sin(\Omega_{\mathrm{E}} t)\,. \end{aligned} \tag{1.26}$$

If we now define the Lorentz-violating frequencies ν_{X} and ν_{Y} as the amplitudes of the cosine/sine part of the sidereal frequency variation,

$$\nu_{\mathrm{LV}} =: \nu_{\mathrm{X}}\, \cos(\Omega_{\mathrm{E}} t)\, + \nu_{\mathrm{Y}}\, \sin(\Omega_{\mathrm{E}} t)\, = \frac{2\, \sin\chi}{h}\, (\tilde{b}_{\mathrm{X}}^{\mathrm{n}}\, \cos(\Omega_{\mathrm{E}} t) + \tilde{b}_{\mathrm{Y}}^{\mathrm{n}}\, \sin(\Omega_{\mathrm{E}} t))\,, \tag{1.27}$$

we get a relation between $\nu_{\mathrm{X(Y)}}$ and the Kostelecký parameters $\tilde{b}_{\mathrm{X(Y)}}^{\mathrm{n}}$,

$$\nu_{\mathrm{X(Y)}} = \frac{2 \sin\chi}{h}\, \tilde{b}_{\mathrm{X(Y)}}^{\mathrm{n}}\,. \tag{1.28}$$

This equation is used later in Chap. 4.4 to determine a limit for the parameters for Lorentz-violation out of the ^{3}He/^{129}Xe clock-comparison experiment.

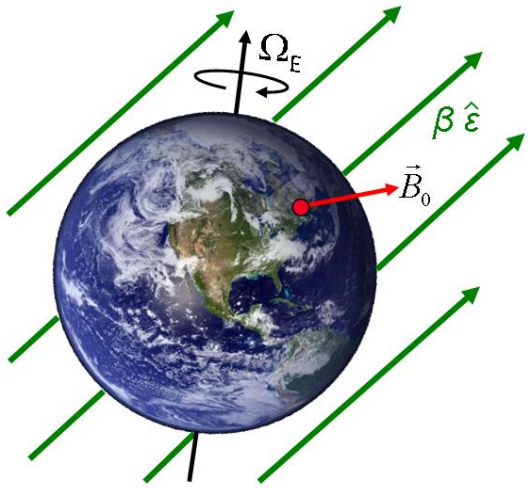

Figure 1.2: The Earth and with it the magnetic field $\vec{B}_0$ in the laboratory rotate around the axis Ω_E with respect to a Lorentz-violating background field $\beta\hat{\epsilon}$.

1.2 The Cosmic Microwave Background

To make the Lorentz-violating coupling a bit more descriptive, one can write the energy shift that occurs in the Standard Model Extension as

$$E_{\mathrm{LV}} = -\tilde{b}_{\mathrm{J}} \cdot \sigma^{\mathrm{J}} = -\vec{\tilde{b}} \cdot \vec{\sigma} = -\beta\ \vec{\sigma} \cdot \hat{\epsilon}\ , \tag{1.29}$$

where $\vec{\tilde{b}} = \beta\hat{\epsilon}$ is the hypothetical, Lorentz-violating background field with magnitude β and the fixed direction $\hat{\epsilon}$ in space. So the coupling of the spin $\vec{\sigma}$ to the background field is analog to the Zeeman coupling of a spin to a magnetic field. This coupling is illustrated in Fig. 1.2: The spin quantization axis is given by the magnetic field $\vec{B}_0$, which rotates about Ω_{E} together with the Earth relative to the background field. So the angle between $\vec{B}_0$ and $\hat{\epsilon}$ changes with the period of the Earth's rotation. Then the energy difference ΔE_{LV} and the corresponding frequency ν_{LV} due to a spin coupling to $\vec{\tilde{b}}$ is given by

$$\Delta E_{\mathrm{LV}} = h\nu_{\mathrm{LV}} = E_{\mathrm{LV}}(m_{\mathrm{F}} = +\frac{1}{2}) - E_{\mathrm{LV}}(m_{\mathrm{F}} = -\frac{1}{2}) = 2\beta\cos(\Omega_{\mathrm{E}}t + \Phi)\ . \tag{1.30}$$

Such a privileged reference frame as defined by the direction $\hat{\epsilon}$ is given by the Cosmic Microwave Background (CMB), whose dipole anisotropy describes a preferred direction in space. In Fig. 1.3 the dipolar dependence of the temperature distribution in space due to

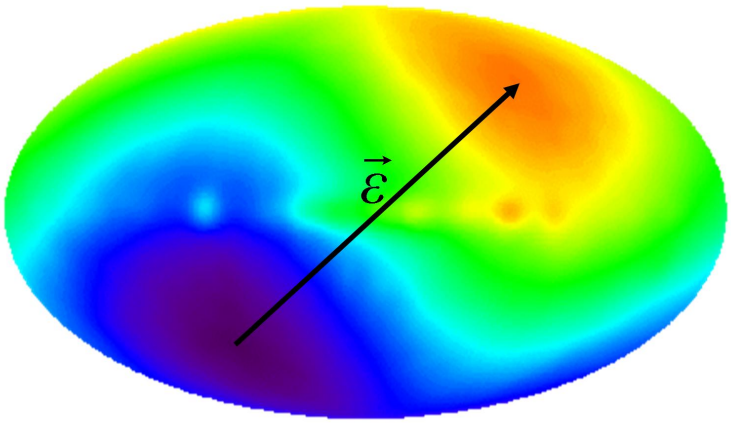

Figure 1.3: Dipole anisotropy of the cosmic microwave background [78].

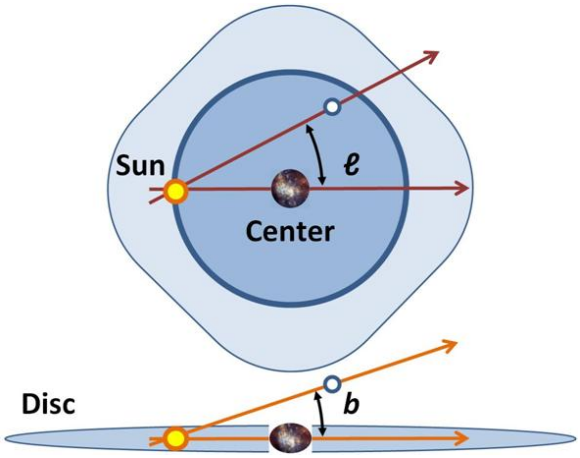

Figure 1.4: Galactic coordinate system [82]: It is aligned in the plane of the Milky Way galaxy ("Disc"), and the origin is the Sun. The coordinates are given as the longitude l, which is the azimuth angle in the galactic plane that lies between 0°(the direction to the galactic center) and 360°, and the latitude b that lies between -90° (at the South Galactic Pole) and +90° (at the North Galactic Pole).

the movement of the solar system relative to the CMB is shown. If the background field is assumed to point into the direction of the CMB dipole, the expected phase developing of a possible signal due to Lorentz violation can be calculated. In the *galactic coordinate system* which is centered on the sun and aligned in the plane of the Milky Way galaxy [76], the dipole direction is given by $(l, b) = (264.31° \pm 0.17°,\ 48.05° \pm 0.10°)$ [72], where l is the longitude and b the latitude (see Fig. 1.4).

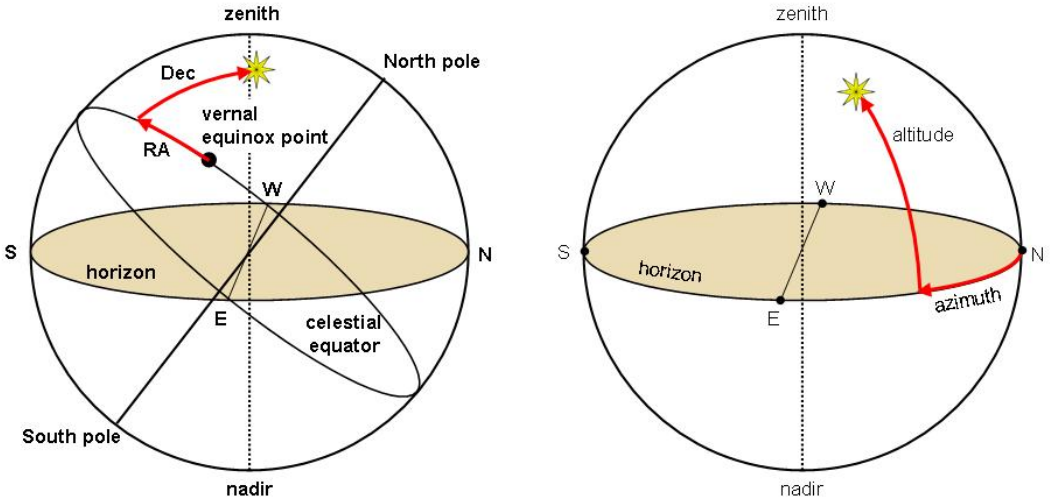

Figure 1.5: *Left*: The equatorial coordinate system. The Earth's equatorial plane and rotation axis serve as references that are projected onto the celestial sphere. The origin lies in the vernal equinox point. The coordinates are the right ascension RA, which is the azimuth angle in the equatorial plane and lies between 0 h and 24 h, and the declination Dec, which is the elevation angle between -90° and +90°. *Right*: The horizontal coordinate system. The reference plane is the local horizon on the Earth's surface; the direction is given by the azimuth az, which is 0° at the north direction, and the altitude al, which is +90° at the zenith and -90° at the nadir. The outer circle going through the north pole, the zenith, the south pole and the nadir is called meridian.

Equatorial coordinate system and sidereal time

The galactic coordinates can be transferred into the *equatorial coordinate system*, where the Earth's equatorial plane and rotation axis serve as references that are projected onto the celestial sphere (see Fig. 1.5, left side). The coordinates are the declination Dec, which is the elevation angle between -90° and +90°, and the right ascension RA, which is the azimuth angle in the equatorial plane. RA is measured relative to the apparent location of the center of the Sun at the moment of the March equinox, a position known as the *vernal equinox point*. The right ascension is often expressed in *sidereal hours* (0 h to 24 h) instead of degrees, because an apparent rotation of the equatorial coordinate system takes 24 hours of sidereal time to complete, which corresponds to 23 hours, 56 minutes and 4.091 seconds of SI time. The direction given by the vernal equinox point, i.e., RA 0° or 0 h, corresponds to the $\hat{X}$-axis in the coordinate system shown in Fig. 1.1. As the position of the vernal equinox point on the celestial sphere changes slightly due to

the precession of the Earth's axis, one has to give a reference time together with this system. Commonly used is the time known as J2000, which is 12:00 UT (Universal Time, earlier: Greenwich Mean Time) on 2000 January 1. By use of Ref. [54] the direction of the CMB dipole in equatorial coordinates is given as (RA 11 h 11 min 57 s, Dec -7° 13' 14").

To get the angle α between the CMB dipole and the magnetic field of our experiment, the dipole coordinates have to be converted into the *horizontal coordinate system*, where the reference plane is given by the Earth's local horizon. The coordinates are defined by the azimuth angle az, which is 0° at north direction, and the altitude al, which is +90° at the zenith and -90° at the nadir (see Fig. 1.5, right side). Given in this reference system, the direction of the CMB dipole depends on the point in time and the position on the Earth's surface. For our experiment the position is the BMSR-2 in Berlin, which lies at northern latitude 52.516°= 52° 31' and eastern longitude 13.320° = 13° 19' [79]. With the help of Ref. [20] one can now determine the direction of the CMB dipole in horizontal coordinates at BMSR-2 for certain points in time. Then the angle α can be calculated as

$$\cos(\alpha) = \cos(az_{\mathrm{CMB}} - az_{\mathrm{B}}) \cdot \cos(al_{\mathrm{CMB}}) \ ,$$

where az_{CMB} and $az_{\mathrm{B}} = 28°$ are the azimuth of the CMB dipole and the magnetic field, respectively, and al_{CMB} is the altitude of the CMB dipole. The altitude of the field is zero, because the field vector lies inside the horizontal plane. The angle was calculated for a period of 24 hours at intervals of 2 hours, starting at $t_{0,1}$, the beginning of the first one of the clock-comparison measurements that are described in Chap. 4. The cosine of α is shown in Fig. 1.6. One can see that the CMB dipole and the field are directed such that the sensitivity for an anomalous coupling between spins and CMB background is about 80% of the maximum possible sensitivity.

1.3 Experimental searches for Lorentz violation

The sidereal modulations of atomic transition frequencies predicted by the SME for the case of Lorentz violation could be measured in high-precision experiments at the low-energy scale. A famous experiment that can be interpreted as a search for Lorentz violation was the Michelson-Morley experiment performed in 1887, that was looking for a change in the speed of light under rotation [51]. The aim of this experiment was to prove the existence of the ether. Michelson and Morley measured the speed of light via interference of two light beams passing through two perpendicular arms of a rotatable interferometer (the Michelson interferometer). Today, modern Michelson-Morley-type experiments exist (see, for example,

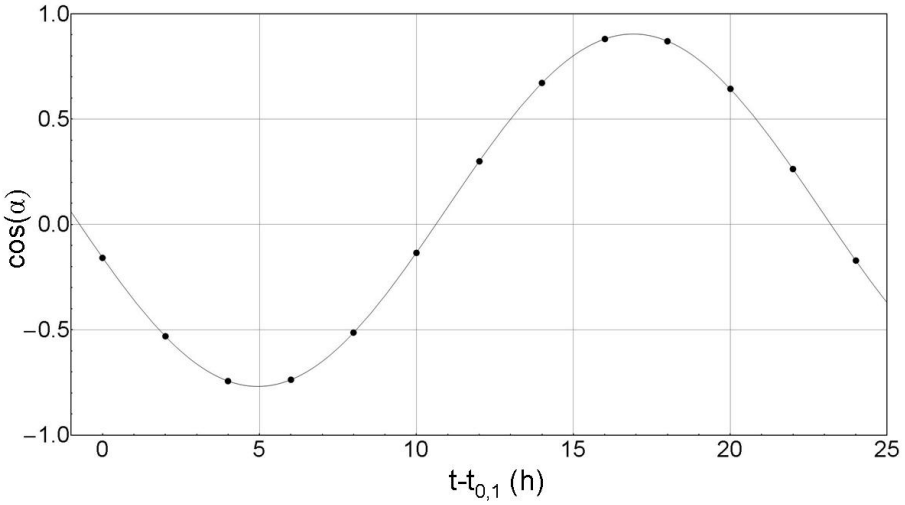

Figure 1.6: Cosine of the angle α between the spin quantization axis (magnetic field $\vec{B}_0$) and the CMB dipole direction $\hat{\epsilon}$ over a period of 24 hours (see Fig. 1.2). $t_{0,1}$ is the starting time of the first one of the clock-comparison measurements described in Chap. 4, i.e., on 2009 March 21 at 21:25 GMT (22:25 Berlin time).

[31]), which measure the resonance frequency of a cavity as its orientation changes with respect to a stationary frequency standard. These experiments are sensitive to the SME parameters for the photon.

The experiment presented in this work belongs to the group of clock-comparison experiments: the spin precession frequencies of ^{3}He and ^{129}Xe nuclear spins are compared while the spin quantization axis rotates together with the Earth in respect to the fixed stars. Therefore, both noble gases are filled into a 6 cm diameter spherical glass cell, and the free Larmor precession is detected with the help of SQUID[4] sensors inside a magnetically shielded room, the BMSR-2 (**B**erlin **M**agnetically **S**hielded **R**oom) at the Physikalisch-Technische Bundesanstalt (PTB) in Berlin. By measuring at low pressures (in the order of mbar) and low magnetic field, it is possible to reach transverse spin relaxation times of several hours (see Chap. 2.5.2), and hence to observe the free precession signal over a period of approximately 1 day. As the weighted ^{3}He/^{129}Xe frequency (or phase) difference, $\Delta\omega = \omega_{\mathrm{he}} - \frac{\gamma_{\mathrm{he}}}{\gamma_{\mathrm{xe}}}\omega_{\mathrm{xe}}$, is considered, the influence of external magnetic fields is canceled, and one gets sensitive to possible Lorentz-violating effects concerning the neutron. Other examples for clock-comparison experiments, that are sensitive to neutron and proton parameters

[4]SQUIDs (**S**uperconducting **Qu**antum **I**nterference **D**evices) are highly sensitive detectors for magnetic flux changes.

of the SME, are the ^{3}He/^{129}Xe maser and the K-^{3}He co-magnetometer that will be presented in Sec. 1.3.1 and 1.3.2. Furthermore, the most sensitive measurement so far in the electron sector is introduced in Sec. 1.3.3.

1.3.1 ^{3}He/^{129}Xe maser

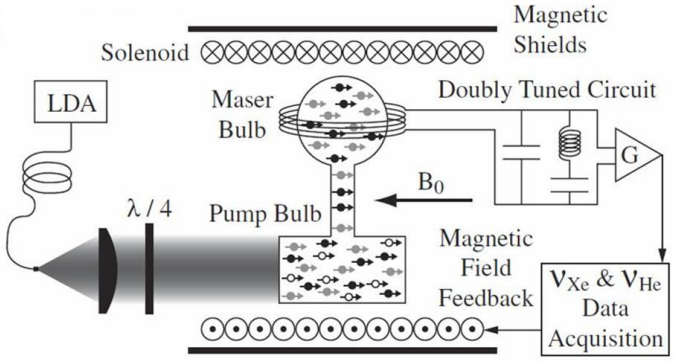

Figure 1.7: Setup of the ^{3}He/^{129}Xe maser experiment [5].

The Walsworth group at Harvard University uses ^{3}He and ^{129}Xe gas in a clock-comparison experiment to constrain the SME parameters for the neutron [7]. The difference to our experiment is that they do not measure free spin precession, but operate ^{3}He and ^{129}Xe as a two-species maser. The setup is shown in Fig. 1.7: The dual noble-gas maser sits inside a homogeneous magnetic field of ≈ 3 Gauss that is provided by a solenoid, and is surrounded by a three-layer magnetic shielding. The maser cell consists of two glass chambers, which are named the pump and the maser bulb, and is filled with ^{129}Xe at a pressure of about 100-200 Torr, ^{3}He at about 1100-2400 Torr and N_2 as buffer gas at 60-100 Torr. In the pump bulb the gases are spin polarized by means of spin-exchange optical pumping (SEOP, see Chap. 2.2.2) with Rubidium. The D_1 transition of Rubidium is excited by a 795 nm circularly polarized laser beam. The polarized gas atoms then diffuse into the maser bulb, where maser oscillations are maintained with the help of two resonant circuits for the ^{3}He and ^{129}Xe Larmor frequencies of ≈ 10 kHz and ≈ 3.5 kHz, respectively. The resonant coils provide positive feedback to these transitions, so that the ^{3}He and ^{129}Xe spin ensembles perform continuous and independent maser oscillations. The static magnetic field is stabilized via active feedback by phase-locking the ^{129}Xe maser to a stable frequency standard, while the free-running ^{3}He maser serves as a sensitive probe for Lorentz-violating interactions. Therefore, the relative phases and Larmor frequencies of both masers are monitored while the

spin quantization axis rotates about the Earth's axis with respect to a hypothetical Lorentz-violating background field. The expected sidereal variation according to the Standard Model Extension takes the from

$$\delta\nu_{\mathrm{He}} = \delta\nu_{\mathrm{X}} \cos(\Omega_{\mathrm{E}} t) + \delta\nu_{\mathrm{Y}} \sin(\Omega_{\mathrm{E}} t) \ ,$$

where Ω_{E} is the Earth's rotation frequency, and $\delta\nu_{\mathrm{X(Y)}}$ represents the effect of the Lorentz-violating couplings on the ^{3}He maser frequency (with the ^{129}Xe maser acting as co-magnetometer) and is proportional to the SME parameter $\tilde{b}^{\mathrm{n}}_{\mathrm{X(Y)}}$. In total, 90 days of data that was taken during 3 measurement periods was used to extract a limit for $\tilde{b}^{\mathrm{n}}_{\mathrm{X(Y)}}$. For each one-sidereal day run a model that contained at least 7 free parameters was fitted to the data using a linear least-squares routine. Besides the Lorentz-violating terms of the above equation, the model consisted of a phase offset, a linear term, as well as quadratic and maser amplitude-correlated phase drifts. The total weighted means and uncertainties were then formed from all data sets. These values were used to extract the mean Lorentz-violating frequency shift of $R \equiv \sqrt{\delta\nu_{\mathrm{X}}^2 + \delta\nu_{\mathrm{Y}}^2} = 53 \pm 45$ nHz, which corresponds to $\tilde{b}^{\mathrm{n}}_{\mathrm{J}} \equiv \sqrt{(\tilde{b}^{\mathrm{n}}_{\mathrm{X}})^2 + (\tilde{b}^{\mathrm{n}}_{\mathrm{Y}})^2} = (6.4 \pm 5.4) \cdot 10^{-32}$ GeV [6], where the error is the 1-σ error.

1.3.2 K-^{3}He Clock-comparison experiment

The so far most sensitive experiment that constrains the Lorentz violating parameter $\tilde{b}_{\mathrm{J}}$ for the neutron and the proton is accomplished at the group of M.V. Romalis at Princeton university [14]. In this experiment, K and ^{3}He atoms are used in a co-magnetometer configuration. The setup is shown in Fig. 1.8: The whole apparatus is positioned inside an evacuated bell jar which sits on a rotary platform. The heart of the experiment is the 2.4 cm diameter spherical cell filled with 9.4 amagats of ^{3}He, 29 Torr of N_2 as buffer gas, and a drop of K metal. A circularly polarized laser beam optically pumps the K atoms, which then transfer their polarization to the ^{3}He atoms via spin-exchange collisions. The cell sits inside a vacuum chamber and is magnetically and thermally shielded. Outside the shielding the optical elements are arranged. An applied magnetic field in z-direction, i.e., coaxial with the polarized spins, can be tuned such that it cancels the magnetic field experienced by the K atoms due to the ^{3}He magnetization and external fields. Hence the K magnetometer operates at quasi zero field (at the "compensation point"), and is therefore sensitive to anomalous non-magnetic spin interactions. The measured quantity in this experiment is the polarization of the K atoms in x direction $P^{\mathrm{e}}_{\mathrm{x}}$, which is detected optically with the help of a probe laser in x-direction. At the compensation point it is to a good approximation given

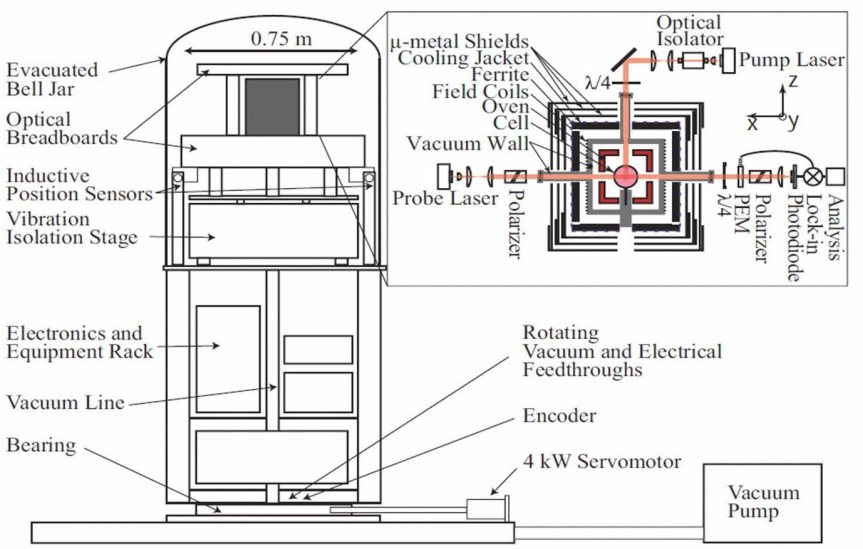

Figure 1.8: Experimental setup of the K-^{3}He comagnetometer.

by

$$P_{\mathrm{x}}^{\mathrm{e}} = \frac{\gamma_{\mathrm{e}} P_{\mathrm{z}}^{\mathrm{e}}}{R_{\mathrm{tot}}} (\beta_{\mathrm{y}}^{\mathrm{N}} - \beta_{\mathrm{y}}^{\mathrm{e}} + \frac{\Omega_{\mathrm{y}}}{\gamma_{\mathrm{N}}}) \ , \tag{1.31}$$

where $\beta_{\mathrm{y}}^{\mathrm{N}}$ and $\beta_{\mathrm{y}}^{\mathrm{e}}$ are the anomalous background fields in y-direction that couple to the ^{3}He nuclear and K electron spin, respectively, $P_{\mathrm{z}}^{\mathrm{e}}$ is the K electron spin polarization in z direction, R_{tot} the K relaxation rate, γ_{e} and γ_{N} the gyromagnetic ratios for the electrons and the ^{3}He nuclei, respectively, and Ω_{y} the rotation rate of the apparatus. The co-magnetometer also acts as a very sensitive gyroscope that sees a sinusoidal signal when the platform is rotating. To remove this and other unwanted background effects, the sidereal oscillations resulting from a 180° reversal of the apparatus are measured. The position is changed between the NS- and the EW-orientation every 22 seconds; the signal is recorded while the apparatus is stationary at each position. From 143 days of data taking the constraints on the Lorentz-violating parameters are measured to be $\tilde{b}_{\mathrm{X}}^{\mathrm{n}} = (0.1 \pm 1.6) \cdot 10^{-33}$ GeV, $\tilde{b}_{\mathrm{Y}}^{\mathrm{n}} = (2.5 \pm 1.6) \cdot 10^{-33}$ GeV and $\tilde{b}_{\mathrm{XY}}^{\mathrm{p}} < 6 \cdot 10^{-32}$ GeV, with the uncertainties being the 1σ-errors.

1.3.3 Spin polarized torsion pendulum

An experiment that searches for Lorentz violating effects in the electron sector is the one carried out by the Eöt-Wash group at the university of Washington, where a spin

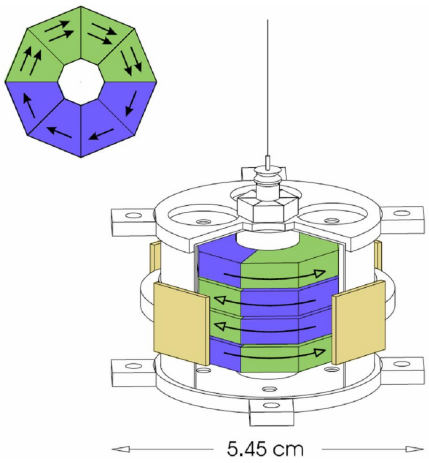

Figure 1.9: The Eöt-Wash torsion pendulum [30]: It consists of 4 octagons, each made out of 4 AlNiCo (light green) and 4 $SmCo_5$ magnets (dark blue). Upper left: top view of a single octagon; the arrows with filled heads show the relative densities and directions of the electron spins. Lower right: The pendulum is surrounded by a magnetic shield (shown cut away) that supports 4 mirror plates (light gold) that are used to monitor the twist of the pendulum. The arrows with open heads show the direction of $\vec{B}$; the outer magnetic field is negligibly small.

polarized torsion pendulum is used to search for new interactions that couple to the electronic spin [30]. The pendulum is suspended from a 75 cm long tungsten fiber inside of a vacuum vessel that sits on a turntable. Magnetic fields and gradients are reduced by a set of Helmholtz coils and 4 layers of mu-metal shielding. Torques on the pendulum are monitored by a highly sensitive optical autocollimator system. The pendulum is made out of four octagonal rings that consist of two different types of magnets ($SmCo_5$ and AlNiCo), with four $SmCo_5$ magnets on the one and four AlNiCo magnets on the other side of each ring (see Fig. 1.9). To minimize any magnetic interactions, both types of magnets were equally magnetized by sending appropriate current pulses through coils that were temporarily wound around the octagons. The magnetization was set to be in the angular direction of the octagons, such that the external magnetic field is negligibly small. In AlNiCo, as in most ferromagnetic materials, the magnetic field is almost entirely produced by the electronic spins, while in $SmCo_5$ a great part of the field comes from the orbital magnetic moment. This leads to the desired fact that one gets a substantial number of about 10^{23} polarized electrons without having an external field.

The coupling of the electronic spin σ^e to some Lorentz-violating background field $\tilde{b}^e$ is

described by the interaction potential

$$V = -\vec{\sigma}^{\mathrm{e}} \cdot \vec{\tilde{b}}^{\mathrm{e}} \ . \tag{1.32}$$

Thus, when the turntable rotates, the potential (1.32) produces a torque on the pendulum that can be detected by measuring its induced twist. This experiment constrained the Lorentz violating parameters $\tilde{b}_{\mathrm{X}}$ and $\tilde{b}_{\mathrm{Y}}$ for the electron to be less than $1.4 \cdot 10^{-31}$ GeV at the 2-σ level.

Chapter 2

Theory of spin precession

This Chapter deals with the theory that is important for this work. In Sec. 2.1 the equations describing an atom with spin in a static, external field are repeated. Afterwards, in Sec. 2.2, the optical pumping of ^{3}He and ^{129}Xe that leads to a nuclear spin polarization will be explained. Sec. 2.3 is about the Larmor precession of magnetic moments in a field, which is described by the Bloch equations. In Sec. 2.4 the equations are given for the dipolar field that is produced by spin-polarized atoms. Finally, in Sec. 2.5, the relaxation mechanisms that lead to a decay of the polarization are described.

2.1 Spins in a magnetic field

Let us consider an atom with nuclear spin $\vec{I}$, where $|\vec{I}| = \sqrt{I(I+1)}\hbar$ with the nuclear spin quantum number I that can take integral or half-integral values. The spin is associated with a (nuclear) magnetic moment given by

$$\vec{\mu} = \gamma \, \vec{I}, \tag{2.1}$$

where $\gamma = \frac{g \, \mu_\mathrm{N}}{\hbar}$ is the gyromagnetic ratio with the nuclear g-factor g, the nuclear magneton $\mu_\mathrm{N} = \frac{e\hbar}{2m_p}$ and the reduced Planck constant $\hbar = \frac{h}{2\pi}$ [57]. If the spin quantization axis is given by the z-axis, the z-component of the magnetic moment is given by

$$\mu_\mathrm{z} = \gamma \, \hbar \, m_\mathrm{I}, \tag{2.2}$$

where $m_\mathrm{I} = -I, -I+1, \cdots, I-1, I$ is the projection of the nuclear spin on the z-axis.
In a magnetic field $\vec{B} = B_0 \, \hat{e}_\mathrm{z}$ the magnetic moment interacts with the field which leads to

a splitting in the energy levels, the so-called Zeeman effect:

$$E_{\mathrm{Zeeman}} = -\mu_{\mathrm{z}}\, B_0 = -\gamma\, \hbar\, m_{\mathrm{I}} B_0. \tag{2.3}$$

In our experiment the noble gases ^{3}He and ^{129}Xe are used that both have nuclear spin $I = \frac{1}{2}$ (and electron spin $J = 0$). The projection m_I then can take the values $+\frac{1}{2}$ ("spin-up") and $-\frac{1}{2}$ ("spin-down"), i.e., the z-component of the nuclear spin is directed parallel or anti-parallel to the magnetic field. As the g-factors and therewith the gyromagnetic ratios of both ^{3}He and ^{129}Xe are negative, the state with $m_I = -\frac{1}{2}$ is energetically more favorable. The energy difference ΔE of the spin-up and spin-down state and the corresponding transition frequency, the so-called Larmor frequency ω_{L}, are given by

$$\begin{aligned} \Delta E &= \gamma\, \hbar\, B_0, \\ \omega_{\mathrm{L}} &= \gamma B_0. \end{aligned} \tag{2.4}$$

2.2 Hyperpolarization through optical pumping

In thermal equilibrium the population numbers of the Zeeman levels are distributed according to the Boltzmann statistics. This means that for a given temperature T in a magnetic field B_0, the fraction of the population numbers for a two-level system such as ^{3}He or ^{129}Xe is given by

$$\frac{N_+}{N_-} = \exp\left(-\frac{E_+ - E_-}{kT}\right) = \exp\left(-\frac{\gamma\, \hbar\, B_0}{kT}\right), \tag{2.5}$$

where $(E_+ - E_-)$ is the energy difference of Eq. 2.4, k the Boltzmann constant and $N_{+(-)}$ the population numbers of the spin-up and the spin-down state, respectively. This unequal distribution of different spin states leads us to the definition of the spin polarization of an atom with spin $F = I + J$:

$$P := \frac{1}{F}\, \frac{\sum_{\mathrm{F}} m_{\mathrm{F}} \cdot N(m_{\mathrm{F}})}{\sum_{\mathrm{F}} N(m_{\mathrm{F}})}, \tag{2.6}$$

where $N(m_{\mathrm{F}})$ is the population number of the state with the magnetic quantum number m_{F}. For ^{3}He and ^{129}Xe with $F = I = 1/2$ the (nuclear spin) polarization is equal to

$$P(I = \frac{1}{2}) = \frac{N_+ - N_-}{N_+ + N_-}\ . \tag{2.7}$$

At a field B_0 of 1 Tesla and a temperature of 300 K, the so-called thermal or Boltzmann polarization for ^{3}He or ^{129}Xe is in the order $P_{\mathrm{B}} \approx 10^{-6}$. Much higher degrees of polarization,

the so-called *hyperpolarization*, can be reached by means of optical pumping, where momentum is transferred to the atom from a resonant light source (usually a laser). In our group ^{3}He is polarized with the method of *metastability exchange optical pumping* (MEOP), where polarization degrees of up to 90% can be reached. Xenon, in contrast, can be polarized by *spin exchange optical pumping* (SEOP), where one first polarizes ^{87}Rb atoms which then transfer their momentum to the ^{129}Xe atoms via spin exchange collisions. Both methods will be explained in the next sections; detailed descriptions can be found in [84] and [3].

2.2.1 Metastability exchange optical pumping

At the Mainz polarizer, the optical pumping of ^{3}He is done at low pressures of about 1 mbar. A weak gas discharge excites the atoms from the ground state into the metastable 2^3S_1 state. From there the atoms are pumped into the $2^3P_{0,1,2}$ states. In total nine hyperfine structure lines exist between these two levels, that are named C1 to C9 in the order of increasing energies [53]. A weak homogeneous field of roughly 10 G leads to a splitting of the hyperfine levels into the Zeeman sub-levels with quantum number m_F. For the optical pumping the lines C8 and C9, that correspond to transitions from the 2^3S_1 into the 2^3P_0 state, are the preferred transitions. In the following, the pumping process on the C9-line will be explained with the help of Fig. 2.1.

Right-circularly polarized laser light (σ^+ light) with $\lambda = 1083.03$ nm excites transitions into the 2^3P_0 state with $\Delta m_\mathrm{F} = +1$. During the lifetime of this state of $\tau = 97.8$ ns [21], collisions lead to radiationless transitions into the other 2^3P levels, that are approximately equally occupied. So the following de-excitation happens almost isotropically into the Zeeman levels of the 2^3S_1 state. Repeated absorption and spontaneous re-emission then leads to a redistribution of the population numbers towards increasing m_F. This corresponds to a polarization of the electronic spin. The electronic and the nuclear spin are coupled via the hyperfine interaction in the 2^3S_1 level. The characteristic time constant of this interaction is $\tau_\mathrm{HF} = 1/A = 1/(4.493\ \mathrm{GHz}) = 2.2310^{-10}$ s [65], which is much shorter than the lifetime τ of the 2^3S_1 state (see above). At first the polarized atom is still in the metastable state, but during the long lifetime of the 2^3S_1 state the atom collides with unpolarized atoms in the ground state. Some of these collisions lead to an exchange of the excitation energy between the colliding atoms, while the nuclear spins stay unchanged. This can be expressed through the following reaction:

$$^3\mathrm{He}^*(\mathrm{A}, m_\mathrm{F}) +^3 \mathrm{He}(\mathrm{B}, m_\mathrm{I} = -1/2) \rightleftharpoons {}^3\mathrm{He}(\mathrm{A}, m_\mathrm{I} = +1/2) +^3 \mathrm{He}^*(\mathrm{B}, m_\mathrm{F} - 1)\ , \qquad (2.8)$$

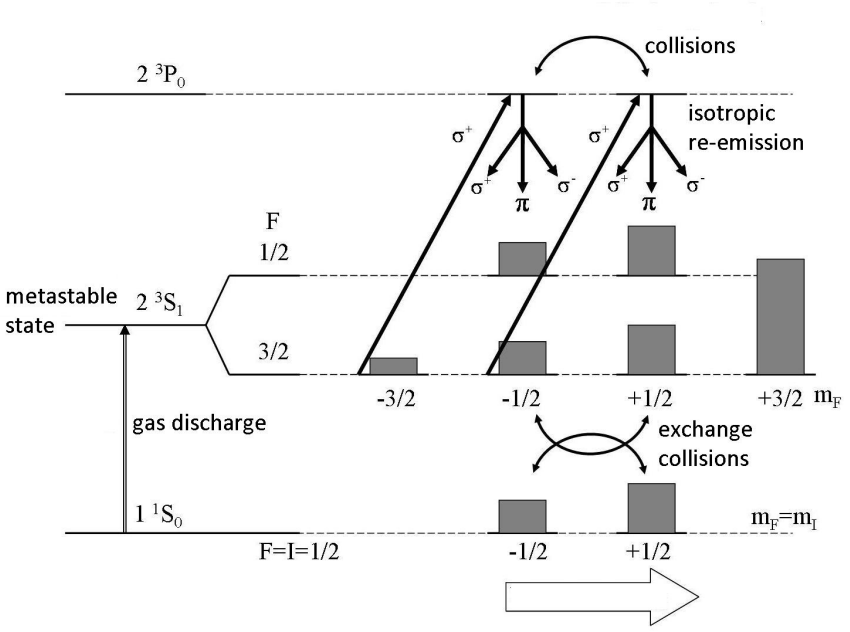

Figure 2.1: Metastability exchange optical pumping (MEOP) of ^{3}He: From the metastable 2^3S_1 state, that is excited by a gas discharge, the atoms are pumped to 2^3P_0 with the help of resonant σ^+ light. Repeated absorption and isotropic re-emission leads to a redistribution of the population numbers towards increasing m_F. Via the hyperfine interaction the electronic polarization is transferred to the nucleus. Exchange collisions between metastable and ground state atoms then lead to a nuclear spin polarization in the ground state.

where ^{3}He* is the excited atom, and (A) and (B) define the nuclei of the atoms. As there are more atoms in the states with higher m_F, i.e., $N(m_\mathrm{F}) > N(m_\mathrm{F}-1)$, the reaction preferentially happens from the left to the right side. So the ground state atoms go from $m_\mathrm{F} = -1/2$ to $m_\mathrm{F} = +1/2$, i.e., the polarization according to Eq. (2.7) is positive. At the Mainz polarizer, polarization degrees of typically 70% are reached.

2.2.2 Spin exchange optical pumping

The PTB Berlin features a polarizer for ^{129}Xe that we used for our experiments in the *Berlin magnetically shielded room* (BMSR-2). In the following the method of spin exchange optical pumping (SEOP) will be explained using the example of the PTB polarizer. A detailed description can be found in [40]. In SEOP, one firstly polarizes the electron shell of an alkali atom (here: Rubidium), and then the polarization is transfered from the atomic shell of the alkali atom to the ^{129}Xe nucleus via the spin-exchange interaction. A scheme of the PTB polarizer is shown in Fig. 2.2. It works in a continuous-flow-mode, i.e., the gases

are pumped through the system continuously, controlled by digital mass flow controllers (MFC). The gas mixture, that is cleaned from oxygen and water through filters[1], typically contains 100 mbar of isotopically enriched Xe (91.2 % ^{129}Xe), 200 mbar of N_2 and 4.7 bar of ^{4}He (the latter ones are used as buffer gases). It flows through the pumping cell, a cylindrical Duran glass cell of volume $V = 30$ cm^3, that contains a droplet of Rubidium metal. The cell is heated to about 150°C to reach a Rb vapor pressure such that the Rb can be regarded as optically thick. The gas is optically pumped by circularly polarized laser beams (about 50 W coming from one side and 70 W from the other) that excite the D_1 transition ($\lambda = 794.8$ nm) of Rubidium. The comparatively low xenon pressure is chosen because the depolarization rate for Rb-Xe collisions is quite high. To achieve a higher total pressure and therewith a pressure broadening of the Rb absorption line so that it fits better to the spectral linewidth of the laser, ^{4}He is used as buffer gas. The second buffer gas, nitrogen, serves as quenching gas to avoid radiation trapping: during collisions with the nitrogen molecules the excited alkali metal atoms can deexcite nonradiatively instead of reradiate a photon. This is desirable because the reemitted photons are unpolarized and can pump unwanted transitions and therewith lead to depolarization. Another advantage lies in the fact that the nonradiative deexcitation happens with equal probability into both ground state levels, whereas the deexcitation through photon emission prefers the unwanted branch. This advantages have to be weighted against the disadvantage of nitrogen breaking up the Rb-Xe van der Waals molecules and so slowing down the spin transfer.

When the Rubidium atom has been polarized, its electronic spin polarization can be transfered to the ^{129}Xe nucleus. This can happen either during binary collisions or during the lifetime of a van der Waals molecule. The relevant interaction is the nuclear-electron spin-exchange interaction

$$V_{\mathrm{IS}} = \alpha \vec{I} \cdot \vec{S}, \tag{2.9}$$

that couples the nuclear spin $\vec{I}$ of the xenon atom to the electron spin $\vec{S}$ of Rubidium. The coupling constant α depends on the internuclear separation R between the Rb and the Xe atom. The cross-section for the spin-exchange interaction is much higher for xenon than for helium [25]. Therefore, ^{129}Xe can be polarized much faster with SEOP than ^{3}He. This is the reason why in our group the metastable optical pumping method is used for ^{3}He.

After flowing through the pumping cell, the polarized ^{129}Xe can be separated from the buffer gases in a liquid-nitrogen Dewar: the heavier ^{129}Xe atoms are frozen out, while the other

[1] OxiSorb from the company MESSER

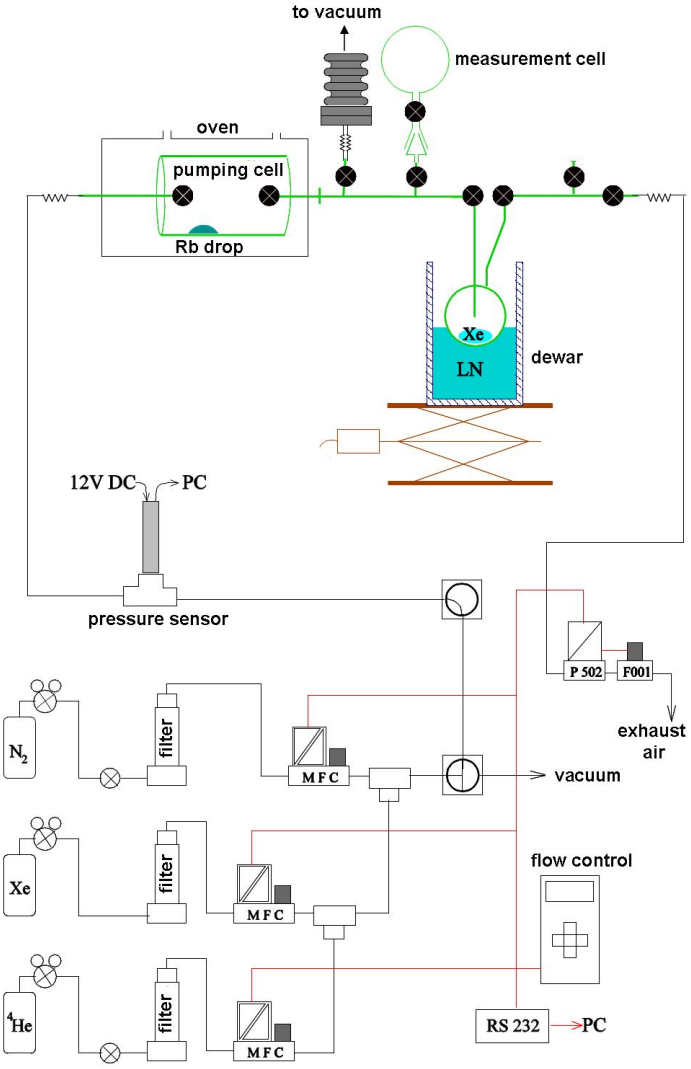

Figure 2.2: Scheme of the PTB ^{129}Xe polarizer: The gases N_2, ^{129}Xe and ^{4}He are directed through filters to mass flow controllers (MFC) that provide the desired mixing ratios. The gas mixture is flowing through the pumping cell that contains a droplet of Rb metal and is heated to about 150° C. Circularly polarized laser beams that are in resonance with the D_1 transition of Rubidium are irradiated from both sides to optically pump the Rb atoms, which then transfer the polarization to the ^{129}Xe atoms via spin exchange collisions. In a liquid-nitrogen (LN) Dewar, the polarized ^{129}Xe atoms are frozen out and thus separated from the buffer gases (N_2 and ^{4}He).

gases are released into the ambient air. Then the ^{129}Xe can be unfrozen and filled into the measurement cell. To reach a pressure of about 1 bar in the measurement cell (volume circa 100 ml), one has to freeze out for approximately one hour. The polarization after the freezing and unfreezing, where about half of the polarization is lost, amounts to $15 \pm 2\%$.

2.3 Bloch equations

The dynamics of a magnetic moment in an external magnetic field is described in detail in [70] and will be summarized here. The equations of motion for a classical magnetic moment $\vec{m}$ in a magnetic field $\vec{B}$, the Bloch equations, are given by:

$$\dot{\vec{m}}(t) = \gamma\, \vec{m}(t) \times \vec{B}(t) \ , \tag{2.10}$$

where γ is the gyromagnetic ratio. In [70] it is shown that a quantum mechanical treatment of an atomic magnetic moment $\hat{\vec{\mu}} = \gamma\hbar\hat{\vec{I}}$, i.e., solving the Schroedinger equation for the Hamiltonian $\hat{H} = -\hat{\vec{\mu}} \cdot \hat{\vec{B}}$, leads to the same result as the classical equation (2.10). The classical magnetic moment vector $\vec{m}$ then just has to be replaced by the expectation value $\langle\hat{\vec{\mu}}\rangle$. Eq. (2.10) not only holds true for the expectation value of the magnetic moment of a single spin, but even for the expectation value of the total magnetic moment,

$$\langle\hat{\vec{m}}\rangle = \sum \langle\hat{\vec{\mu}}\rangle \ , \tag{2.11}$$

if we assume that the single spins do not interact with each other. To simplify matters, the classical notation will be used in the following.

For a spin-polarized gas, the magnitude of the magnetic moment is proportional to the polarization P and the number of gas atoms, $N = \frac{pV}{kT}$ (with pressure p, volume V, temperature T and Boltzmann constant k):

$$m = \ N\, P\, \mu = N\, P\, \gamma\, I\, \hbar \ . \tag{2.12}$$

Another quantity often used is the magnetization $\vec{M}$, that is defined as the quantity of magnetic moment per unit volume V:

$$\vec{M} = \frac{1}{V}\vec{m} = \frac{1}{V}\sum \vec{\mu} \ . \tag{2.13}$$

If the (static) magnetic field is pointing to the z-direction, $\vec{B} = B_0\, \hat{\mathrm{e}}_z$, and the magnetic

moment is tilted by an angle α relative to the magnetic field axis, i.e.,

$$\vec{m} = \begin{pmatrix} m \sin\alpha \cos\varphi \\ m \sin\alpha \sin\varphi \\ m \cos\alpha \end{pmatrix} \tag{2.14}$$

with an arbitrary azimuth angle φ, it follows from Eq. 2.10 that

$$\dot{\vec{m}} = -\gamma B_0 \, m \, \sin\alpha \, \hat{\mathrm{e}}_\varphi \ , \tag{2.15}$$

where $\hat{\mathrm{e}}_\varphi$ is the normal vector in azimuthal direction. Eq. 2.15 means that the magnetic moment $\vec{m}$ is rotating clockwise, i.e., with a negative sense of rotation, around the magnetic field axis (z-axis) with the angular frequency $\omega_\mathrm{L} = |\gamma B_0|$. This rotation is called *Larmor precession* and the corresponding frequency the *Larmor frequency*. The energy $\Delta E = \hbar\,\omega_\mathrm{L}$ corresponds to the energy difference between the two Zeeman levels according to Eq. 2.4.

An easy way to tilt the magnetic moment vector away from the axis of the guiding field $\vec{B}_0$ is to switch on an additional, constant field $\vec{B}_1$ perpendicular to $\vec{B}_0$. If the switching operation of the $\vec{B}_1$ field happens sufficiently fast (non-adiabatic field change), i.e.,

$$t_\mathrm{switch} \ \ll \ \frac{2\pi}{\omega_\mathrm{L}}, \tag{2.16}$$

the magnetic moment cannot follow the magnetic field vector and then starts to precess around the new field axis, $\vec{B}_0 + \vec{B}_1$, under the angle $\alpha = \arctan\frac{B_1}{B_0}$. If, by contrast, the magnetic field changes slowly (adiabatic field change), i.e.,

$$t_\mathrm{switch} \ \gg \ \frac{2\pi}{\omega_\mathrm{L}}, \tag{2.17}$$

the magnetic moment vector follows the field and is then aligned along the new field axis, $\vec{B}_0 + \vec{B}_1$, without precessing. For our experiments at PTB Berlin we used this method of switching on an additional field to generate spin precession (see Chap. 3.2 and 4.1.4).

Another way to reach a tilting of the magnetic moment, that is used for example in magnetic resonance imaging, is by irradiating an additional magnetic field $\vec{B}_1(t)$ that is rotating[2] in

[2] In practice one usually does not use a rotating but an alternating field $B_\mathrm{x}(t) = B_\mathrm{x0} \cos\omega_\mathrm{r} t$. This can be broken down into two rotating components, one rotating clockwise and the other counterclockwise. One can show that the component rotating in the opposite sense as the precessing magnetic moment can be neglected.

the plane perpendicular to the static field (here the x-y-plane) with angular frequency ω_r,

$$\vec{B}_1(t) = B_1(\hat{e}_\mathrm{x}\cos\omega_\mathrm{r}t + \hat{e}_\mathrm{y}\sin\omega_\mathrm{r}t) \ . \tag{2.18}$$

The Bloch equations (2.10) with $\vec{B}(t) = \vec{B}_0 + \vec{B}_1(t)$ then can be solved using a coordinate system rotating around the z-axis at frequency ω_r (see [70]). For the simplest case that the $\vec{B}_1$ field rotates in resonance with the Larmor frequency, $\omega_\mathrm{r} = \gamma B_0$, the tilting angle is given by

$$\alpha = \gamma\, B_1\, t_\mathrm{irr} \ , \tag{2.19}$$

where t_irr is the duration of irradiation of the $\vec{B}_1$ field. After the magnetic moment has been tilted (either by a fast field switch or by irradiating a rotating field), it precesses freely around the axis of the $\vec{B}_0$ field. Due to different relaxation processes that are described in Sec. 2.5, the longitudinal component of the magnetic moment tends to reach its equilibrium value m_0, while its transverse components tend to vanish (the magnetic moment will wish to be parallel to the static $\vec{B}_0$ field). Therefore, we have to extend Eq. (2.10) by the following relaxation terms:

$$\dot{m}_\mathrm{x} = \gamma\,(\vec{m}\times\vec{B})_\mathrm{x} - \frac{m_\mathrm{x}}{T_2} \ , \tag{2.20}$$

$$\dot{m}_\mathrm{y} = \gamma\,(\vec{m}\times\vec{B})_\mathrm{y} - \frac{m_\mathrm{y}}{T_2} \ , \tag{2.21}$$

$$\dot{m}_\mathrm{z} = \gamma\,(\vec{m}\times\vec{B})_\mathrm{z} + \frac{m_0 - m_\mathrm{z}}{T_1} \ . \tag{2.22}$$

The precession signal can be detected with a so-called pickup coil pair, whose axis is oriented perpendicular to the $\vec{B}_0$ axis (in our experiment SQUID detectors are used, see Sec. 3.2). The magnetic moment induces a periodically variating current in the pickup coils. The detected signal is referred to as the FID (Free-Induction-Decay) signal.

Ramsey-Bloch-Siegert shift

Such fields as in Eq. (2.18) that rotate in the plane perpendicular to the static B_0-field have an influence on the Larmor precession frequency as can be deduced from the results of Ramsey [64] who generalized the results of Bloch and Siegert [11]. If the rotation frequency, ω_r, is not exactly equal to the Larmor frequency ω_L of the atoms, the precession frequency is shifted according to

$$\Delta\omega_\mathrm{RBS} = \begin{cases} +\sqrt{(\omega_\mathrm{L}-\omega_\mathrm{r})^2+\omega_1^2} - (\omega_\mathrm{L}-\omega_\mathrm{r}) & \text{for } \omega_\mathrm{L} < \omega_\mathrm{r} \ , \\ -\sqrt{(\omega_\mathrm{L}-\omega_\mathrm{r})^2+\omega_1^2} - (\omega_\mathrm{L}-\omega_\mathrm{r}) & \text{for } \omega_\mathrm{L} > \omega_\mathrm{r} \ , \end{cases} \tag{2.23}$$

where ω_1 is related to the magnitude of the B_1-field as $\omega_1 = \gamma\ B_1$.

2.4 Magnetic field produced by spin-polarized atoms

A homogeneous distribution of magnetic moments in a spherical cell produces a magnetic dipole field *outside* the cell [37], that is described by the formula

$$\vec{B}(\vec{r}) = \frac{\mu_0}{4\pi}\ \frac{3\hat{r}(\hat{r}\cdot\vec{m}) - \vec{m}}{r^3} \quad . \tag{2.24}$$

If the magnetic moments are oriented along the z-axis, i.e., the dipole axis is equal to the z-axis, the z-component of the magnetic field outside the cell at the distance r from the center of the cell is given by

$$B_z(r) = \frac{\mu_0}{4\pi}\frac{m\left(3cos^2\Theta - 1\right)}{r^3} \quad \text{for } r > R_\mathrm{Z}\ , \tag{2.25}$$

with R_Z being the cell radius, μ_0 the vacuum permeability, $m = NP\gamma I\hbar$ the magnitude of the magnetic moment of the ^{3}He or ^{129}Xe atoms (see Eq. (2.12)) and Θ the angle between the z-axis and the line that connects the cell center and the point of measurement. For $\Theta = 0$, i.e., for a point on the z-axis, and by using Eq. (2.12) and the ideal gas law, one can write the above equation as

$$B_z(r) = \frac{pV}{kT}\frac{2\mu_0 P\gamma I\hbar}{4\pi r^3}\ , \tag{2.26}$$

where p is the pressure in the cell, V the volume of the cell, k the Boltzmann constant, T the temperature, P the degree of polarization, γ the gyromagnetic ratio and $I = \frac{1}{2}$ the nuclear spin of the gas atoms. So the magnetic field produced by a spin-polarized gas is proportional to the γ-ratio of the species, the polarization P, and the number of gas atoms N, and it decreases with the distance r according to $\frac{1}{r^3}$.

Demagnetization field

For an ideally spherical cell the average magnetic field produced by the polarized spins *inside* the cell is zero, because the fields of the single magnetic moments cancel each other [81]. This has also been verified in a calculation with "Mathematica". Due to the fact that in reality the measurement cell is not an ideal sphere but has an appendix, for example, the spins of each species (^{3}He or ^{129}Xe) in the appendix produce a so-called demagnetization field, $\vec{B}_\mathrm{demag}$. So the field inside a non-spherical cell can not be regarded as zero anymore. In a simple model one can view the main part of the cell as an ideal sphere A, and the appendix as a second small sphere B (see Fig. 2.3). The magnetic moment of the polarized

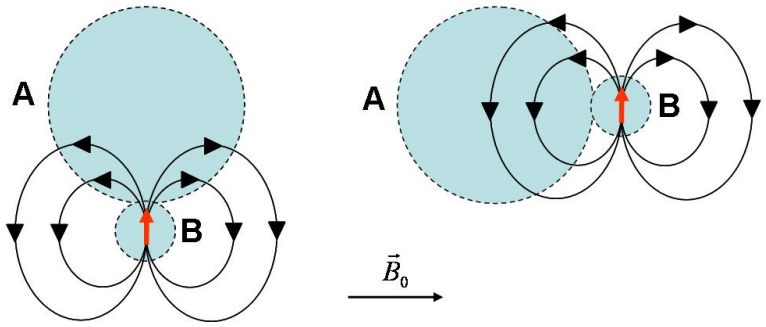

Figure 2.3: Demagnetization field produced by the magnetic moment in the cell's appendix, approximated as a second small sphere B. It can be seen that the field in the spherical part of the cell depends on if the cell's appendix is aligned parallel or perpendicular to the magnetic field.

gas in volume B now produces a magnetic dipole field in volume A, and, the other way around, the gas in volume A produces a field in volume B. Looking at the magnetic field lines in Fig. 2.3, one can see that the size and the orientation of the demagnetization field depends on the orientation of the appendix relative to the magnetic holding field $\vec{B}_0$. When the magnetic moment of ^{3}He (^{129}Xe) in volume A is precessing around the main field B_0, also the moment in volume B is precessing around B_0. Because of field inhomogeneities, the precession frequency in volume A differs slightly from the precession frequency in volume B. This leads to unwanted effects in the weighted frequency (or phase) difference which is considered in our experiment (see Chap. 4.3.3).

2.5 Relaxation

Due to different mechanisms that will be explained in the following sections, the polarization P and with it the magnetic moment is not stable in time, but it decreases exponentially until it reaches the equilibrium (Boltzmann) polarization P_B,

$$P(t) = (P(t_0) - P_\mathrm{B}) \exp(-t/T_1) + P_\mathrm{B} \ . \tag{2.27}$$

This process is called relaxation, and the corresponding decay time is the so-called *longitudinal relaxation time* T_1 that will be discussed in the following section. In Sec. 2.5.2 I will deal with the *transverse relaxation time* T_2^* which is the decay time of the transverse polarization, i.e., the part of the magnetic moment that is precessing around an external magnetic field.

2.5.1 Longitudinal Relaxation

The relaxation mechanisms that are relevant for this work are the gradient relaxation ($T_{1,\mathrm{grad}}$), as well as the relaxation due to collisions of the noble gas atoms with the wall ($T_{1,\mathrm{wall}}$) and with each other due to binary or van der Waals collisions ($T_{1,\mathrm{bin}}$ and $T_{1,\mathrm{vdW}}$). So the total longitudinal relaxation time T_1 is given by:

$$\frac{1}{T_1} = \frac{1}{T_{1,\mathrm{grad}}} + \frac{1}{T_{1,\mathrm{wall}}} + \frac{1}{T_{1,\mathrm{bin}}} + \frac{1}{T_{1,\mathrm{vdW}}} \ . \tag{2.28}$$

The single terms will be explained in the following.

Wall relaxation

During collisions of the polarized noble gas atoms with the walls of the glass cell, the dipolar coupling as well as the Fermi-contact interaction with small para- or ferromagnetic impurities in the glass matrix can lead to spin relaxation. This can happen either during the adsorption of the atoms at the glass wall, or during the diffusion into the glass matrix. The latter process can be deeply suppressed by using quasi impermeable aluminosilicate glass, as the GE-180 glass[3] that was used for our cells. The wall relaxation rate $1/T_{1,\mathrm{wall}}$ is pressure independent and proportional to the surface-to-volume ratio of the cell:

$$\frac{1}{T_{1,\mathrm{wall}}} \propto \frac{S}{V} \ . \tag{2.29}$$

A detailed description of the longitudinal relaxation of hyperpolarized ^{3}He in glass cells can be found in [66], [67] and [23].

Gradient relaxation

If a polarized noble gas atom moves through an inhomogeneous magnetic field, transverse gradients generate a temporally fluctuating magnetic field in the rest frame of the atom. This field can cause spin flips if its Fourier spectrum contains components near the Larmor frequency $\omega_L = \gamma \cdot B$. Let the magnetic holding field $\vec{B}$ be oriented in x-direction (to be consistent with the coordinate system of the shielded room as shown in Fig. 3.6). Then according to [16] the longitudinal relaxation rate in a spherical volume due to the transverse

[3] GE-180 is produced by "General Electric" and mainly consists of SiO_2 (60%), BaO (18%), Al_2O_3 (14%) and CaO (7%).

field gradients $\vec{\nabla}B_{1,\mathrm{y}} = (\frac{\partial B_{1,\mathrm{y}}}{\partial x}, \frac{\partial B_{1,\mathrm{y}}}{\partial y}, \frac{\partial B_{1,\mathrm{y}}}{\partial z})$ and $\vec{\nabla}B_{1,\mathrm{z}} = (\frac{\partial B_{1,\mathrm{z}}}{\partial x}, \frac{\partial B_{1,\mathrm{z}}}{\partial y}, \frac{\partial B_{1,\mathrm{z}}}{\partial z})$ is given by

$$\begin{aligned} \frac{1}{T_{1,\mathrm{grad}}} &= 2D\frac{|\vec{\nabla}B_{1,\mathrm{y}}|^2 + |\vec{\nabla}B_{1,\mathrm{z}}|^2}{B_0^2} \\ &\quad \times \sum_n \frac{1}{(x_{1n}^2 - 2)(1 + D^2 x_{1n}^4 (\gamma B_0)^{-2} R^{-4})} \ . \end{aligned} \tag{2.30}$$

Here D is the diffusion coefficient, $\vec{B}_0 = B_0 \cdot \hat{e}_{\mathrm{x}}$ the average homogeneous field in x-direction, γ the gyromagnetic ratio, R the cell radius and x_{1n} (n = 1, 2, 3, ...) are the zeros of the derivative of the spherical Bessel function ($\frac{d}{dx} j_1(x_{1n}) = 0$). $\vec{B}_1(\vec{r})$ is the deviation of the local field from the average homogeneous field $\vec{B}_0$, and its mean value is assumed to be zero. The diffusion coefficient for ^{3}He and ^{129}Xe in a gas mixture (GM) with helium, xenon and nitrogen, which in our experiment is used as buffer gas to suppress the van der Waals relaxation (see below), is given by [52]:

$$\begin{aligned} \frac{1}{D_{\mathrm{He}}^{GM}} &= \left(\frac{p_{\mathrm{He}}}{D_{\mathrm{He}}} + \frac{p_{\mathrm{Xe}}}{D_{\mathrm{He\ in\ Xe}}} + \frac{p_{N_2}}{D_{\mathrm{He\ in\ N_2}}} \right) \frac{1}{p_0} \frac{T_0^{3/2}}{T^{3/2}}, \\ \frac{1}{D_{\mathrm{Xe}}^{GM}} &= \left(\frac{p_{\mathrm{Xe}}}{D_{\mathrm{Xe}}} + \frac{p_{\mathrm{He}}}{D_{\mathrm{Xe\ in\ He}}} + \frac{p_{N_2}}{D_{\mathrm{Xe\ in\ N_2}}} \right) \frac{1}{p_0} \frac{T_0^{3/2}}{T^{3/2}} \ , \end{aligned} \tag{2.31}$$

where p_{He}, p_{Xe} and p_{N_2} are the ^{3}He, ^{129}Xe and nitrogen partial pressures, $D_{\mathrm{He/Xe}}$ is the diffusion coefficient of pure ^{3}He or ^{129}Xe gas at standard conditions[4] (p_0 = 1013.25 mbar, T_0 = 273.15 K), and $D_{\mathrm{X\,in\,Y}}$ the diffusion coefficient of species X in species Y for $p_{\mathrm{X}} \to 0$. The different coefficients for a pressure of 1 mbar are listed in Tab. 2.5.1.
If one considers, according to [16], the characteristic diffusion time $\tau_{\mathrm{d}} = R^2/D$ and the characteristic precession time $\tau_{\mathrm{p}} = 1/\omega_{\mathrm{L}}$, Eq. (2.30) can be approximated by simpler expressions, depending on the size of the ratio

$$\frac{\tau_{\mathrm{d}}}{\tau_{\mathrm{p}}} = \frac{R^2 \omega_{\mathrm{L}}}{D} \propto pB_0 \ . \tag{2.32}$$

For $\tau_{\mathrm{d}}/\tau_{\mathrm{p}} \ll 1$, i.e., when the precession time is long compared to the diffusion time, which is the case for low pressures and low magnetic fields (the regime of motional narrowing), we

[4]There exist different conventions about the standard conditions. In the context of spin relaxation and chemical shifts the unit *amagat (amg)* is often used, which is a unit of number density that is defined as the number of ideal gas molecules per unit volume at 1 atm (= 101.325 kPa) and 0°C (= 273.15 K). In this work these values are taken as standard pressure and temperature.

get

$$\frac{1}{T_{1,\mathrm{grad}}} \approx \frac{8\,R^4}{175D}\,\gamma^2\,(|\vec{\nabla}B_{1,\mathrm{y}}|^2 + |\vec{\nabla}B_{1,\mathrm{z}}|^2)\ . \tag{2.33}$$

On the other hand, at high fields and high pressures, when the precession time is short compared to the diffusion time, i.e., $\tau_\mathrm{d}/\tau_\mathrm{p} \gg 1$, the following approximation can be used:

$$\frac{1}{T_{1,\mathrm{grad}}} = D\frac{|\vec{\nabla}B_{1,\mathrm{y}}|^2 + |\vec{\nabla}B_{1,\mathrm{z}}|^2}{B_0^2}\ . \tag{2.34}$$

So one can see that in the upper case, the longitudinal relaxation rate is proportional to $\frac{1}{D}$ and hence proportional to the pressure, while in the lower case $\frac{1}{T_{1,\mathrm{grad}}}$ is inversely proportional to the pressure. Furthermore, in the motional narrowing regime, the T_1 relaxation depends on the absolute field gradients, while in the other case it depends on the relative gradients.

Binary and van der Waals relaxation

Another relaxation mechanism arises during collisions between the ^{3}He or ^{129}Xe atoms, when the magnetic dipole-dipole interaction couples the nuclear spins to the relative angular momentum of the noble gas atoms. As a result, nuclear spin polarization is lost to orbital angular momentum. This can happen either during binary collisions or during the lifetime of weakly bound van-der-Waals molecules. The latter are dominating for the heavier, polar ^{129}Xe atoms, while for the lighter ^{3}He atoms only the binary collisions play a role. According to [56] the binary relaxation rate for ^{3}He at pressure p and temperature T is given by

$$\frac{1}{T_{1,\mathrm{bin}}^{\mathrm{He}}} \approx \frac{1}{754\ \mathrm{h}}\ \frac{p}{p_0}\frac{T_0}{T}\ . \tag{2.35}$$

where p_0 and T_0 are the standard pressure and temperature. For ^{129}Xe the binary relaxation can be found in [36]:

$$\frac{1}{T_{1,\mathrm{bin}}^{\mathrm{Xe}}} \approx \frac{1}{56\ \mathrm{h}}\ \frac{p}{p_0}\frac{T_0}{T}\ . \tag{2.36}$$

In [18] the pressure-independent van der Waals relaxation rate for ^{129}Xe is deduced. In the case of pure ^{129}Xe the maximum relaxation time is

$$T_{1,\mathrm{vdW}}^{\mathrm{Xe}} = 4.1\ \mathrm{h}\ . \tag{2.37}$$

Anyhow, by adding buffer gases such as helium or nitrogen, one can suppress the van der Waals relaxation, because the buffer gas molecules can break up the Xe-Xe van der Waals

Diff. coeff.	Value ($\frac{\mathrm{cm}^2}{\mathrm{s}}$)	Ref.	Temperature (K)
D_{He}	≈ 1880	[52]	293
$D_{\mathrm{He\ in\ Xe}}$	≈ 600	[59]	300
$D_{\mathrm{He\ in\ N_2}}$	≈ 770	[59]	300
D_{Xe}	≈ 58	[28]	300
$D_{\mathrm{Xe\ in\ He}}$	≈ 790	[28]	300
$D_{\mathrm{Xe\ in\ N_2}}$	≈ 210	[28]	353

Table 2.1: Diffusion coefficients for ^{3}He and ^{129}Xe at a pressure of 1 mbar

molecules. Then we get [18]:

$$\frac{1}{T_{1,\mathrm{vdW}}^{\mathrm{Xe\ in\ B}}} = \frac{1/T_{1,\mathrm{vdW}}^{\mathrm{Xe}}}{1 + r[B]/[Xe]} \ , \tag{2.38}$$

where $[B]/[Xe]$ is the ratio of the partial pressures of the buffer gas and ^{129}Xe, and r the breakup rate coefficient relative to the breakup rate for ^{129}Xe molecules. For ^{129}Xe it is $r = 1$ per definition, while for N_2 it was measured to be $r = 1.05(8)$ [18].

2.5.2 Transverse Relaxation

If the transverse magnetic moment is precessing around an external field as described in Sec. 2.3, the amplitude of the precession signal decreases exponentially with the characteristic time constant T_2^*, the (effective) transverse relaxation time. The reason for this relaxation is the loss of phase coherence of the single magnetic moments due to collisions of the atoms with the walls and with each other, and due to magnetic field gradients. The T_2^* relaxation rate depends on the longitudinal relaxation times $T_{1,\mathrm{wall}}$, $T_{1,\mathrm{bin}}$ and $T_{1,\mathrm{vdW}}$ discussed in the previous section, and on a gradient term $1/T_{2,\mathrm{grad}}$:

$$\frac{1}{T_2^*} = \frac{1}{T_{1,\mathrm{wall}}} + \frac{1}{T_{1,\mathrm{bin}}} + \frac{1}{T_{1,\mathrm{vdW}}} + \frac{1}{T_{2,\mathrm{grad}}} \ . \tag{2.39}$$

Analytical expressions for the gradient relaxation rate $1/T_{2,\mathrm{grad}}$ for spherical sample cells in a field $\vec{B}$ that is oriented in x-direction are derived in [16]:

$$\begin{aligned} \frac{1}{T_{2,\mathrm{grad}}} = {} & \frac{8R^4\gamma^2|\vec{\nabla}B_{1,\mathrm{x}}|^2}{175D} + D\frac{|\vec{\nabla}B_{1,\mathrm{y}}|^2 + |\vec{\nabla}B_{1,\mathrm{z}}|^2}{B_0^2} \\ & \times \sum_{\mathrm{n}} \frac{1}{(x_{1\mathrm{n}}^2 - 2)(1 + D^2 x_{1\mathrm{n}}^4 (\gamma B_0)^{-2} R^{-4})} \ . \end{aligned} \tag{2.40}$$

Here D is again the diffusion coefficient according to (2.31), $\vec{B}_0 = B_0 \cdot \hat{e}_\mathrm{x}$ the average homogeneous field in x-direction, $\vec{B}_1(\vec{r})$ the deviation of the local field from $\vec{B}_0$, γ the gyromagnetic ratio, R the cell radius and x_{1n} (n = 1, 2, 3, ...) are the zeros of the derivative of the spherical Bessel function ($\frac{d}{dx} j_1(x_{1n}) = 0$).

Now one can introduce approximations to Eq. (2.40) as was done in Sec. 2.5.1. For the case of motional narrowing, where $\tau_\mathrm{d}/\tau_\mathrm{p} \ll 1$ is valid, i.e., at low pressures and low magnetic field, we get

$$\frac{1}{T_{2,\mathrm{grad}}} = \frac{4R^4\gamma^2}{175D} \cdot \left(|\vec{\nabla} B_{1,\mathrm{y}}|^2 + |\vec{\nabla} B_{1,\mathrm{z}}|^2 + 2|\vec{\nabla} B_{1,\mathrm{x}}|^2 \right) , \tag{2.41}$$

whereas for $\tau_\mathrm{d}/\tau_\mathrm{p} \gg 1$, i.e., at high pressures and high magnetic field, the following equation is valid:

$$\frac{1}{T_{2,\mathrm{grad}}} = \frac{8R^4\gamma^2 |\vec{\nabla} B_{1,\mathrm{x}}|^2}{175D} . \tag{2.42}$$

In both cases the transverse relaxation rate is inversely proportional to D and hence proportional to the pressure, and it depends on the absolute field gradients. For high pressures and high magnetic field, only the longitudinal gradient components $\vec{\nabla} B_{1,\mathrm{x}} = (\frac{\partial B_{1,\mathrm{x}}}{\partial x}, \frac{\partial B_{1,\mathrm{x}}}{\partial y}, \frac{\partial B_{1,\mathrm{x}}}{\partial z})$ play a role.

Chapter 3

Spin precession of ^{3}He: Experiment and results

In preparation of the ^{3}He/ ^{129}Xe clock-comparison experiments that will be dealt with in Chap. 4, in December 2006 the spin precession of ^{3}He alone was measured. ^{3}He can be used as a highly sensitive magnetometer by measuring precisely its spin precession frequency, which is proportional to the external magnetic field (see Eq. (2.4)). The sensitive detection and control of magnetic fields is of great importance both in the applied sector (e.g. geomagnetic [22] or biomagnetic measurements [9]) and in fundamental physics. An example for an application of the ^{3}He magnetometer in fundamental research is the measurement of the Electric Dipole Moment of the neutron (nEDM), which is a highly sensitive probe for CP-violation [1]. In the "n2EDM" research project at the Paul Scherrer Institut (PSI) in Villigen/CH the magnetometry with ^{3}He is an important component. As the experimental limit of the neutron EDM is pushed lower, fluctuations of the magnetic field in the spectrometer region become a principal source of error. Therefore, it is of great importance to measure the magnetic field in this region with high sensitivity. Ref. [27] presents the proposed layout of the neutron EDM spectrometer, as well as test measurements with a prototype of a flat ^{3}He magnetometer vessel.

The idea for a magnetometer based on the detection of spin precession of gaseous, nuclear spin-polarized ^{3}He arises from Cohen-Tannoudji et al. [19], who in 1969 used a ^{87}Rb-magnetometer to detect the magnetic field produced by precessing ^{3}He spins. The setup of his experiment is shown in Fig. 3.1: Two spherical cells of 6 cm diameter, one filled with ^{87}Rb and the other with ^{3}He at a pressure of 4 mbar, are optically pumped by resonant, circularly polarized light (B_1 for ^{87}Rb and B_2 for ^{3}He). They are situated in a magnetic

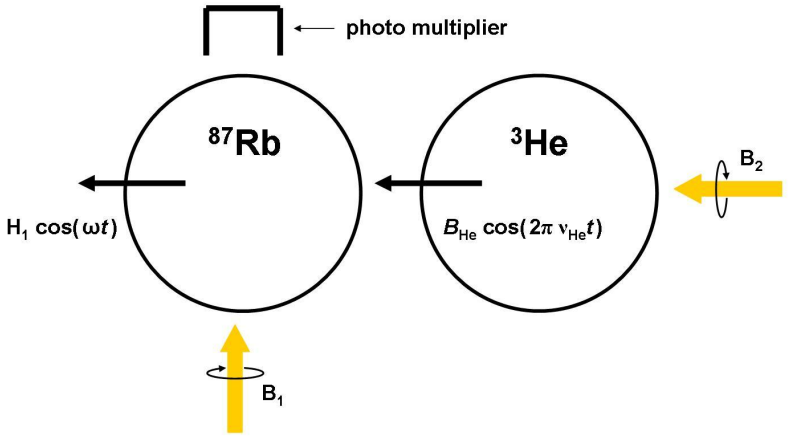

Figure 3.1: Setup of the Cohen-Tannoudji experiment: The ^{87}Rb and ^{3}He atoms are optically pumped by resonant, circularly polarized light (B_1 for ^{87}Rb and B_2 for ^{3}He). The Rb magnetometer detects the alternating dipole field $B_{\mathrm{He}}\cos(2\pi\nu_{\mathrm{He}}t)$ produced by the freely precessing ^{3}He atoms.

shielding that reduces the external magnetic noise by a factor 10^5. Additional compensation coils lead to a low residual field with a field homogeneity such that the relaxation time is no longer limited by field gradients. When the maximum polarization of ^{3}He of about 5% is reached, an additional field $\vec{h}$ of 2 μG perpendicular to the ^{3}He pumping direction is switched on. The nuclear spins now start to precess around $\vec{h}$ at a Larmor frequency ν_{He} of about 6 mHz and thereby produce an alternating dipole field $B_{\mathrm{He}}\cos(2\pi\nu_{\mathrm{He}}t)$ that is seen by the Rb atoms. To measure the spin precession the transmitted light of B_1 is detected by a photomultiplier. The alternating field induces spin flips in the Rubidium that change its absorption behavior. By irradiating an alternating magnetic field $H_1\cos(\omega t)$, with the frequency ω being near the Larmor frequency of the Rubidium atoms, one reaches a resonant behavior that increases the sensitivity. Fig. 3.2 shows the recorded precession signal over a period of 11 hours. In his experiment Cohen-Tannoudji already reached a sensitivity of about 100 $\mathrm{fT}/\sqrt{\mathrm{Hz}}$ and a transverse nuclear relaxation time T_2^* of 140 min.

Our ^{3}He magnetometer works according to the same principle, but instead of the Rb-magnetometer SQUIDs are used as magnetic field detectors (see Sec. 3.2). The ^{3}He atoms are optically pumped using the MEOP method described in Sec. 2.2.1. With signal-to-noise ratios of more than 4000 and a measured transverse spin relaxation time T_2^* of up to 60 hours (see Sec. 3.3), it is possible to apply the ^{3}He magnetometer for long-term measurements with ultra-high sensitivity (see Sec. 3.4).

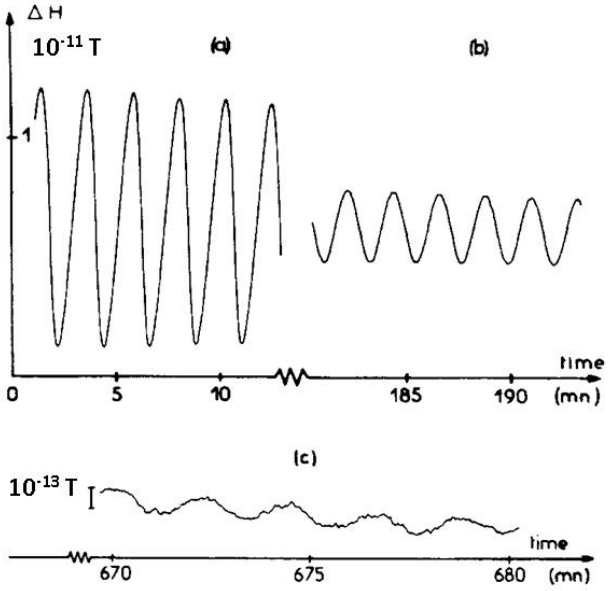

Figure 3.2: Spin precession of ^{3}He observed by Cohen-Tannoudji in 1969.

3.1 Preparation of the measurement cells

In order to reach long T_1 and therewith long T_2^* relaxation times, one has to put some effort in the preparation of the measurement cells. For our magnetometer cells we used GE180 glass that in previous experiments pointed out to have good relaxation properties [66, 67, 23]. The cells are spherical and have a diameter of 6 cm (see Fig. 3.3).
To get rid of ferromagnetic contaminations, the cells were cleaned with a 2 percent solution of Mucasol, a cleaning agent of the company Merz that contains surfactants and phosphates[1]. Afterwards the cells were baked-out at 450° C at a vacuum pumping station until the vacuum reached less then 10^{-7} mbar. The cleaning is not only important to reach good relaxation properties, but also to get a high efficiency during the optical pumping process. If there are too many foreign atoms like nitrogen or oxygen in the cell, they can reduce the density of the metastable atoms via so called *quench collisions*, which leads to a reduced polarization [84].

After the cleaning process the cells were demagnetized. Therefore, they were put into a

[1]The cells used for the clock-comparison measurements were additionally treated with so-called "Piranha solution" consisting of a mixture of concentrated sulfuric acid and hydrogen peroxide at the mixing ratio 7:3 [13].

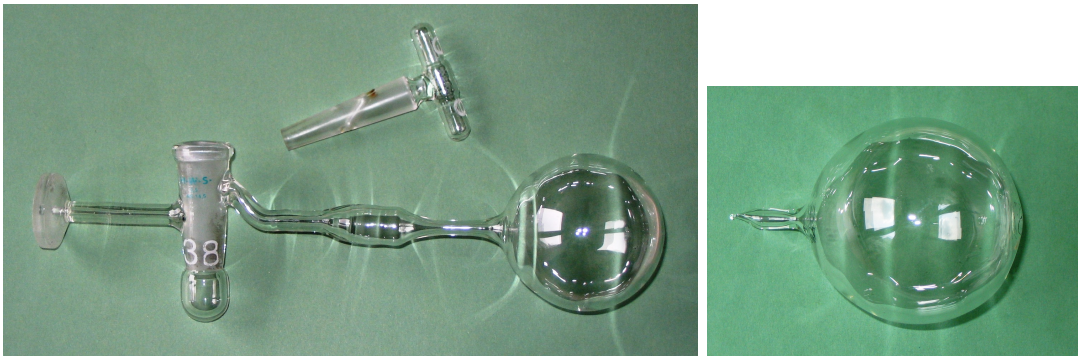

Figure 3.3: Magnetometer cell out of GE 180 glass with appendix and stopcock (*left*) and filled with ^{3}He after the sealing (*right*)

strong magnetic field of about 700 G that is reduced periodically to zero, whereas the envelope of the field decreases linearly. This procedure reduces the magnetization of small ferromagnetic particles (e.g. magnetite particles of μm sizes) in the glass [34].

The measurement of the T_1 times of the cells was done with two different methods. Firstly the cells were filled with 1 bar of polarized ^{3}He, and T_1 was measured in a nuclear magnetic resonance (NMR) setup: The atoms were kept in a holding field of about 8 G, and every 15 minutes the spins were flipped by a small angle ($\alpha < 3°$), and the FID signal was recorded. The amplitude, which is proportional to the polarization, was determined via a Fast Fourier Transformation. An exponential fit to the amplitude-time data (with one data point every 15 minutes) then gave the T_1 time. The measurement typically took several days, depending on T_1. If the measured relaxation times were too low, the cells were baked-out and demagnetized once more, which sometimes led to a significant improvement of T_1. In total 8 cells were measured, which had T_1 times between 34 and 53 hours.

In this first T_1 measurement the cells were measured with appendix and stopcock and at high pressures. For the magnetometer measurements it is better to work at low pressures in the regime of motional narrowing (see Chap. 2.5.2). Furthermore, the stopcock could be a handicap, because impurities could enter into the cell. For this reason we used sealed cells that are closed to the outside. The sealing was done by strongly heating the appendix at the point of its smallest diameter, so that the glass narrows down under the increased air pressure. Such a sealed cell is shown on the right side of Fig. 3.3. When the first T_1 measurement led to sufficient results, the cells were evacuated again and then filled with ^{3}He at pressures between 1 and 4.5 mbar. This is the pressure regime where reasonable

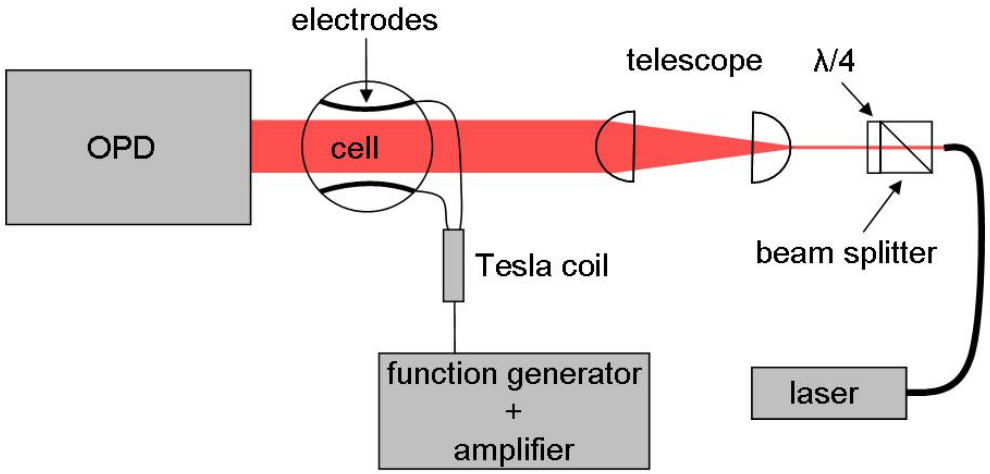

Figure 3.4: Setup for the T_1 measurements of the magnetometer cells.

polarization degrees can be reached using metastability exchange optical pumping.

The second T_1 measurement of the sealed cells at low gas pressures was done as follows (see Fig. 3.4): In a homogeneous magnetic field of about 10 Gauss the ^{3}He atoms were optically pumped with circularly polarized laser light ($\lambda = 1083$ nm). To ignite the gas discharge that excites the atoms to the metastable state, two ring-shaped copper electrodes were fixed at the cell. They were part of a resonance circuit with a function generator, an amplifier and a Tesla coil. The polarization was measured with a so called *optical polarization detection* (OPD) that analyzes the circular polarization of the 668 nm fluorescence line of the weak discharge spectrum. The degree of polarization of the 668 nm light is proportional to the nuclear spin polarization, with a pressure-dependent gauge factor given in [47]. The functioning of the OPD is described in detail in [26]. After the first polarization measurement the cell was left in the magnetic field for a time Δt (1-3 days), and then the gas discharge was re-ignited and the residual polarization P_{res} was measured. With the initial polarization P_{i} the T_1 time can be calculated according to

$$P_{\mathrm{res}} = P_{\mathrm{i}} \exp\left(-\frac{\Delta t}{T_1}\right) . \tag{3.1}$$

The T_1 times were measured to be between 14 h for a 1 mbar and 85 h for a 4.5 mbar cell. One could see a trend of increasing T_1 with increasing pressures, which is reasonable because for a field of 10 Gauss Eq. (2.34) is valid, i.e., the gradient relaxation time is proportional to the pressure. At the NMR-measurement that was done with pressures around 1 bar, the wall relaxation is the dominating term in T_1, while at low pressures of some mbar the

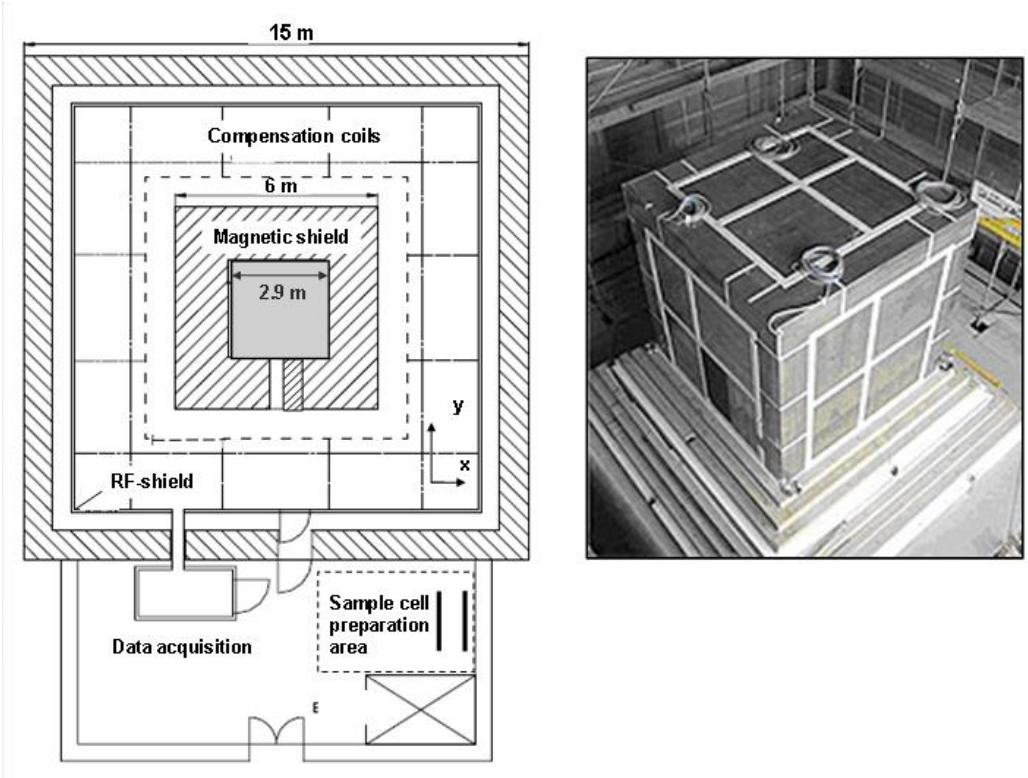

Figure 3.5: BMSR-2. *Left:* Horizontal cut view through building, shielded room and annex with data acquisition chamber and sample cell preparation area. *Right*: Mu-metal shielding during construction.

gradient relaxation starts to play a role. For some cells the T_1 times measured with the second method for the sealed cell is bigger than the one measured for the same cell in the NMR setup when the cell still had its appendix. This can be explained by the fact that the small appendix with a capillary of 3 mm diameter has a very bad surface-to-volume ratio, so that, according to Eq. (2.29), the gas relaxes quite fast in this region. The biggest T_1 of (85 ± 5) h (at 4.5 mbar) was measured for cell number Z10. This cell was used for the ^{3}He magnetometer measurements described in the following.

3.2 Experimental realization

The experiments with the ^{3}He magnetometer were done at the Physikalisch-Technische Bundesanstalt Berlin (PTB) in the *Berlin magnetically shielded room* (BMSR-2, [12]). With a residual field of less than 1 nT [75] and good field homogeneities, the BMSR-2 provides excellent conditions for measurements in the motional narrowing regime, i.e., at low pressures

and low magnetic fields (see Sec. 2.5), where it is possible to achieve T_2^* relaxation times for ^{3}He of several days. The cubic room with an inner edge length of 2.9 m consists of 7 layers of mu-metal[2] surrounded by a highly conductive eddy current layer made out of 10 mm aluminum. Its passive shielding factor exceeds 10^8 above 6 Hz, and with additional active shielding the room has a shielding factor of more than $7 \cdot 10^6$ down to 0.01 Hz. The complete shielding system is situated in a building with 15 m cubic outer dimension and a two-story annex with rooms for data acquisition and measurement preparation (see Fig. 3.5).

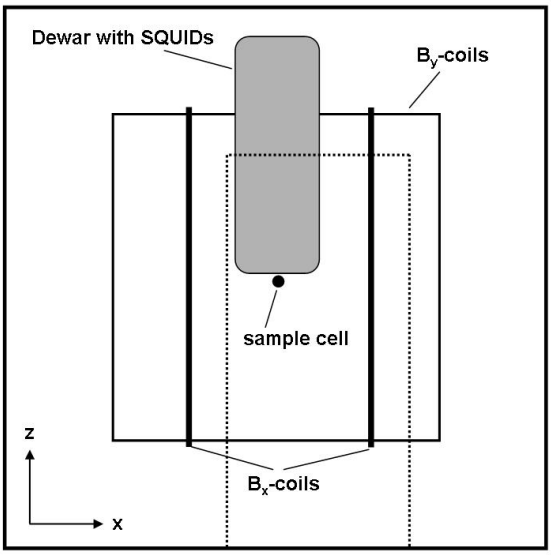

Figure 3.6: Experimental setup in the BMSR-2 (side view seen from the door opening). The outer open rectangle shows the inner shielding layer, the other open rectangles are the B_{x}- and B_{y}-coil pairs. The pneumatically driven sliding door is indicated by dashed lines. The gray rectangle is the Dewar housing the SQUID detectors, the small circle below the Dewar the sample cell (fixation not shown).

3.2.1 Experimental setup

The experimental setup is shown in Fig. 3.6. The SQUID[3] vector magnetometer system that was used for our experiments is installed permanently inside the BMSR-2, and has been originally designed for biomagnetic measurements. It is housed in a liquid-helium Dewar with a flat bottom and an inner diameter of 250 mm that is suspended from the

[2] Mu-metal is a nickel-iron alloy with very high magnetic permeability

[3] A SQUID (**S**uperconducting **Qu**antum **I**nterference **D**evice) is a highly-sensitive magnetic flux detector based on superconducting loops containing Josephson junctions. A more detailed description of SQUIDs can be found, for example, in [41].

ceiling. The 304 DC-SQUID magnetometers are divided up into 19 identical modules and are arranged in such a way that x-, y- and z-components of the magnetic field can be measured.

Inside the shielded room two square coil pairs (B_{x}- and B_{y}-coils) of edge length 180 cm and 175 cm were mounted perpendicular to each other, where the distance between the $B_{\mathrm{x(y)}}$-coils was 97(94) cm, respectively. Each coil pair (with $n = 20$ windings per coil) produced a homogeneous magnetic field of around 400 nT at a current of 20 mA, which was provided by a low noise current source[4]. The use of two coil pairs was chosen in order to manipulate the sample spins. A slow rotation of the magnetic field from B_{x} to B_{y} (or vice versa) causes an adiabatic rotation of the spins for $\Omega_{\mathrm{rot}}/\omega_{\mathrm{L}} \ll 1$, while for $\Omega_{\mathrm{rot}}/\omega_{\mathrm{L}} \gg 1$ the non-adiabatic condition is met (see Chap. 2.3). A fast rotation of the magnetic field was used to realize a "$\pi/2$-pulse". This way, nuclear spin-precession in the xz-plane (through a fast rotation from B_{x} to B_{y}) or, alternatively, in the yz-plane (through a fast rotation from B_{y} to B_{x}) could be monitored.

To choose the coil configuration that gives a good magnetic field homogeneity, a simulation was done with the program "Comsol32" (see App. C.1). All 9 gradient components of the simulated field, i.e., $\partial B_{\mathrm{x,y,z}}/\partial(x, y, z)$, were below 4 pT/cm. The magnetic field gradients were also measured by the SQUID magnetometer system itself (for a detailed description of the measurement procedure see [27]). The main uncertainty in the determination of the gradient components is the incorrect alignment of the Dewar and the fact that in presence of a magnetic guiding field this misalignment has a strong influence mainly on the extraction of the transverse components of the field gradient. From these measurements the absolute values of the gradient vectors for each field component were determined (see Tab. 3.1). The fact that the measured gradients are much higher than the simulated ones could be explained by an incorrect alignment and spacing of the coils. It is also possible that the Dewar itself was magnetized, which would have led to additional gradients. These gradients could not be detected with the SQUID system itself, because the SQUIDs have a fixed position relative to the Dewar. We know that the Dewar was magnetized during later measurements, and it cannot be excluded that it already was magnetized in December 2006, when the ^{3}He measurements described in this chapter were done.

[4]The current source is produced by "Magnicon" as part of the "SEL-1 SQUID Electronics"

$\left\vert\vec{\nabla}B_{1,\mathrm{x}}\right\vert$	$\left\vert\vec{\nabla}B_{1,\mathrm{y}}\right\vert$	$\left\vert\vec{\nabla}B_{1,\mathrm{z}}\right\vert$
$(32.7 \pm 3.5)\ \frac{\mathrm{pT}}{\mathrm{cm}}$	$(44.4 \pm 8)\ \frac{\mathrm{pT}}{\mathrm{cm}}$	$(27.0 \pm 0.8)\ \frac{\mathrm{pT}}{\mathrm{cm}}$

Table 3.1: Field gradients of the field produced by the B_{x}-coils in the BMSR-2, measured with the SQUID system itself during the ^{3}He precession measurements in Dec. 2006.

3.2.2 The measurement procedure

The sealed spherical sample cell (Z10 with radius $R = 3$ cm, $p_{\mathrm{he}} = 4.5$ mbar) with a longitudinal relaxation time $T_1 = (85 \pm 5)$ h was placed below the Dewar inside the B_{x} field as close as possible to a lower z-SQUID sensor. To reduce global magnetic field drifts, a lower and an upper z-SQUID was used in gradiometer configuration, i.e., we looked at the difference between the signals seen by the lower and the upper SQUID sensor. The distance from the center of the cell to the lower SQUID sensor was $d \approx 6$ cm, the one to the upper SQUID about 20 cm. As the ^{3}He magnetization drops with $1/r^3$, for the upper SQUID the ^{3}He precession signal is vanishingly small. So by building the difference between both SQUID signals, global magnetic field changes that are seen by both sensors are suppressed. The gas was optically pumped by means of a 2W Yb-doped fiber laser (wavelength: 1083 nm), where the fiber was laid through one of the holes in the mu-metal shielding. The optics to achieve a circularly polarized beam was mounted on an optical plate inside the shielding about 1 m away from the cell. The polarization build-up along the x-axis was monitored optically with the method described in Sec. 3.1. After switching off the discharge and laser light, a slow (adiabatic) rotation from B_{x} to B_{y}, followed by a fast (non-adiabatic) rotation back into the x-direction caused the spins first to orient themselves into the y-direction, and then to start to precess in the yz-plane. Now the door of the shielded room was closed, and the SQUID detection was started.

3.3 Results

The left side of Fig. 3.7 shows the recorded SQUID signal over a time interval of 0.5 s at the beginning of the precession cycle. The signal amplitude reaches $B_s = 12.5$ pT and the precession frequency $\nu \approx 13$ Hz. This corresponds to a magnetic field of $B_0 = \frac{2\pi\nu}{\gamma} \approx 401$ nT. With a noise level of about 3 fT/$\sqrt{\mathrm{Hz}}$ (see Sec. 4.1.4) this leads to a signal-to-noise ratio of $SNR = \frac{12500\ \mathrm{fT}}{3\ \mathrm{fT}} \approx 4167$ in a bandwidth of 1 Hz. With the help of Eq. (2.26) the achieved polarization can be calculated out of the signal amplitude to be $P \approx 15\%$.

On the right side of Fig. 3.7 the exponentially decaying envelope of the signal amplitude over

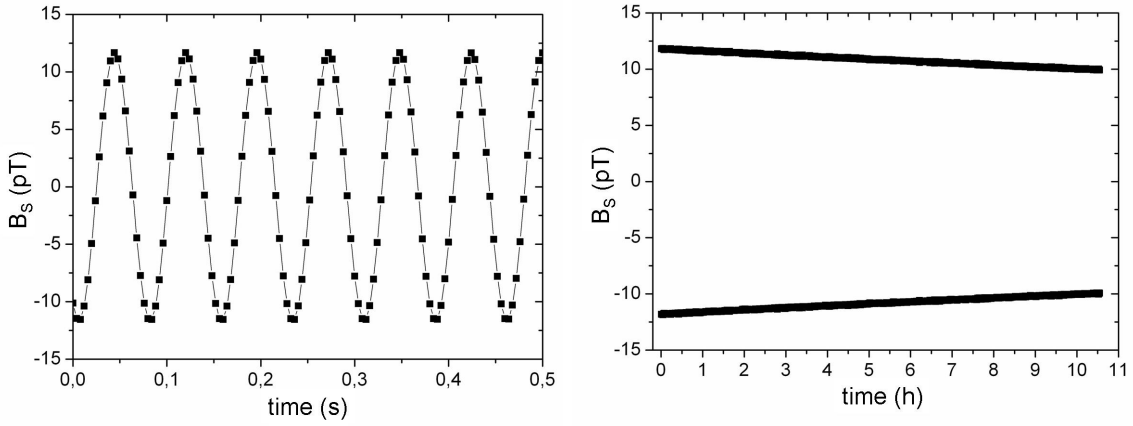

Figure 3.7: *Left*: ^{3}He precession signal recorded with a SQUID detector. *Right*: Envelope of the signal that shows a slow exponential decay corresponding to a T_2^* time of 60 hours.

a period of about 10 h is shown. From an exponential fit we get a transverse relaxation time of $T_2^* = (60.2 \pm 0.1)$ h, which is the longest coherent spin relaxation time of a macroscopic sample measured so far. Theoretically the T_2^* time can be calculated from Eq. 2.39, where the binary relaxation rate can be neglected for a pressure of 4.5 mbar. With $D_{\mathrm{He}} = 470\,\frac{\mathrm{cm}^2}{\mathrm{s}}$ (at p = 4.5 mbar), $B_0 = 401$ nT and the magnetic field gradients given in Tab. 3.1, the expected gradient relaxation time according to Eq. 2.40 is $T_{2,\mathrm{grad}} = (370 \pm 64)$ h. With the measured longitudinal relaxation time $T_1 = (85 \pm 5)$ h, the estimated total transverse relaxation time is $T_2^* = (\frac{1}{T_1} + \frac{1}{T_{2,\mathrm{grad}}})^{-1} = (69 \pm 4)$ h. This is very close to the measured T_2^*, which shows that the main sources of the transverse spin-relaxation are understood quantitatively. This result also demonstrates that even longer spin coherence times for ^{3}He can be obtained, and that our present value for T_2^* is mainly limited by the wall relaxation time $T_{1,\mathrm{wall}}$ of the sample cell. For future measurements the wall relaxation properties could be improved by using cells with a bigger radius and therewith better surface-to-volume ratio (see Eq. (2.29)), or with the help of a better demagnetization procedure.

3.4 Sensitivity estimation

The sensitivity of the ^{3}He-magnetometer can be estimated using the statistical signal processing theory described, e.g., in [39]. As the magnetic field is proportional to the precession frequency ν, the sensitivity for the magnetic field measurement can be deduced from the Cramer Rao lower bound (CRLB) that sets the lower limit on the variance of any frequency estimator. The signal S from the precessing spins consisting of N data points recorded at a

sampling rate r_s can be written as:

$$\begin{aligned} S[n] &= A \cdot e^{-\beta \cdot n} \cdot cos(2\pi(\nu/r_\mathrm{s})n + \phi) + \omega[n] \\ \text{with } n &= 0,\, 1, \cdots,\, N-1, \end{aligned} \tag{3.2}$$

where A is the amplitude, β the damping factor due to relaxation ($\beta = \frac{1}{r_\mathrm{s} T_2^*}$), ϕ the phase and $\omega[n]$ the White Gaussian Noise. For detection times $T \leq T_2^*$, where the exponential damping of the signal amplitude A does not affect the sensitivity of the magnetometer too much, we can use the average value $\overline{SNR} = \bar{A}/N_\alpha$ for the measured signal-to-noise ratio. The noise N_α is defined as the square root of the integrated power spectral density ρ_α of the corresponding signal fluctuations,

$$N_\alpha = \left(\int_0^{\nu_\mathrm{BW}} \rho_\alpha^2 \cdot d\nu \right)^{1/2} . \tag{3.3}$$

where $\nu_\mathrm{BW} = r_\mathrm{s}/2$ is the sampling rate limited bandwidth (Nyquist frequency). If the noise is white, i.e., $\rho_\alpha = const.$, the noise level is given by $N_\alpha = \rho_\alpha \sqrt{\nu_\mathrm{BW}}$. According to [39], the Cramer-Rao Lower Bound (CRLB), i.e., the lower limit for the variance σ_ν^2 of the frequency, is then given by:

$$\sigma_\nu^2 \geq \frac{12}{(2\pi)^2 \cdot (\bar{A}/N_\alpha)^2 \cdot \nu_\mathrm{BW} \cdot T^3} . \tag{3.4}$$

With Eq. (2.4) one can now derive the theoretical sensitivity δB for the measurement of the magnetic field B, which increases with the observation time T according to

$$\delta B \geq \frac{\sqrt{12}}{(\bar{A}/\rho_\alpha) \cdot T^{3/2} \cdot \gamma} . \tag{3.5}$$

This equation is valid for a sinusoidal signal with constant frequency and amplitude. In the appendix of Ref. [27] an improvement to the sensitivity estimate is given that takes the exponential damping of the precession signal into account.
The $T^{-3/2}$ dependency of Eq. (3.5), together with the measured T_2^* time of 60 hours and the signal-to-noise ratio $SNR \approx 4167$, leads to a magnetic field sensitivity of $\delta B \approx 2fT$ after an integration time of 200 s, which is roughly the typical cycle time in the neutron EDM experiment [1], and $\delta B \approx 10^{-4}$ fT after 24 hours. In Ref. [27] it is shown that the CRLB limit is actually reached. In order to prove this, ^{129}Xe is used as reference magnetometer in a clock comparison experiment, so that the magnetic field fluctuations are canceled out and one can study the remaining noise sources inherent to the magnetometer.

Chapter 4

Clock-comparison experiments with ^{3}He and ^{129}Xe

In the experiments described in this chapter, co-located polarized ^{3}He and ^{129}Xe spin samples are used to search for Lorentz-violating signatures by monitoring their Larmor precession frequencies (or phases) as the laboratory reference frame rotates with respect to distant stars. When looking at the weighted frequency difference, any dependence on magnetic field fluctuations should be canceled:

$$\begin{aligned} \Delta\omega(t) &= \omega_{\mathrm{he}}(t) - \frac{\gamma_{\mathrm{he}}}{\gamma_{\mathrm{xe}}}\omega_{\mathrm{xe}}(t) \\ &= \underbrace{(\gamma_{\mathrm{he}} - \frac{\gamma_{\mathrm{he}}}{\gamma_{\mathrm{xe}}}\gamma_{\mathrm{xe}})}_{0}\cdot B(t) + (1 - \frac{\gamma_{\mathrm{he}}}{\gamma_{\mathrm{xe}}})\cdot\omega_{\mathrm{LV}}(t) + \ \ldots\ , \end{aligned} \tag{4.1}$$

where $\omega_{\mathrm{he/xe}}$ are the Larmor frequencies of ^{3}He and ^{129}Xe, $\gamma_{\mathrm{he/xe}}$ their gyromagnetic ratios (see Sec. 4.3.2), $B(t)$ the magnetic field and $\omega_{\mathrm{LV}} = 2\pi\nu_{\mathrm{LV}} = \omega_{\mathrm{LV,he}} \approx \omega_{\mathrm{LV,xe}}$ the Lorentz-violating frequency shift according to Eq. (1.26). Since according to the Schmidt nuclear shell model (see, e.g., in [55]) ω_{LV} is roughly the same for ^{3}He and ^{129}Xe and does not depend on the gyromagnetic ratio, it does not drop out in the weighted frequency difference. As will be discussed in detail in Sec. 4.3, $\Delta\omega$ contains additional small terms that are not completely eliminated in the weighted frequency difference. Instead of the frequency difference one can as well consider the weighted phase difference,

$$\Delta\Phi(t) = \Phi_{\mathrm{he}}(t) - \frac{\gamma_{\mathrm{he}}}{\gamma_{\mathrm{xe}}}\Phi_{\mathrm{xe}}(t)\ , \tag{4.2}$$

with the phase being the time integral of the frequency, $\Phi(t) = \int_0^t \omega(t')dt' = \gamma\int_0^t B(t')dt'$.

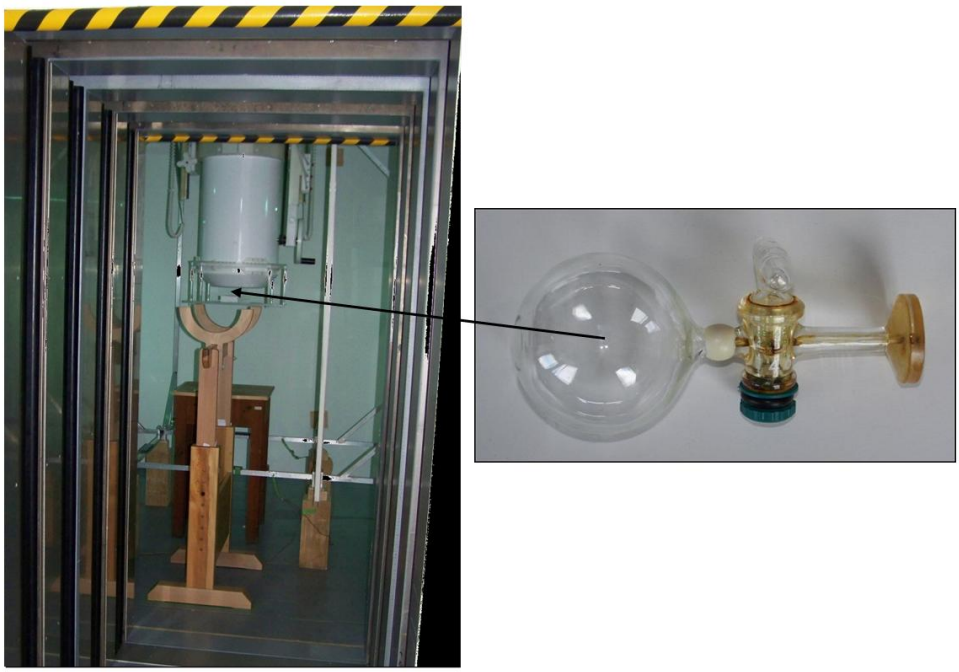

Figure 4.1: *Left:* View into the shielded room at PTB: The white Dewar is filled with liquid helium and contains the SQUID detectors. The quadratic coils made out of aluminum can be seen as well. The wooden support in front of the Dewar is used to hold the transport coil when the measurement cell is positioned on the cell holder made out of POM (Polyoxymethylen) that is fixed on the Dewar. *Right:* Cell (Z146) with stopcock and appendix that was used for the clock-comparison measurements.

4.1 Experimental realization

As well as the precession measurements with ^{3}He described in the preceding chapter, the clock-comparison measurements were performed in the magnetically shielded room BMSR-2 at PTB Berlin. The SQUID detection system was the same as described in Chap. 3.2.

4.1.1 Magnetic field

Fig. 4.1 shows a view inside the BMSR-2, with the white Dewar that contains the SQUID detectors, and the quadratic coil pairs for the magnetic guiding field. The measurement region directly below the Dewar was at (0, 0, -6.6 cm) (cell center), where (0, 0, 0) marks the center of the shielding (see as well Fig. C.2 in the appendix). For symmetry reasons it would have been better to place the cell as well as the coils in the shielding center, but this was not possible due to the dimensions of the Dewar which was already shifted up to its highest z-position. Simulations with "Comsol32" showed that for this position of the mea-

surement cell, a good field homogeneity is reached if the center of the $B_{x(y)}$-coils is shifted to (0, 0, -2 cm). These simulations are presented in App. C.1. The coils were changed slightly compared to the ^{3}He magnetometer measurements: the dimensions and distances were the same ($B_{x(y)}$-coils: length 180(175) cm, distance 97(94) cm), but the coils had $n = 40$ windings instead of 20. Moreover, the aluminum frame was cut at some point, and the two sides were separated by a non-magnetic and non-conducting PVC block. The reason for this was the fact that in previous measurements, small currents were induced in the aluminum frame, which produced stray fields that changed the field homogeneity. The number of windings was changed to have the opportunity to measure at higher field strengths than before, because this could lead to a reduced gradient relaxation according to Eq. (2.40). The current source used provides a maximal current of 25 mA, so with 40 windings a maximal field of about 1 μT could be reached. However, for the experiments described here (March 2009 runs), the coil was driven with 10 mA, which gives a field of about 400 nT, the same as in the measurements with the ^{3}He magnetometer. It was observed that a higher field strength did not improve the T_2^* times, and, furthermore, the noise in the region of the ^{3}He and ^{129}Xe frequency was worse at the higher field.
The magnetic field produced by the B_x-coils inside the BMSR-2 was measured in February 2009, some weeks before the clock-comparison experiments were accomplished[1]. The magnitude of the field was determined out of the Larmor precession frequency ν_{xe} of polarized ^{129}Xe gas inside a 6 cm diameter spherical cell via the formula $B = \frac{2\pi\nu_{xe}}{\gamma_{xe}}$, with γ_{xe} being the gyromagnetic ratio. The Larmor precession was measured at 10 different positions around the measurement region (0, 0, -6.6 cm), at two different heights, each with 5 measurement points (see Fig. C.3). The measured gradients in the x-y-plane laid between 1 pT/cm and 17 pT/cm, while in the z-direction values between 2 pT/cm and 48 pT/cm were measured. The results of the field measurements are presented in detail in App. C.2.

4.1.2 Filling system

To achieve good relaxation properties not only for ^{3}He but especially for ^{129}Xe, it is necessary to add a buffer gas, in our case N_2, to the gas mixture to suppress the van-der-Waals relaxation (see Chap. 2.5). To be able to fill different gases with varying pressures into the measurement cell, the cells for the clock-comparison experiments were not sealed but had an appendix with stopcock (see Fig. 4.1). The gases were also not polarized in-situ as in the experiment described before, but the already polarized gases were filled from low-relaxation

[1] As the coils used during the March run were not finished yet, the field was measured with older coils, which are in principle identical in construction, but do have only 20 instead of 40 windings. The field homogeneity, however, should not differ a lot between both coil systems.

storage vessels into the measurement cell. This was realized with a specially designed glass construction with 3 sluice valves with different volumes. Since it is very important that during the filling process the spin polarization of the gases is not destroyed due to magnetic field gradients, conventional valves can not be used, because they usually contain parts made out of magnetic materials. For this reason, the filling system was produced completely out of glass, because it is non-magnetic. To avoid gradients it is also necessary that the whole construction is placed in a homogeneous magnetic field, which is produced by a pair of Helmholtz coils with a diameter of 140 cm, which produce a field of $B_0 \approx B_z \approx 8.5$ G at a current of 5 A. The relative field gradient components $\frac{dB_z/dx}{B_z} = \frac{dB_z/dy}{B_z}$ and $\frac{dB_z/dz}{B_z}$ have been measured to be $\approx 10^{-4} \frac{1}{\mathrm{cm}}$ [48]. With the help of Eq. (2.30) the gradient relaxation times $T_{1,\mathrm{grad}}$ for ^{3}He and ^{129}Xe can be calculated. For relative gradients of the order $10^{-4} \frac{1}{\mathrm{cm}}$, a field of 8.5 G, and the typical storage cell pressures $p^{\mathrm{he}}_{\mathrm{stor}} \approx 2.1$ bar and $p^{\mathrm{xe}}_{\mathrm{stor}} \approx 1$ bar, one gets the values $T^{\mathrm{he}}_{1,\mathrm{grad}} = 5609$ h and $T^{\mathrm{xe}}_{1,\mathrm{grad}} = 80120$ h. Thus the gradient relaxation of the gases in the storage cells can be neglected.

The filling system, that is described in detail in [77], is shown in Fig. 4.2: Three storage vessels filled with N_2, polarized ^{3}He and polarized ^{129}Xe, respectively, at pressures of typically 1-2 bar, are connected to the flanges on one side of the glass construction. The ^{3}He gas was polarized at the Mainz polarizer to values of typically 70%. From there it was transported to the PTB in 1 liter storage vessels with wall relaxation times $T_{1,\mathrm{stor}}$ of typically 200 hours at a pressure $p_{\mathrm{stor}} \approx 2.1$ bar. Magnetized transport boxes provided a homogeneous field during transport [32]. As ^{129}Xe relaxes faster than ^{3}He, the ^{129}Xe gas was polarized at the PTB polarizer at any one time directly before the measurement. The flange on the upper right side in Fig. 4.2 is connected to a vacuum pumping system. The valves V1 and V2 can be opened to evacuate the system and are closed during the filling process. With the valves in the middle (SV1 -SV3), which work as sluices with different volumes, the desired gas quantity of either ^{3}He, ^{129}Xe or N_2 can be filled into the measurement cell that is connected to the upper left flange. A pressure sensor[2] with a non-magnetic sensor head measures the pressure in the measurement cell.

When choosing adequate pressures for the measurement, one has to weight between a high signal-to-noise ratio on the one hand, and good relaxation properties regarding both the gradient and the van der Waals relaxation on the other hand. In Fig. 4.3 the theoretical dependence of T_2 (disregarding the wall relaxation) with $\frac{1}{T_2} = \frac{1}{T_{2,\mathrm{grad}}} + \frac{1}{T_{1,\mathrm{vdW}}}$ is plotted as

[2]The "Vacuubrand" vacuum measurement "DCP 3000" with pressure sensor VSK 3000", with a specially fabricated non-magnetic sensor head out of aluminum

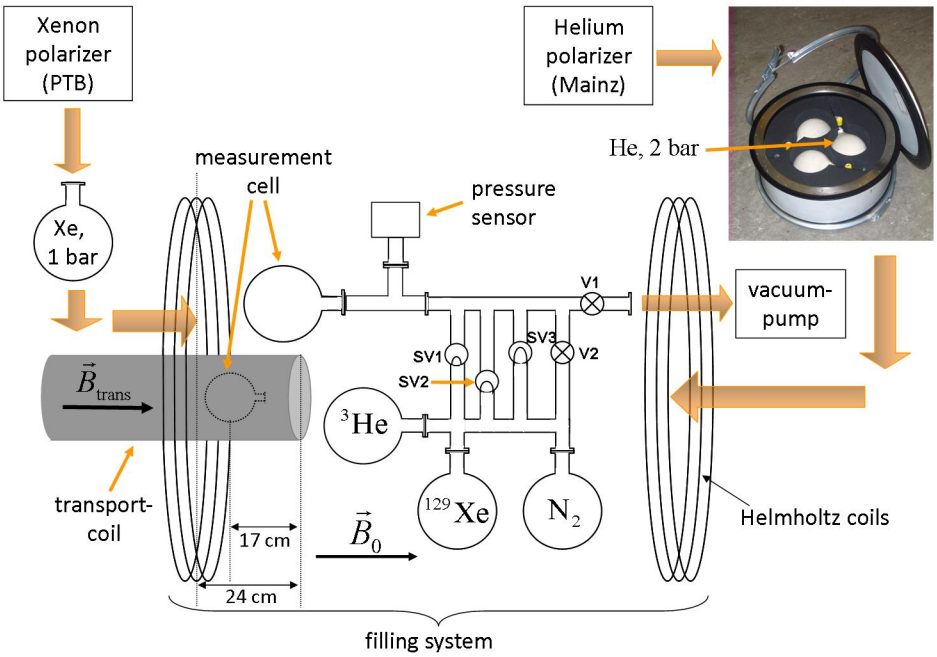

Figure 4.2: Scheme of the gas filling system (not true to scale): The polarized ^{3}He is transported from the Mainz polarizer to the PTB in Berlin via magnetized transport boxes [32], while ^{129}Xe is polarized at the PTB polarizer. The filling system made out off glass has three sluice valves in the middle (SV1, SV2 and SV3), with which different gas quantities can be filled into the measurement cell. Nitrogen is used as buffer gas to suppress the van-der-Waals relaxation. The whole system is situated inside a homogeneous Helmholtz field $\vec{B}_0$. To minimize polarization losses, care has to be taken regarding the correct positioning of the transport coil, which is used for the transport of the measurement cell to the shielded room (see Sec. 4.1.3).

a function of the N_2 buffer gas pressure in a ^{3}He/^{129}Xe gas mixture at fixed ^{3}He and ^{129}Xe pressures $p_{\mathrm{he}} = 4.1$ mbar and $p_{\mathrm{xe}} = 8.3$ mbar. For ^{3}He, the formation of van der Waals molecules can be neglected, i.e., $\frac{1}{T_{1,\mathrm{vdW}}} \approx 0$, so that the gradient relaxation time $T^{\mathrm{he}}_{2,\mathrm{grad}}$ decreases with increasing pressure. In case of ^{129}Xe , T_2^{xe} is maximal at N_2 partial pressures between 30 and 60 mbar. So for the long-term co-magnetometer measurements we chose pressures of about 4-9 mbar for ^{3}He, 8-9 mbar for ^{129}Xe, and about 30 mbar for N_2.

4.1.3 Transport of the polarized gases

The transport of the measurement cell from the filling region to the shielded room, as well as the transport of the ^{129}Xe storage cell from the polarizer lab to the filling

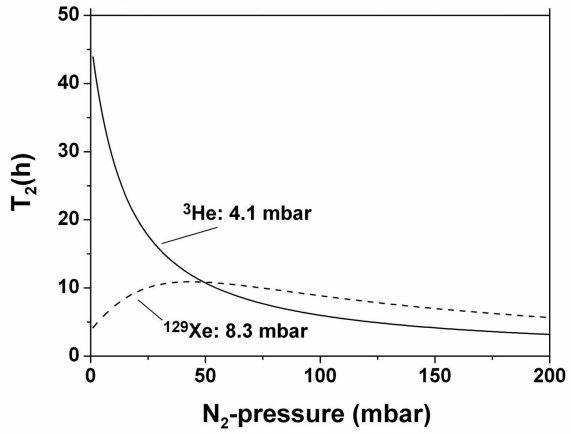

Figure 4.3: Calculated relaxation times $T_{2,\mathrm{he/xe}}$ due to gradient and van der Waals relaxation in a ^{3}He/^{129}Xe/N_2 gas mixture as a function of the nitrogen pressure, for $p_{\mathrm{he}} = 4.1$ mbar and $p_{\mathrm{xe}} = 8.3$ mbar.

system, was realized with a specially designed transport coil (see Fig. 4.4). It consists of an inner (i) and outer (o) solenoid of lengths $L = 60$ cm, with magnetic moments $M_{\mathrm{o}} = -M_{\mathrm{i}} = n_{\mathrm{o}}\, I_{\mathrm{o}}\, A_{\mathrm{o}}$, where n is the number of windings, I the current and A the cross section area. With the chosen values $n_{\mathrm{o}} = n_{\mathrm{i}}/2$, $I_{\mathrm{o}} = -I_{\mathrm{i}}$ and $A_{\mathrm{o}} = 2\, A_{\mathrm{i}}$, the resulting field is $B_{\mathrm{trans}} = B_{\mathrm{i}} + B_{\mathrm{o}} = \mu_0\, (n_{\mathrm{i}}/2)\, I_{\mathrm{i}}/L$. The voltage is provided by two 6 V batteries connected in series, leading to a field of about 3.6 G along the coil axis. Since the axial stray field of this double-solenoid system drops proportional to $1/z^5$, the fringe field of the transport coil reaches the 400 nT level already at a distance of $z \approx 30$ cm from the solenoid. This guarantees that the inner μ-metal walls are not magnetized while entering the shielded room, and therewith that the field gradients do not change too much from measurement to measurement.

In order to minimize polarization losses during transport, some things have to be paid attention to during the gas transport:

- Since the transport field is quite inhomogeneous at the ends of the transport coil, where the magnetic field lines bend, it is better to put the cell into and out of the coil while it is switched-off. During this time a homogeneous holding field is either provided by the Helmholtz coils of the filling system, or by the B_{y} coils inside the shielded room.

- To avoid spin flips during the switch-on (switch-off), it is necessary to slowly ramp up (down) the current in the coil, so that the field change happens adiabatically according

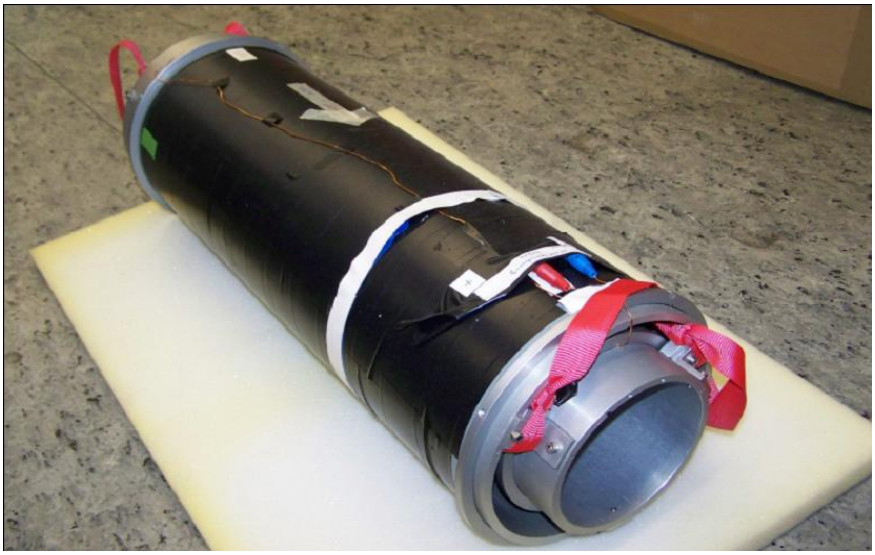

Figure 4.4: Transport coil for the transfer of the polarized gas from the filling station to the shielded cabin.

to Eq. (2.17). Therefore, the transport coil has a switch that slowly ramps up (down) the coil current, so that 10 seconds after pressing the switch the field inside the coil has increased to its maximal value (decreased to less than 0.1 nT, respectively).

- As magnetic field zero crossings can as well cause spin flips, it is very important that the transport coil is inserted into the coils of the filling system and the coils inside the shielded room in such a way that the magnetic field lines always point into the same direction.

The transport from the filling system to the shielded room happened as follows: After the measurement cell was filled with the desired gas mixture, the disabled transport coil was held into the Helmholtz coils, with both coils overlapping in a region of at least 24 cm (see Fig. 4.2). Then the cell was laid into the transport coil about 17 cm away from the coil edge, thus in a region where the field of the Helmholtz coils is still quite homogeneous. The coil was switched on, and after about 10 seconds, when the current reached its maximum value, was carried into the shielded cabin, with the B_y field switched on (see Fig. 3.6). There it was put onto a wooden support (see Fig. 4.1) on the same height as the measurement position, i.e., in a region where the homogeneity of the B_y field is quite good. After switching off the coil and waiting 10 seconds, the cell was taken out of the coil and placed below the dewar. Now the door of the shielded room was closed and the measurement was started.

4.1.4 Measurements

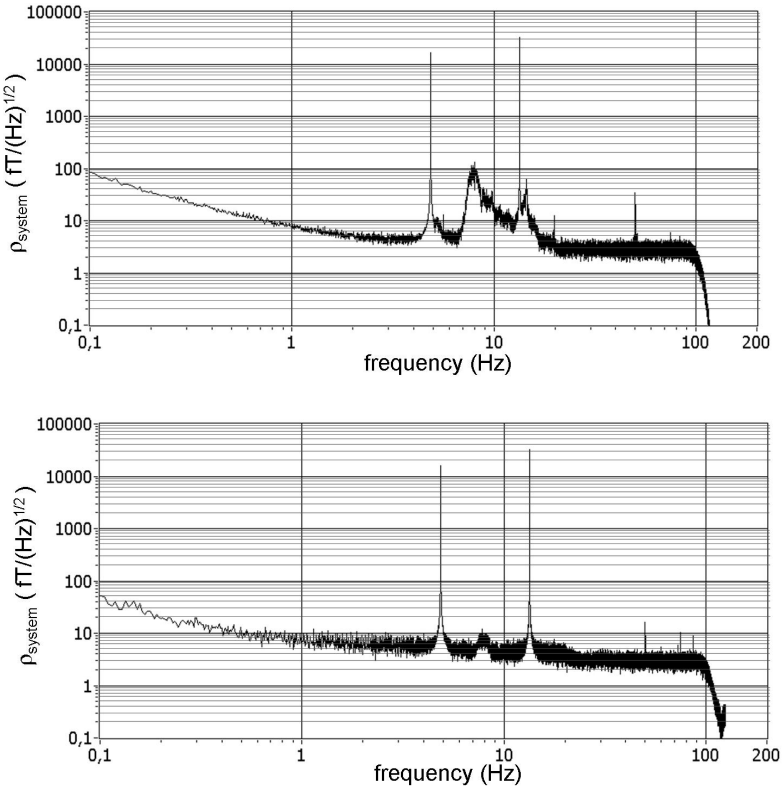

Figure 4.5: Magnetic flux density spectrum of the ^{3}He/^{129}Xe precession signal (run C92), detected with a single SQUID (*above*) and with a gradiometer (*below*). The upper spectrum shows big disturbances that are due to vibrations of the Dewar with respect to the measurement cell. The gradiometer suppresses the predominant part of the disturbances, and only a small peak at the main vibrational mode of about 8 Hz remains.

To force the spins to precess around the B_x-field, i.e., in the yz-plane, a non-adiabatic field rotation from B_y to B_x was used (see Chap. 3.2). The signals measured by different SQUID detectors in the lower and the upper level of the SQUID detection system were monitored. For the analysis later on a gradiometer signal was used, i.e., the difference of two z-SQUIDs, one in the lower and one in the upper level (see Chap. 3.2.2). This allows to suppress global magnetic field changes, for example microphonic effects that are due to the vibration of the Dewar relative to the measurement cell. In Fig. 4.5 two magnetic flux density spectra[3] (in units of fT/$\sqrt{\text{Hz}}$) are shown for measurement C92, the first one

[3]The density spectrum was determined with the *LabView8.5* utility routine *Spectral measurements*, using the Hamming window function. The first 2^{20} data points of C92 were used, and it was averaged over every

	t_0 (s)	t_{SD} (d)	T (h)	$B_{He}(t_0)$ (fT)	$B_{Xe}(t_0)$ (fT)	p_{He} (mbar)	p_{Xe} (mbar)	p_N (mbar)	p_{tot} (mbar)
C92	0	0.4051	14.61	8006	4818	4.1	8.3	29.3	41.7
C94	137554	0.0015	13.19	12880	3546	9.2	8.8	35.2	53.7
C95	186033	0.5641	15.00	22083	4138	9.3	8.8	32.8	51.4
C99	243779	0.2343	11.86	16173	3196	5.1	9.3	33.4	47.8
C101	302171	0.9120	13.80	29982	6269	5.2	9.6	34.2	49.6
C102	355491	0.5308	15.00	29699	5309	5.1	8.3	27.8	41.2
C103	417506	0.2505	15.95	12492	4838	5.0	8.3	26.0	39.3

Table 4.1: Parameters of the 7 main measurements: starting times t_0 relative to C92, Local Sidereal Time t_{SD} in units of days (see Chap. 4.4), observation times T, amplitudes of the precession signals $B_{He/Xe}$ at $t = t_0$, and pressures p of ^{3}He,^{129}Xe, N_2 and the total pressure in the measurement cell.

of the 7 long-term measurements. The upper plot is the spectrum for a single SQUID signal (sensor Z1E), whereas the lower one shows the spectrum for the gradiometer signal (sensors Z1E and Z9E). In addition to the ^{129}Xe and ^{3}He peaks at 4.9 Hz and 13.4 Hz, respectively, one can see a sharp peak at 50 Hz, as well as vibrational frequency components that partly overlap with the ^{129}Xe and ^{3}He peaks. In the case of the gradiometer, the vibrational frequencies are quite suppressed, and only a small peak at the main vibrational mode of about 8 Hz remains. The background noise level for both spectra is located at approximately 3 fT/$\sqrt{\text{Hz}}$. The fact that is falls down at $\approx$ 100 Hz is due to internal filters used in the SQUID electronics.

In total, seven long-term measurement runs (between 12 and 16 hours observation time) were performed during one week in march 2009. The parameters of these measurements (starting time, Local Sidereal Time, observation time, amplitudes and pressures) are listed in Tab. 4.1. From the amplitudes of the ^{3}He and ^{129}Xe SQUID signals at $t = t_0$ one can calculate the polarization according to Eq. (2.26). For ^{3}He, we had polarizations between 6% and 26%, for ^{129}Xe between 4% and 8%. In App. B the polarization losses due to the filling process and the transport from the filling station to the BMSR-2 are discussed.

The left side of Fig. 4.6 shows the precession signal for the first one of the measurements (C92), the superposition of the ^{3}He and ^{129}Xe precession at the Larmor frequencies $\nu_{he} = \frac{\gamma_{he}}{2\pi} B \approx 13.4$ Hz and $\nu_{xe} = \frac{\gamma_{xe}}{2\pi} B \approx 4.9$ Hz. With the help of a digital filter with a bandwidth of, e.g., 1 Hz, one can separate the signals of both gases as shown on the right side of the figure. It can be seen that for C92, the amplitudes at the beginning of the

20 points of the spectrum.

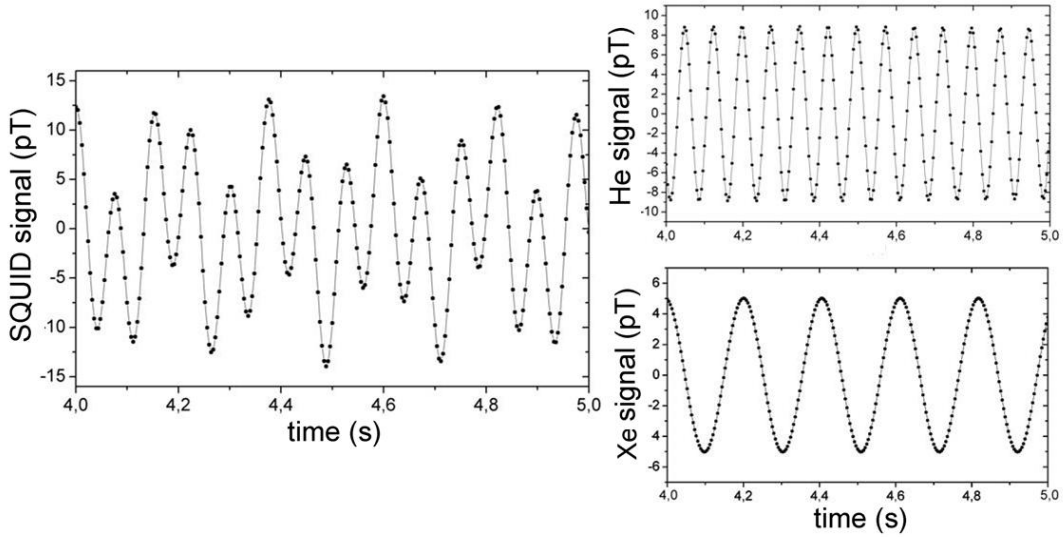

Figure 4.6: *Left*: ^{3}He and ^{129}Xe precession signal for measurement C92. *Right*: Precession signals for ^{3}He (above) and ^{129}Xe (below), separated through a digital filter (bandwidth 1 Hz) around 13.4 Hz and 4.9 Hz, respectively.

measurement were $B_{\mathrm{he}}(t_0) \approx 8$ pT and $B_{\mathrm{xe}}(t_0) \approx 4.8$ pT. From the magnetic flux density spectrum in Fig. 4.5 one can read a background noise level of about 3 fT/$\sqrt{\mathrm{Hz}}$, thus we have a signal-to-noise ratio at the beginning of run C92 of $\mathrm{SNR_{Xe}} = \frac{4800\ \mathrm{fT}}{3\ \mathrm{fT}} = 1600$ for ^{129}Xe and $\mathrm{SNR_{He}} = \frac{8000\ \mathrm{fT}}{3\ \mathrm{fT}} \approx 2667$ for ^{3}He in a bandwidth of 1 Hz.

4.2 Raw data fits, transverse relaxation and phase determination

To search for Lorentz-violating signatures the relevant quantity to examine is the weighted phase difference of Eq. (4.2). During data analysis we used two different methods for phase extraction. The first method we tried is the digital lock-in method that works in principle like a lock-in amplifier, as it uses frequency mixing to convert a higher-frequency to a low-frequency signal. After the mixing operation, which is accomplished in the time domain, the signal is Fourier transformed, then filtered through a Gaussian filter, and afterwards transformed back into time domain. Out of this mixed and filtered signal the phase is determined. This method works quite well for phase extraction, but it has one disadvantage: it is not clear how the Fourier transformations and the filtering change the errors of the data points. For this reason the phase errors have to be determined afterwards out of the scattering of the phase data. Thereby the filter has to be considered with a scaling factor, but it was not really clear how this scaling factor has to be determined. As we could not find a satisfying solution for the error determination, we later on used another method for phase extraction: the piecewise fitting of the raw data. Therefore, the SQUID signal is divided into data sets of length τ, and each of this data set is fitted to an equation that describes the ^{3}He and ^{129}Xe spin precession. The phase is then determined out of the best-fit-parameters. In this method no filtering or Fourier transformation is used. This has the advantage that the phase errors can be calculated straightforward out of the errors of the raw data using the error propagation law.

4.2.1 Piecewise fitting of raw data

The piecewise fitting of the raw data was performed with a *Mathematica* program developed by one of our collaborators from University of Heidelberg. The fitting routine is based on the standard Least-Squares method for multiple dimensions. A discrete pseudo-dimension is used to allow for the fitting of several measurement runs simultaneously, while specific fit parameters for each run can be implemented (see Sec. 4.4.2).

To extract the ^{3}He and ^{129}Xe phase developing, the SQUID (gradiometer) data of each run ($j = 1, \ldots, 7$ corresponding to C92, C94, C95, C99, C101, C102 and C103) are divided into sequential time intervals (i) of length $\tau = 3.2\,\mathrm{s}$ ($i = 1, \ldots, N_j$). The number of obtained sub-data sets laid between $13350 < N_j < 18000$ corresponding to observation times T_j of coherent spin precession in the range of $12\,\mathrm{h} < T_j < 16\,\mathrm{h}$. For each sub-data set a χ^2

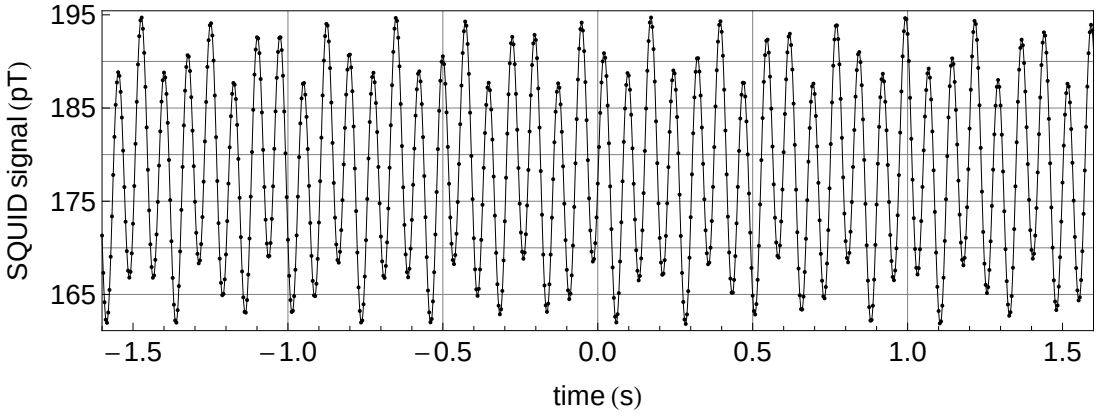

Figure 4.7: Typical sub-data set of 3.2 s length used for fitting

minimization was performed, using the fit-function

$$f^{\mathrm{i}}(t) = A^{\mathrm{i}}_{\mathrm{he}} \sin(\omega^{\mathrm{i}}_{\mathrm{he}} t) + B^{\mathrm{i}}_{\mathrm{he}} \cos(\omega^{\mathrm{i}}_{\mathrm{he}} t) + A^{\mathrm{i}}_{\mathrm{xe}} \sin(\omega^{\mathrm{i}}_{\mathrm{xe}} t) + B^{\mathrm{i}}_{\mathrm{xe}} \cos(\omega^{\mathrm{i}}_{\mathrm{xe}} t) + (c^{\mathrm{i}}_0 + c^{\mathrm{i}}_{\mathrm{lin}} t) \quad (4.3)$$

with a total of 8 fit-parameters. Within the relatively short time intervals, the term $(c^i_0 + c^i_{lin} \cdot t)$ represents the adequate parameterization of the SQUID offset showing a small linear drift due to the elevated $1/f$-noise at low frequencies (< 1 Hz). The sine and cosine terms describe the spin precession signal of the noble gas atoms with the frequencies $\omega^{\mathrm{i}}_{\mathrm{he/xe}}$. Instead of writing $C^{\mathrm{i}}_{\mathrm{he/xe}} \sin(\omega^{\mathrm{i}}_{\mathrm{he/xe}} t + \phi^{\mathrm{i}}_{\mathrm{he/xe}})$, it is better to use the sum of a sine and cosine term, because the amplitudes $A^{\mathrm{i}}_{\mathrm{he/xe}}$ and $B^{\mathrm{i}}_{\mathrm{he/xe}}$ are linear parameters, while the phase $\phi^{\mathrm{i}}_{\mathrm{he/xe}}$ in the other notation is nonlinear and therefore can lead to problems during the fitting, because nonlinear parameters are very sensitive on the initial values used for the fit. Both notations can be transformed into each other with the sine addition theorem,

$$\begin{aligned} C^{\mathrm{i}}_{\mathrm{he/xe}} \sin(\omega^{\mathrm{i}}_{\mathrm{he/xe}} t + \phi^{\mathrm{i}}_{\mathrm{he/xe}}) &= C^{\mathrm{i}}_{\mathrm{he/xe}} \sin(\omega^{\mathrm{i}}_{\mathrm{he/xe}} t) \cos(\phi^{\mathrm{i}}_{\mathrm{he/xe}}) + C^{\mathrm{i}}_{\mathrm{he/xe}} \cos(\omega^{\mathrm{i}}_{\mathrm{he/xe}} t) \sin(\phi^{\mathrm{i}}_{\mathrm{he/xe}}) \\ &= A^{\mathrm{i}}_{\mathrm{he/xe}} \sin(\omega^{\mathrm{i}}_{\mathrm{he/xe}} t) + B^{\mathrm{i}}_{\mathrm{he/xe}} \cos(\omega^{\mathrm{i}}_{\mathrm{he/xe}} t) \ , \end{aligned} \quad (4.4)$$

where $A^{\mathrm{i}}_{\mathrm{he/xe}} = C^{\mathrm{i}}_{\mathrm{he/xe}} \cos(\phi^{\mathrm{i}}_{\mathrm{he/xe}})$ and $B^{\mathrm{i}}_{\mathrm{he/xe}} = C^{\mathrm{i}}_{\mathrm{he/xe}} \sin(\phi^{\mathrm{i}}_{\mathrm{he/xe}})$ are termed the *quadrature amplitudes* of the oscillation.

In Fig. 4.7 a typical sub-data set is shown. It consists of 800 data points, which at our sampling rate of $r_{\mathrm{s}} = 250$ Hz corresponds to $\tau = 3.2$ s. The length for one sub-data set has to be chosen such that on the one hand the number of data points provide enough statistics for the fit, while on the other hand the ^{3}He and ^{129}Xe frequencies can be regarded as

constant and the SQUID offset drift as linear. The length $\tau = 3.2\ s$ fulfills these conditions. The time values for each sub-data set are always shifted in such a way that the zero-point lies in the middle of the sub-data set. The error for each data point was estimated to be 34 fT, which is the typical noise in the sampling rate limited bandwidth (Nyquist frequency) $f_{\mathrm{BW}} = f_{\mathrm{s}}/2 = 125$ Hz (with the sampling rate $f_{\mathrm{s}} = 250$ Hz). This can be seen in Fig. 4.5, where the magnetic flux density spectrum of run C92 is shown. The background noise is approximately 3 fT/$\sqrt{\mathrm{Hz}}$ at the ^{3}He and ^{129}Xe frequencies; this corresponds to a total noise of 3 fT/$\sqrt{\mathrm{Hz}} \cdot \sqrt{125\mathrm{Hz}} \approx 34$ fT.

From the flux density spectrum one can as well determine the starting values for the fit parameters $\omega^{\mathrm{i}}_{\mathrm{he}}$ and $\omega^{\mathrm{i}}_{\mathrm{xe}}$. As the fit model is nonlinear in the frequency, it is important to have good starting values, even for the linear parameters. For this reason the fit is accomplished in two steps: Firstly, the frequencies $\omega^{\mathrm{i}}_{\mathrm{he/xe}}$ are kept fixed at the values determined from the flux density spectrum. By this means, the model becomes linear, so that the starting values for the other parameters are not critical and the fit converges easily. Secondly, the best-fit-parameters from the first fit are chosen as starting values for the second fit, where now the frequencies can be varied as well. This method guarantees that one really reaches the minimal χ^2 in the nonlinear fit.

Best-fit parameters and uncertainties

The fit routine delivers the 8 best-fit parameters for each sub-data set, i.e., the ^{3}He and ^{129}Xe frequencies $\omega^{\mathrm{i}}_{\mathrm{he/xe}}$, the sine and cosine amplitudes $A^{\mathrm{i}}_{\mathrm{he/xe}}$ and $B^{\mathrm{i}}_{\mathrm{he/xe}}$, as well as the SQUID drift parameters c^{i}_0 and $c^{\mathrm{i}}_{\mathrm{lin}}$. The uncertainty of each parameter, that I will refer to as the *correlated error*, is given by the 1σ-error for this parameter, i.e., the interval that contains 68.3% of normally distributed data. Additionally, the *uncorrelated* error of each parameter is given by the fitting routine. This value corresponds to the uncertainty of the parameter if there would be no correlations between the parameters. In App. A more information is given about the error determination. The uncorrelated error is solely used for comparison with the correlated error, to get a feeling on the strength of the correlations between the parameters. If both errors are roughly equal, one can neglect the correlations. If they differ too much, one has to consider the correlations in the error propagation, i.e., the Gaussian error propagation law is not longer valid. In the case of the raw data fits, with sub-data sets consisting of 800 points, the correlations between the parameters are always small (the correlated and uncorrelated error differs by less than 10%), so that Gaussian

error propagation can be used[4] when determining the error of the phase later on (Sec. 4.2.5).

Moreover, the fit routine gives the reduced chi-square value (χ^2/dof) for each fit, as well as the probability Q that this value is due to chance, which is given by the integral over the probability density function (PDF) of the chi-square distribution,

$$Q = \int_{\chi^2_{\min}}^{\infty} PDF(x;\nu)dx \ . \tag{4.5}$$

In Fig. 4.8, where the PDF of the chi-square distribution for 15000 dof is shown, Q corresponds to the size of the gray area below the PDF curve. If this probability is smaller than 5%, i.e., for values of χ^2/dof that are too high, the routine automatically re-scales the error of the raw data with the factor $S = \sqrt{\chi^2/dof}$, so that a $\chi^2/dof = 1$ is reached, which also leads to larger errors of the best-fit parameters. This is a standard method often used in error determination, especially when the errors of the primary data are not known (see for example [62], Chap. 15.1).

The following section deals with the chi-square distributions for the 7 main measurements. Afterwards, in Sec. 4.2.3, some residuals of raw data fits are shown. Sec. 4.2.4 treats the decay of the ^{3}He and ^{129}Xe amplitudes with the transverse relaxation time T_2^*. Finally, in Sec. 4.2.5, the extraction of the ^{3}He and ^{129}Xe phases is described. These phases are then used to calculate the weighted phase difference of Eq. (4.2), which is the quantity of interest that is needed to determine the limits for the Lorentz-violating parameters (Sec. 4.4).

4.2.2 Chi-square distributions

For such a large number of degrees of freedom as in the case of our raw data fits ($dof > 10000$), the PDF of the chi-square distribution approaches a normal distribution with the mean value $\langle\chi^2/dof\rangle = 1$ and the standard deviation $\sigma_{\chi^2/dof} = \sqrt{2 \cdot dof - 1}/dof$ (see Fig. 4.8).

Looking at the chi-square distributions of the raw data fits of the 7 main runs (Fig. 4.9), we can see that the distributions are all much broader than the theoretical one, and that they are not symmetric, but have a tail at higher χ^2/dof values. For this reason the mean value $\langle\chi^2/dof\rangle$ is shifted to the right (indicated by the gray dashed line). Furthermore, there are some outliers where the χ^2/dof is ≥ 2 (not shown in the figures). In Tab. 4.2

[4] Another requirement for the validity of Gaussian error propagation is the possibility of linearising the fit model in a region around the minimal chi-square, which is fulfilled in our case.

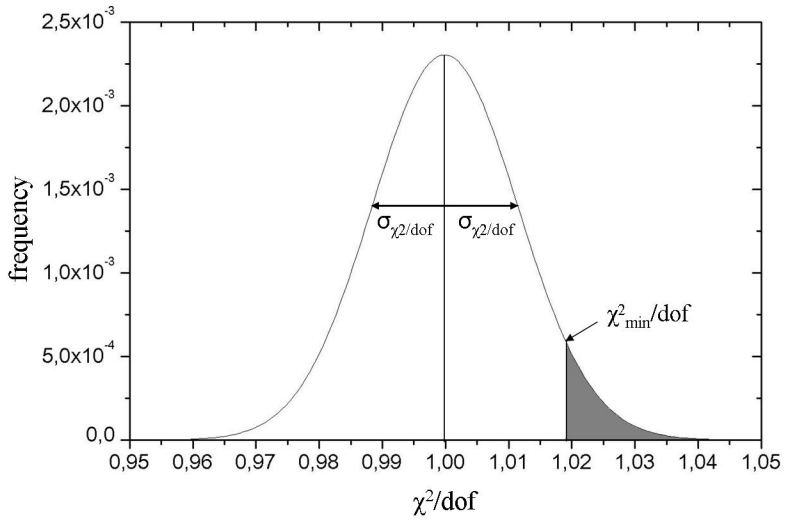

Figure 4.8: Probability density function of the chi-square distribution for 15000 degrees of freedom. The mean value is $\langle \chi^2/dof \rangle = 1$ and the standard deviation $\sigma_{\chi^2/dof} = \sqrt{2dof - 1}/dof$. The gray area corresponds to the chi-square probability Q given in Eq. (4.5).

the number of sub-data sets with $\chi^2/dof \geq 2$ is listed for the 7 main measurements. The main reason for these outliers lies in the fact that in some sub-data sets the SQUID offset jumps slightly for so far unknown reasons (see Sec. 4.2.3). Additionally, as was seen already in the magnetic flux density spectrum (Fig. 4.5) and will be illustrated again in Sec. 4.2.3, we had disturbance frequencies in the raw data due to vibrations of the Dewar relative to the measurement cell. The strength of these disturbances can fluctuate during the measurement, which is the main reason for the broader distributions.

In Fig. 4.9 and Tab. 4.2 one can see that the mean chi-square value is approximately 1 only for the runs C94 and C95. For run C103 it is smaller than 1 ($< \chi^2/dof >= 0.91$), while for the other runs it is slightly bigger (between 1.11 and 1.22). As explained in the preceding section, the error for each data point was estimated from the background noise that can be read out of the flux density spectrum to be ≈ 34 fT in the sampling rate limited bandwidth $f_{\mathrm{BW}} = 125$ Hz (see Fig. 4.5). Due to the fact that the noise changes from run to run (and also in the course of one run), the value of 34 fT is not the true error for all data points in all 7 runs. This is the reason why $< \chi^2/dof >$ fluctuates from measurement to measurement: for run C103 the error was overestimated, while for the runs C92, C99, C101 and C102 it was underestimated. For the further analysis, however, this is not a problem, because the fitting routine automatically re-scales the error for each fit if the chi-square

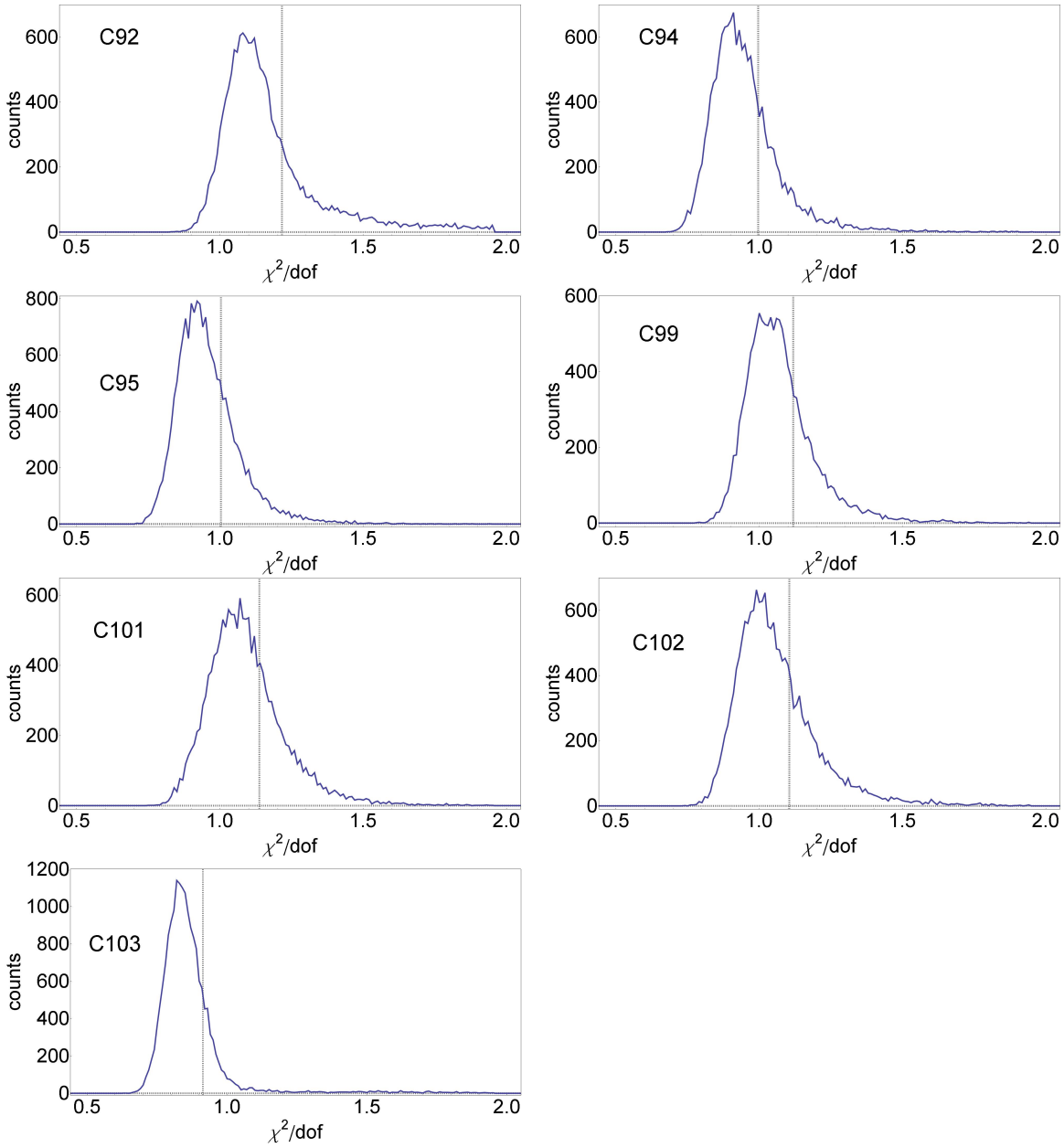

Figure 4.9: Chi-square distributions of the raw data fits of the 7 main measurements: The gray dashed line indicates the mean chi-square value $\langle \chi^2/dof \rangle$, which is shifted to the right due to the tail at higher χ^2/dof values. The χ^2/dof values that are ≥ 2 are not included in the mean value.

probability Q, i.e., the probability that the error of the data points reflects the statistical noise, is smaller than 5% (see preceding section and App. A).

	$< \chi^2/dof >$	$\sigma_{\chi^2/dof}$	#(fits)	$\#(\chi^2/dof \geq 2)$
C92	1.216	0.179	16437	995
C94	0.996	0.124	14835	17
C95	1.004	0.112	16875	8
C99	1.118	0.123	13348	24
C101	1.137	0.136	15522	28
C102	1.105	0.143	16875	45
C103	0.914	0.136	17938	98

Table 4.2: Overview over the χ^2 statistics for the raw data fits: mean and standard deviation of the chi-square distribution (sub-data sets with $\chi^2/dof \geq 2$ are not included), total number of fits and the number of sub-data sets that were discarded because of a $\chi^2/dof \geq 2$.

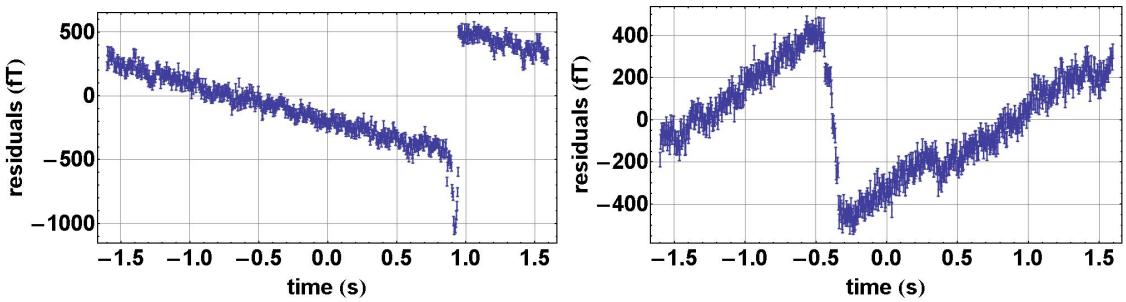

Figure 4.10: Residuals of raw data fits with a $\chi^2 \geq 2$: The data shows jumps in the SQUID amplitude in the order of 1 pT.

To assure the usage of solely "good data" for the fit of the weighted phase difference, the sub-data sets with $\chi^2/dof \geq 2$ were discarded for the further analysis. For measurement C92, which had the most disturbances, about 6% of the sub-data sets were discarded; for the other measurements it was less than 0.5% of the data.

4.2.3 Raw data residuals

The jumps in the SQUID amplitude as well as the disturbance frequencies due to the vibrations of the Dewar can also be seen by looking at the residuals of the raw data fits, that are determined by subtracting the fitted function from the data. In Fig. 4.10 two examples of sub-data sets with offset jumps in the order of 1 pT are shown. It is obvious that for these sub-data sets the model (4.3) does not fit, which leads to a large χ^2/dof. These sub-data sets were discarded for the further analysis.

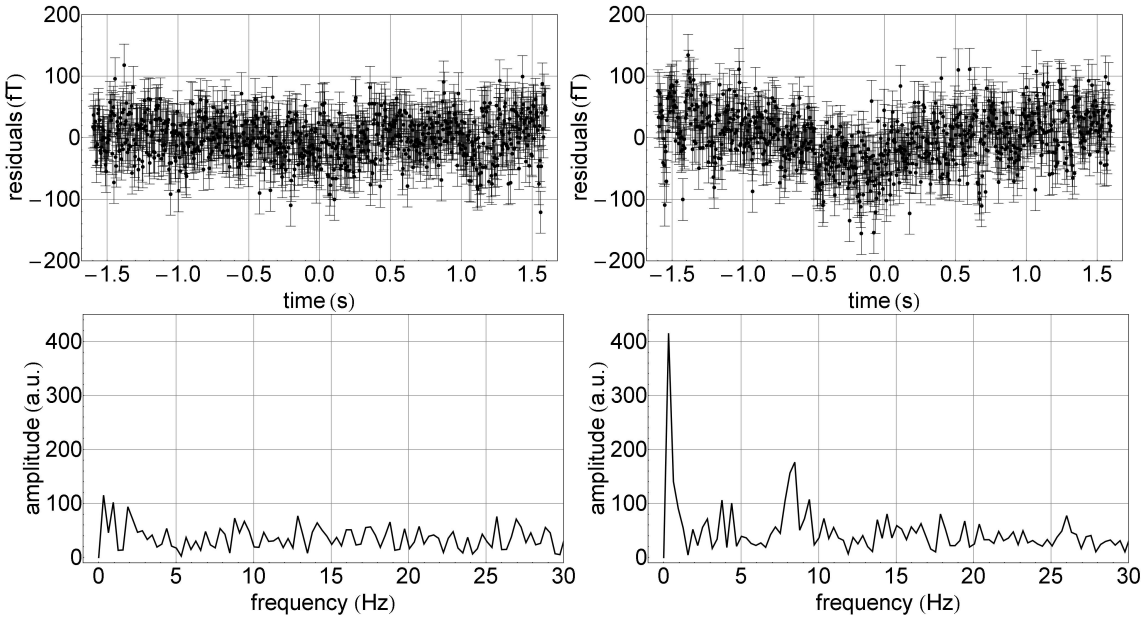

Figure 4.11: Residuals of two raw data fits of run C92 with $\chi^2/dof = 1.05$ (*upper left*) and $\chi^2/dof = 1.75$ (*upper right*). *Below*: Parts of the respective Fourier spectra. For the sub-data set shown at the left-hand side the disturbances are small, while the spectrum at the right-hand side has peaks at about 0.5 Hz and 8 Hz. The latter frequency is the main vibration mode of the Dewar that was already seen in the magnetic flux density spectrum in Fig. 4.5. The peak at 0.5 Hz is due to the change in the offset drift that can be seen in the residuals plot. The different magnitudes of the disturbances are reflected in the different reduced chi-squares of the two fits.

The upper part of Fig. 4.11 shows the residuals for two of the "good" sub-data sets of run C92, one with $\chi^2/dof = 1.05$ and another one with $\chi^2/dof = 1.75$. One can see that the residuals still show some structure and are not normally distributed. The reason for this are nonlinearities in the offset drift, as well as additional frequency components that are contained in the spectrum. This is illustrated in the lower part of Fig. 4.11, where parts of the respective Fourier spectra of the residuals are shown. For the sub-data set with $\chi^2/dof = 1.05$ shown at the left-hand side, the disturbances are small, while the spectrum at the right-hand side (larger χ^2/dof) has peaks at about 0.5 Hz and 8 Hz. The latter frequency is the main vibration mode of the Dewar, which was already seen in the magnetic flux density spectrum in Fig. 4.5. The peak at 0.5 Hz is due to the change in the offset drift that can be seen in the residuals plot. Although the gradiometer signal is used, these disturbances, whose strengths change in the course of the measurement, can not be eliminated completely. To take these frequencies into account one could add another sine/cosine function with a third frequency component to the fit model. This was tried during analysis, but it did not lead

	$T^*_{2,\mathrm{he}}$(s)	$\delta T^*_{2,\mathrm{he}}$(s)	$T^*_{2,\mathrm{xe}}$(s)	$\delta T^*_{2,\mathrm{xe}}$(s)
C92	50899.6	0.77	15835.2	0.62
C94	30293.3	0.35	14745.5	0.55
C95	29986.1	0.15	14102.3	0.34
C99	28159.4	0.17	14406.7	0.54
C101	25655.0	0.12	11413.8	0.45
C102	31235.6	0.14	12110.5	0.32
C103	34434.9	0.24	13057.7	0.31

Table 4.3: Transverse relaxation times of measurements C92-C103.

to better results in total. Indeed, the χ^2/dof then becomes better for some fits, so that the chi-square distributions are more symmetric. But with this third frequency component the fitting takes much longer, and sometimes the fit does not converge at all. As the values for the best-fit parameters do not differ significantly for the two models, it was at last decided to use the simpler model of Eq. (A.1).

4.2.4 Transverse relaxation time and field gradients

The ^{3}He and ^{129}Xe amplitudes are calculated out of the fit parameters as

$$C^{\mathrm{i}}_{\mathrm{he/xe}} = \sqrt{(A^{\mathrm{i}}_{\mathrm{he/xe}})^2 + (B^{\mathrm{i}}_{\mathrm{he/xe}})^2} \ . \tag{4.6}$$

The amplitude errors $\delta C^{\mathrm{i}}_{\mathrm{he/xe}}$ are determined via Gaussian error propagation. In Fig. 4.12 the amplitude developing for run C92 is plotted, which shows the decay due to the transverse relaxation (the error bars are too small to be visible in the plot). The T^*_2 times can be determined with the help of an exponential fit. Because of the long measurement time, the fit gives very small uncertainties: δT^*_2 is smaller than 1 s for all runs. The results for the measurements C92-C103 are shown in Tab. 4.3. For measurement C92 the biggest T^*_2 times were observed ($T^*_{2,\mathrm{he}} = 14.14$ h and $T^*_{2,\mathrm{xe}} = 4.40$ h), while for the other measurements the relaxation times were between 7.13 h and 9.57 h for ^{3}He, and 3.17 h and 4.10 h for ^{129}Xe.

To compare these values with the theoretical prediction according to Eq. (2.39) and Eq. (2.40), let us look at the magnetic field gradients of the B_{x}-field measured in February 2009 with two ^{129}Xe cells (see Sec. 4.1.1 and App. C.2). As with this method only the magnitude of the field can be measured, the single components of the field gradient are not known. From the Maxwell equations div $\vec{B} = 0$ and rot $\vec{B} = 0$ one can conclude that only 6 independent

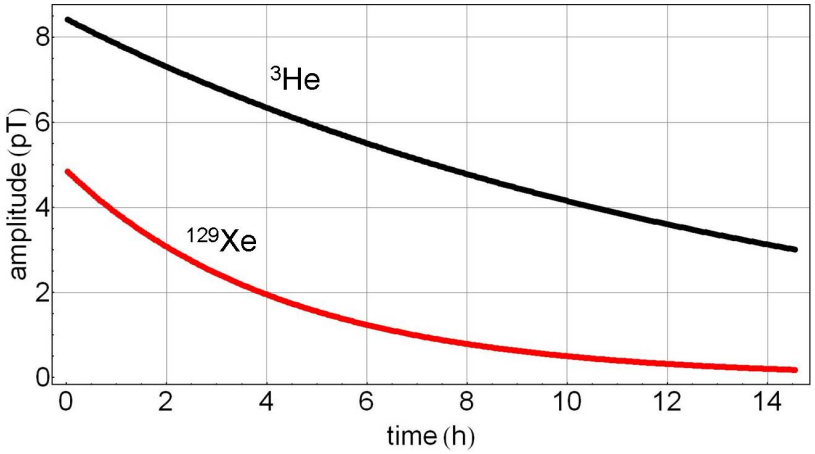

Figure 4.12: Decay of the ^{3}He and ^{129}Xe amplitudes of run (1). The error bars are too small to be visible in the plot.

gradient components exist, i.e.,

$$\left|\frac{\partial B_\mathrm{x}}{\partial z}\right| = \left|\frac{\partial B_\mathrm{z}}{\partial x}\right|, \quad \left|\frac{\partial B_\mathrm{y}}{\partial x}\right| = \left|\frac{\partial B_\mathrm{x}}{\partial y}\right| \quad \text{and} \quad \left|\frac{\partial B_\mathrm{y}}{\partial z}\right| = \left|\frac{\partial B_\mathrm{z}}{\partial y}\right|.$$

Now let's assume similar sizes of the x- and y-gradients on the one hand, and of the z-gradients on the other hand, i.e., $G_{xy} := \left|\frac{\partial B_\mathrm{x}}{\partial y}\right| = \left|\frac{\partial B_\mathrm{y}}{\partial x}\right| \approx \left|\frac{\partial B_\mathrm{x}}{\partial x}\right| \approx \left|\frac{\partial B_\mathrm{y}}{\partial y}\right|$ and $G_z := \left|\frac{\partial B_\mathrm{x}}{\partial z}\right| = \left|\frac{\partial B_\mathrm{z}}{\partial x}\right| \approx \left|\frac{\partial B_\mathrm{y}}{\partial z}\right| = \left|\frac{\partial B_\mathrm{z}}{\partial y}\right| \approx \left|\frac{\partial B_\mathrm{z}}{\partial z}\right|$. To do a conservative estimation, we take the worst of the measured values, i.e., $G_{xy} \approx 17$ pT/cm for the x-y-plane and $G_z \approx 48$ pT/cm for the z-direction (see Fig. C.3 in the appendix). Now the theoretical gradient relaxation time for measurement C92, with the (inner) cell radius $R = 2.9$ cm, $B_0 \approx 400$ nT and the ^{3}He diffusion coefficient according to Eq. (2.31) (with the pressures given in Tab. 4.1), can be calculated according to Eq. (2.40) to be $T^\mathrm{He}_\mathrm{2,grad} \approx 13.0$ h and $T^\mathrm{Xe}_\mathrm{2,grad} \approx 18.4$ h. The wall relaxation times for ^{3}He and ^{129}Xe for the clock-comparison measurement cell (Z146) were measured beforehand in a conventional NMR setup to be $T^\mathrm{He}_\mathrm{1,wall} \approx 130$ h and $T^\mathrm{Xe}_\mathrm{1,wall} \approx 16$ h. Together with the binary relaxation according to Eq. (2.35) and (2.36), as well as the van der Waals relaxation for ^{129}Xe (Eq. (2.38)), the total theoretical relaxation times for measurement C92 according to Eq. (2.39) are $T^\mathrm{*,cal}_\mathrm{2,he} \approx 11.8$ h and $T^\mathrm{*,cal}_\mathrm{2,xe} \approx 5.9$ h. For ^{3}He this is a bit smaller than the measured value of 14.14 h, for ^{129}Xe the measured value was 4.40 h, i.e., the theoretical prediction is too high. As for ^{3}He, with $T^\mathrm{He}_\mathrm{1,wall} > 100$ h, the gradient relaxation surely is the dominant mechanism, one can draw the conclusion that the gradients above are rather over- than underestimated. This gives rise to the assumption that the wall relaxation for ^{129}Xe in reality was much smaller

than 16 hours, if there exist no other relaxation mechanism that was not regarded. For ^{3}He it was observed that the wall relaxation time for some cells fluctuated strongly from one NMR measurement to another. The reason for this is not yet known, perhaps it could be magnetic impurities that somehow get into the cell. That's why the error in the wall relaxation time has to be regarded as quite high.

To get a more realistic estimation of the gradients and $T^{\mathrm{xe}}_{1,\mathrm{wall}}$ during run (1), one can use the measured transverse relaxation times. Therefore, we take again Eq. (2.40) for ^{3}He and assume for the moment that all gradient components are equal, i.e., $G := |\vec{\nabla}B_{1,\mathrm{x}}| = |\vec{\nabla}B_{1,\mathrm{y}}| = |\vec{\nabla}B_{1,\mathrm{z}}|$. By solving Eq. (2.40) for G and inserting the measured $T^*_{2,\mathrm{he}}$ of 14.14 h, together with the ^{3}He parameters given above for run (1), we get $G = 48.8$ pT/cm. If we insert this value of G again in Eq. (2.40), together with the ^{129}Xe parameters of run (1), the gradient relaxation time becomes $T^{\mathrm{xe}}_{2,\mathrm{grad}} = 22.8$ h. Using Eq. (2.28), with the measured $T^*_{2,\mathrm{xe}}$ of 4.4 h for run (1), we then get a wall relaxation time of $T^{\mathrm{xe}}_{1,\mathrm{wall}} \approx 7.7$ h.

The reason for the fluctuations in the T_2^* times from run to run (see Tab. 4.3) is assumed to be changes in the magnetic field gradients. In between run C92 and C94, where the biggest changes were observed, the Dewar was refilled with liquid helium. During this procedure the square coil pairs were possibly shifted, which would have led to a change in the orientation of the magnetic guiding field and therewith a change in the field homogeneity. Another reason could be additional gradients that are produced by ^{3}He and ^{129}Xe demagnetization fields, which would also change from run to run due to changes in the pressures, polarizations and the orientation of the cell appendix (see Sec. 4.3.3).

4.2.5 Phase determination

To determine the limit for Lorentz violation, the quantity of interest is the accumulated ^{3}He and ^{129}Xe phase for the *ith* sub-data set, $\Phi^{\mathrm{i}}_{\mathrm{he/xe}} = n^{\mathrm{i}}_{\mathrm{he/xe}} \cdot 2\pi + \varphi^{\mathrm{i}}_{\mathrm{he/xe}}$, with $i = 1, \ \ldots, \ N$, where N is the total number of sub-data sets for the corresponding measurement run. The part of the phase that lies between zero and 2π, $\varphi^{\mathrm{i}}_{\mathrm{he/xe}}$, is determined from the fit parameters $A^{\mathrm{i}}_{\mathrm{he/xe}}$ and $B^{\mathrm{i}}_{\mathrm{he/xe}}$ using the arctangent (atan2) function, that is defined the following way:

$$\mathrm{atan2}(y,x) = \begin{cases} \arctan(\frac{y}{x}) & x > 0, \\ \pi + \arctan(\frac{y}{x}) & y \geq 0, \ x < 0 \ , \\ -\pi + \arctan(\frac{y}{x}) & y < 0, \ x < 0 \ . \end{cases} \tag{4.7}$$

Hence, the value of atan2 depends on the quadrant of the x and y phase vectors in the unit circle, and takes values in the interval from $-\pi$ to π. To assure that $\varphi^{\mathrm{i}}_{\mathrm{he/xe}}$ does not take negative values (to avoid phase wraps later on), the value π is added to Eq. (4.7):

$$\varphi^{\mathrm{i}}_{\mathrm{he/xe}} = \mathrm{atan2}\left(\frac{A^{\mathrm{i}}_{\mathrm{he/xe}}}{B^{\mathrm{i}}_{\mathrm{he/xe}}}\right) + \pi \ . \tag{4.8}$$

To determine the total, running phase of ^{3}He and ^{129}Xe, one also needs to know the number of traversed periods $n^{\mathrm{i}}_{\mathrm{he/xe}}$ since the beginning of the measurement run. $n^{\mathrm{i}}_{\mathrm{he/xe}}$ is determined indirectly in the following way: In a first step, an estimation of the accumulated phase of the *ith* sub-data set $\Phi^{\mathrm{est,i}}_{\mathrm{he/xe}}$ is done using the phase of the *(i-1)th* sub-data set $\Phi^{\mathrm{i-1}}_{\mathrm{he/xe}}$ (where the phase offset of the first data set is $\Phi^{1}_{\mathrm{he/xe}} = \varphi^{1}_{\mathrm{he/xe}}$):

$$\Phi^{\mathrm{est,i}}_{\mathrm{he/xe}} = \Phi^{\mathrm{i-1}}_{\mathrm{he/xe}} + \bar{\omega}_{\mathrm{he/xe}} \cdot \tau \ . \tag{4.9}$$

Here $\tau = 3.2$ s is the length of one sub-data set, and $\bar{\omega}_{\mathrm{he/xe}}$ the average frequency of the corresponding run, which consists of N sub-data sets,

$$\bar{\omega}_{\mathrm{he/xe}} = \frac{1}{N}\sum_{i=1}^{N} \omega^{\mathrm{i}}_{\mathrm{he/xe}} \ . \tag{4.10}$$

Due to the fact that the frequency stays more or less constant during the course of one run, the maximal frequency deviation ($\Delta\omega_{\mathrm{max}}$) from the mean $\bar{\omega}_{\mathrm{he/xe}}$ was smaller than $5 \cdot 10^{-6}$ rad/s (both for ^{3}He and ^{129}Xe) for all 7 runs. Hence, as $\Delta\omega_{\mathrm{max}} \ll 2\pi$, the accumulated phase between the middle of data set $(i-1)$ and the middle of data set i is estimated quite well with $\bar{\omega}_{\mathrm{he/xe}} \cdot \tau$. Anyhow, to get the true accumulated phase $\Phi^{\mathrm{i}}_{\mathrm{he/xe}}$ of the actual sub-data set, the estimation $\Phi^{\mathrm{est,i}}_{\mathrm{he/xe}}$ has to be corrected by the term

$$\Delta\Phi^{\mathrm{corr,i}}_{\mathrm{he/xe}} = \varphi^{\mathrm{i}}_{\mathrm{he/xe}} - \mathrm{mod}\left(\frac{\Phi^{\mathrm{est,i}}_{\mathrm{he/xe}}}{2\pi}\right) \ . \tag{4.11}$$

The accumulated phase $\Phi^{\mathrm{i}}_{\mathrm{he/xe}}$ is then given by:

$$\begin{aligned} \Phi^{\mathrm{i}}_{\mathrm{he/xe}} &= \Phi^{\mathrm{est,i}}_{\mathrm{he/xe}} + \Delta\Phi^{\mathrm{corr,i}}_{\mathrm{he/xe}} \\ &= \Phi^{\mathrm{i-1}}_{\mathrm{he/xe}} + \bar{\omega}_{\mathrm{he/xe}} \cdot \tau \ + \varphi^{\mathrm{i}}_{\mathrm{he/xe}} - \mathrm{mod}\left(\frac{\Phi^{\mathrm{i-1}}_{\mathrm{he/xe}} + \bar{\omega}_{\mathrm{he/xe}} \cdot \tau}{2\pi}\right) \ . \end{aligned} \tag{4.12}$$

Here the number of traversed periods $n^{\mathrm{i}}_{\mathrm{he/xe}}$ corresponds to the integer value of $\Phi^{\mathrm{est,i}}_{\mathrm{he/xe}}$

divided by 2π.

A problem can now occur in the cases where the phase $\varphi^{\mathrm{i}}_{\mathrm{he/xe}}$ (Eq. (4.8)) is either close to zero or close to 2π. If the former case is given, and if in addition $\bar{\omega}_{\mathrm{he/xe}}$ is *smaller* than the real frequency of the sub-data set, it happens that one underestimates the number of periods $n^{\mathrm{i}}_{\mathrm{he/xe}}$ by one, i.e., a phase wrap appears. On the other hand, if $\varphi^{\mathrm{i}}_{\mathrm{he/xe}}$ is close to 2π and $\bar{\omega}_{\mathrm{he/xe}}$ *bigger* than the real frequency, $n^{\mathrm{i}}_{\mathrm{he/xe}}$ is overestimated. In these cases the correction phase $\Delta\Phi^{\mathrm{corr,i}}_{\mathrm{he/xe}}$ of Eq. (4.11) takes values near $\pm 2\pi$. The phase unwrapping is accomplished with the help of an if statement: if $|\Delta\Phi^{\mathrm{corr,i}}_{\mathrm{he/xe}}| > \Phi_{\mathrm{test}}$, 2π is subtracted from $\Phi^{\mathrm{i}}_{\mathrm{he/xe}}$; if $|\Delta\Phi^{\mathrm{corr,i}}_{\mathrm{he/xe}}| < \Phi_{\mathrm{test}}$, 2π is added to $\Phi^{\mathrm{i}}_{\mathrm{he/xe}}$. If no phase wrap appears, the magnitude of $\Delta\Phi^{\mathrm{corr,i}}_{\mathrm{he/xe}}$ is smaller than 0.2 rad, so Φ_{test} can have any value between 0.2 and 2π.

It is important to note that the errors of $\Phi^{\mathrm{i-1}}_{\mathrm{he/xe}}$ and $\bar{\omega}_{\mathrm{he/xe}}$ do not influence the error of $\Phi^{\mathrm{i}}_{\mathrm{he/xe}}$, because the mod(...) term is subtracted in Eq. (4.12). In this way, $\Phi^{\mathrm{he/xe}}_{\mathrm{est,i}}$ is used solely to determine the number of traversed periods. Hence, the error of $\Phi^{\mathrm{i}}_{\mathrm{he/xe}}$ only depends on the values $A^{\mathrm{i}}_{\mathrm{he/xe}}$ and $B^{\mathrm{i}}_{\mathrm{he/xe}}$ and their errors, $\delta A^{\mathrm{i}}_{\mathrm{he/xe}}$ and $\delta B^{\mathrm{i}}_{\mathrm{he/xe}}$, which are determined by the χ^2-fit. It has been verified that these two parameters are not much correlated (the correlated and uncorrelated errors differ by less than 10%), so one can use the Gaussian error propagation law to determine the error $\delta\Phi^{\mathrm{i}}_{\mathrm{he/xe}}$:

$$\delta\Phi^{\mathrm{i}}_{\mathrm{he/xe}} = \frac{1}{\left(A^{\mathrm{i}}_{\mathrm{he/xe}}\right)^2 + \left(B^{\mathrm{i}}_{\mathrm{he/xe}}\right)^2} \sqrt{\left(B^{\mathrm{i}}_{\mathrm{he/xe}}\right)^2 \cdot \left(\delta A^{\mathrm{i}}_{\mathrm{he/xe}}\right)^2 + \left(A^{\mathrm{i}}_{\mathrm{he/xe}}\right)^2 \cdot \left(\delta B^{\mathrm{i}}_{\mathrm{he/xe}}\right)^2}\,, \tag{4.13}$$

where the derivative of the arctangent function, $\frac{d}{dx}\arctan(x) = \frac{1}{1+x^2}$, was used.

4.3 Weighted phase difference and phase shifts

For each measurement run, the dependence of the phase of Eq. (4.12) on the time t can be expressed as

$$\Phi_{\mathrm{he/xe}}(t = m\tau) = \Phi_{\mathrm{he/xe}}(t = (m-1)\tau) + \bar{\omega}_{\mathrm{he/xe}} \cdot \tau \; + \varphi^{\mathrm{m}}_{\mathrm{he/xe}} \tag{4.14}$$

$$- \mathrm{mod}\left(\frac{\Phi_{\mathrm{he/xe}}(t = (m-1)\tau) + \bar{\omega}_{\mathrm{he/xe}} \cdot \tau}{2\pi}\right) \; , \tag{4.15}$$

where the phase offset of the first time interval is $\Phi_{\mathrm{he/xe}}(t = 0) = \varphi^{1}_{\mathrm{he/xe}}$ (Eq. (4.8)) and $\bar{\omega}_{\mathrm{he/xe}}$ is the average frequency of the corresponding run according to Eq. (4.10). To make small phase variations visible, the dominant contribution to the phase, the linear term $m \cdot \bar{\omega}_{\mathrm{he/xe}} \cdot \tau = \bar{\omega}_{\mathrm{he/xe}} \cdot t$, is at first subtracted. The residual phases for ^{3}He and ^{129}Xe after the subtraction of the main linear term are shown in Fig. 4.13, exemplary for run (2) (C94). For better comparison the phase offset $\Phi_{\mathrm{he/xe}}(t = 0)$ is subtracted as well (here $t = 0$ is the starting point of run (2)), and the ^{129}Xe phase is already multiplied with the ratio $\frac{\gamma_{\mathrm{he}}}{\gamma_{\mathrm{xe}}}$, i.e.,

$$\begin{aligned} \Phi'_{\mathrm{he}}(t) &= \Phi_{\mathrm{he}}(t) - \Phi_{\mathrm{he}}(t = 0) - \bar{\omega}_{\mathrm{he}} \cdot t \; , \\ \frac{\gamma_{\mathrm{he}}}{\gamma_{\mathrm{xe}}} \Phi'_{\mathrm{xe}}(t) &= \frac{\gamma_{\mathrm{he}}}{\gamma_{\mathrm{xe}}} \left(\Phi_{\mathrm{xe}}(t) - \Phi_{\mathrm{xe}}(t = 0) - \bar{\omega}_{\mathrm{xe}} \cdot t\right) \; . \end{aligned} \tag{4.16}$$

The variations in the phases arise from drifts of the magnetic holding field during the measurement.

The relevant quantity to consider further is the weighted phase difference $\Delta\Phi(t)$ according to Eq. (4.2), which is shown in Fig. 4.14 for run (1) (upper curve). The plot shows that there exist contributions to the phase difference that are not eliminated. The dominant term in $\Delta\Phi(t)$ has a linear time dependence, and can be explained by the Earth's rotation, i.e., the rotation of the SQUID detector with respect to the precessing spins. This term can be calculated theoretically (see Sec. 4.3.1), and subtracted from $\Delta\Phi(t)$ to get the remaining phase difference $\Delta\Phi_{\mathrm{rem}}(t)$ (lower curve in Fig. 4.14).

Furthermore, there are exponential terms that can be attributed to demagnetization fields that are produced by the precessing ^{3}He and ^{129}Xe nuclear spins themselves inside a non-spherical cell (Sec. 4.3.3). Other phase shifts arise from deviations of the ratio $\frac{\gamma_{\mathrm{he}}}{\gamma_{\mathrm{xe}}}$ from the literature value due to chemical shifts (Sec. 4.3.2), and from magnetic field gradients (Sec. 4.3.4). Some smaller possible contributions will be discussed in Sec. 4.3.5.

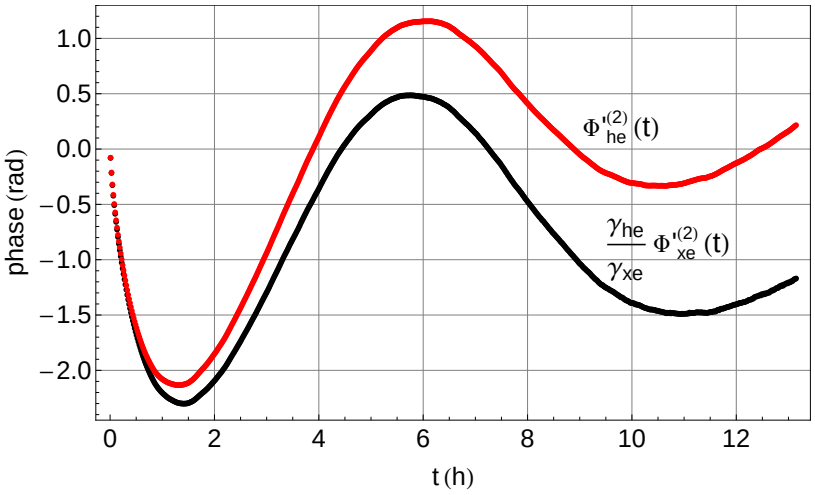

Figure 4.13: Extracted Helium and Xenon phases for run (2) (C94), after subtraction of the linear term $\bar{\omega}^{(2)}_{\mathrm{he/xe}} \cdot t$ and the phase offset $\Phi^{(2)}_{\mathrm{he/xe}}(t = 0)$ (see Eq. (4.16)). For better comparison, the ^{129}Xe phase is scaled with $\frac{\gamma_{\mathrm{he}}}{\gamma_{\mathrm{xe}}}$. The time t starts with the beginning of run (2), and one data point comprises 20 sub-data sets.

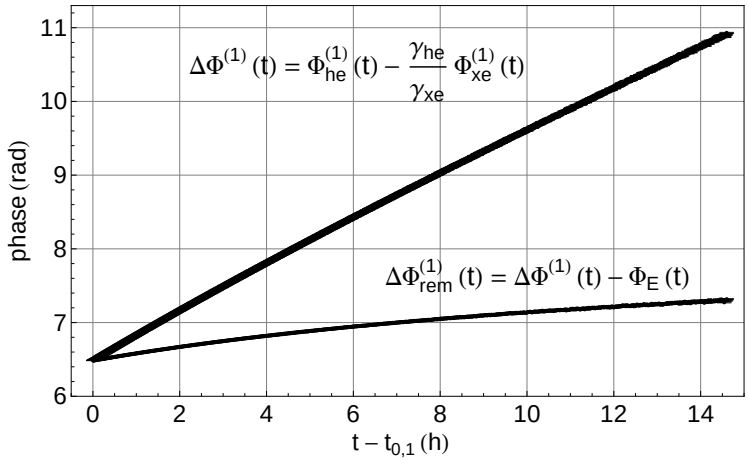

Figure 4.14: Weighted phase difference for run (1) before ($\Delta\Phi^{(1)}$) and after ($\Delta\Phi^{(1)}_{\mathrm{rem}}$) the subtraction of the Earth's rotation term Φ_{E} (Eq. (4.21)). One data point comprises 20 sub-data sets.

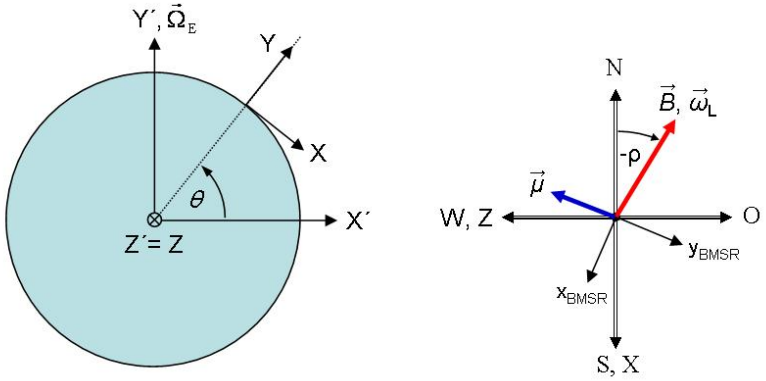

Figure 4.15: *Left*: The Earth's rotating coordinate system (X´,Y´,Z´) is shown, where the Y´-axis is parallel to the Earth's rotation axis, Ω_E. The laboratory system (X,Y,Z) is located at the BMSR-2 in Berlin with Θ being the northern latitude. The Z and Z´-axis are parallel. *Right*: In the laboratory system, the X-axis points to the southern and the Z-axis to the western direction. The holding field $\vec{B}$ inside BMSR-2 points to the north-eastern direction, and the angle between field and north direction is $\rho = 28°$. The field direction is identical with the -x-direction in the BMSR-2 coordinate system.

4.3.1 Contribution of the Earth's rotation

The dominant contribution to the time dependence of $\Delta\Phi(t)$ can be explained by the rotation of the SQUID detector (ω_{det}) with respect to the precessing spins ($\omega_{\mathrm{L,he/xe}}$) due the Earth's rotation with $\Omega_E = 7.2921150(1)\cdot 10^{-5}$ rad/s [10]. In the laboratory system a reduced Larmor precession frequency is measured, $\omega_{\mathrm{he/xe}} = \omega_{\mathrm{L,he/xe}} - \omega_{\mathrm{det}}$, since the ^{3}He/^{129}Xe magnetic moments as well as the SQUID detector are rotating in the same sense with respect to the magnetic guiding field. The field was oriented in the (-x)-direction in the BMSR-2 coordinate system, which is the north-eastern direction, and the angle between field and north direction was $\rho = 28°$ (see Fig. 4.15). The sense of rotation of the precessing magnetic moments can be deduced from the Bloch equations (2.10). As the nuclear magnetic moment is negative for both ^{3}He and ^{129}Xe, the sense of rotation is right-handed with respect to the magnetic field direction (see Fig. 4.16, right side). This can also be verified by looking at the precession signals seen by different SQUID sensors. In Fig. 4.16 the ^{3}He/^{129}Xe precession signal of measurement C92 is shown, detected with the SQUID sensors Z3K, Z1E and Z1B that are placed at different positions along the y-axis. One can see that the maximum amplitude is first detected at Z3K, then at Z1E and then at Z1B, which shows that the sense of rotation of the precessing moments is right-handed with respect to the field direction and to the Earth's rotation axis, i.e., magnetic moments and the Earth rotate in the same sense.
To calculate the size of the frequency shift caused by the rotating detector, ω_{det}, a coordi-

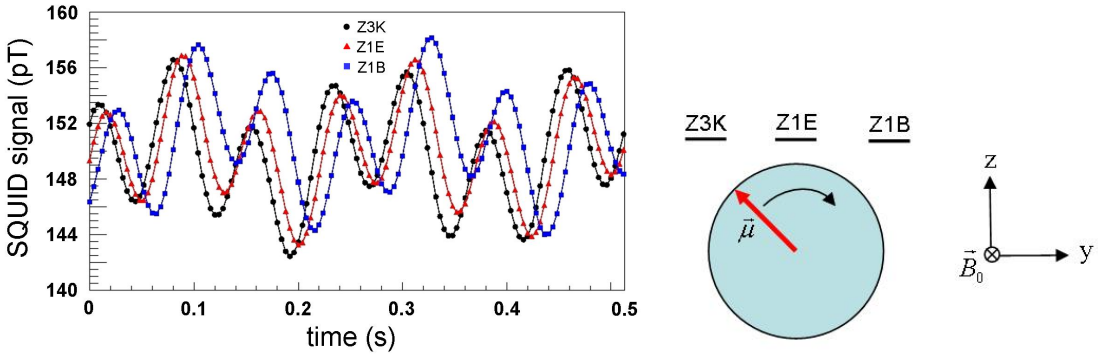

Figure 4.16: *Left*: Precession signal of run C92 detected with 3 different SQUID sensors: Z3K (black dots), Z1E (red triangles) and Z1B (blue squares). For better visualization, the offsets are shifted and the amplitudes scaled. *Right*: Position of the respective SQUIDs and sense of rotation of the precessing magnetic moments.

nate transformation from the laboratory system (X,Y,Z) to the Earth system (X',Y',Z') is performed (see Fig. 4.15). In the laboratory system, the unit vector in field direction, i.e, the axis of precession $\hat{\omega}_{\mathrm{L}}$, is given by (see Fig. 4.15, right side)

$$\hat{\omega}_{\mathrm{L}} = \frac{\vec{\omega}_{\mathrm{L}}}{\omega_{\mathrm{L}}} = \begin{pmatrix} -\cos(-\rho) \\ 0 \\ -\sin(-\rho) \end{pmatrix} = \begin{pmatrix} -\cos\rho \\ 0 \\ \sin\rho \end{pmatrix} , \tag{4.17}$$

where $\rho = 28°$ is the angle between field and north direction. Knowing the northern latitude $\Theta = 52.5164°$, where the PTB Berlin is located [79], $\hat{\omega}_{\mathrm{L}}$ can be transformed into the rotating system (X',Y',Z'):

$$\hat{\omega}'_{\mathrm{L}} = \begin{pmatrix} \sin\Theta & \cos\Theta & 0 \\ -\cos\Theta & \sin\Theta & 0 \\ 0 & 0 & 1 \end{pmatrix} \cdot \begin{pmatrix} -\cos\rho \\ 0 \\ \sin\rho \end{pmatrix} = \begin{pmatrix} -\sin\Theta\cos\rho \\ \cos\Theta\cos\rho \\ \sin\rho \end{pmatrix} . \tag{4.18}$$

The angle χ between the Earth's rotation axis, $\hat{\Omega}_{\mathrm{E}}$, and the axis of precession, $\hat{\omega}'_{\mathrm{L}}$, can be calculated via the scalar product:

$$\cos\chi = \hat{\Omega}_{\mathrm{E}} \cdot \hat{\omega}'_{\mathrm{L}} = \begin{pmatrix} 0 \\ 1 \\ 0 \end{pmatrix} \cdot \begin{pmatrix} -\sin\Theta\cos\rho \\ \cos\Theta\cos\rho \\ \sin\rho \end{pmatrix} = \cos\Theta\cos\rho \, . \tag{4.19}$$

We get $\chi = 57.33°$. Finally, the size of the shift in the ^{3}He and ^{129}Xe Larmor frequencies

caused by the rotating detector, ω_{det}, can be given:

$$\omega_{\mathrm{det}} = |\Omega_{\mathrm{E}}| \cos\Theta \cos\rho \ . \tag{4.20}$$

In the weighted phase difference this leads to the following linear term

$$\begin{aligned} \Phi_{\mathrm{E}} = \Delta\omega_{\mathrm{E}} \cdot t &= -(1 - \frac{\gamma_{\mathrm{he}}}{\gamma_{\mathrm{xe}}})\ \omega_{\mathrm{det}} \cdot t \\ &= 6.87263 \cdot 10^{-5}\ \frac{\mathrm{rad}}{\mathrm{s}} \cdot \mathrm{t} \ . \end{aligned} \tag{4.21}$$

The contribution of the Earth's rotation can be subtracted from the weighted phase difference $\Delta\Phi$. The remaining temporal change of $\Delta\Phi$ after the subtraction of Eq. (4.21), $\Delta\Phi_{\mathrm{rem}}(t)$, is shown in Fig. 4.14 for run (1). It still contains small linear terms plus the exponential terms that will be discussed in Sec. 4.3.3. Part of the remaining linear term is due to the uncertainty in the determination of the angle ρ between the magnetic guiding field and the north direction which is assumed to be below 1°. Ω_{E} and Θ, in contrast, are known precisely enough, so their error can be neglected. The uncertainty $\delta\rho = 1°$ corresponds to a maximum frequency uncertainty of $\delta(\Delta\omega_{\mathrm{E}}) = 6.3 \cdot 10^{-7}$ rad/s and therewith a linear term in the remaining weighted phase difference $\Delta\Phi_{\mathrm{rem}}$ of

$$|\Phi_{\delta\mathrm{E}}| \leq 6.3 \cdot 10^{-7}\ \frac{\mathrm{rad}}{\mathrm{s}} \cdot \mathrm{t} \ . \tag{4.22}$$

4.3.2 Gyromagnetic ratios and Chemical shift

The literature values we took as the gyromagnetic ratios of ^{3}He and ^{129}Xe are valid for the shielded nucleus in a gaseous state at vanishing particle density. Here "shielded" means that the whole atom is considered, with the electron sheet that serves as a shield for the nucleus against outer magnetic fields (diamagnetic shielding). For the ^{3}He gyromagnetic ratio we used the CODATA value given in [57], $\gamma_{\mathrm{he}} = 2.037894730(56) \cdot 10^8\ \frac{\mathrm{rad}}{\mathrm{Ts}}$. In [60] the magnetic moment of ^{129}Xe is given, that is calculated using a value for the proton magnetic moment μ_{p} from the year 1987. With the latest CODATA value for μ_{p} [57], we recalculated the magnetic moment of ^{129}Xe and therewith the gyromagnetic ratio to be $\gamma_{\mathrm{xe}} = 7.39954378(50) \cdot 10^7\ \frac{\mathrm{rad}}{\mathrm{Ts}}$. The ratio of the gyromagnetic ratios $\frac{\gamma_{\mathrm{he}}}{\gamma_{\mathrm{xe}}}$ used in the weighted phase difference (4.2) then becomes

$$\frac{\gamma_{\mathrm{he}}}{\gamma_{\mathrm{xe}}} = 2.75408159(20) \ . \tag{4.23}$$

In our experiment, deviations of the gyromagnetic ratios from the literature value arise from interactions of the noble gas atoms with each other [69] and with the N_2 buffer gas

	$\Delta\omega_{\mathrm{Xe-Xe}}$ (10^{-7} rad/s)	$\Delta\omega_{\mathrm{Xe-N2}}$ (10^{-7} rad/s)	p_{Xe} (mbar)	p_{N2} (mbar)
C92	1.28	1.67	8.3	29.3
C94	1.35	2.01	8.8	35.2
C95	1.35	1.87	8.8	32.8
C99	1.43	1.90	9.3	33.4
C101	1.48	1.95	9.6	34.2
C102	1.28	1.58	8.3	27.8
C103	1.28	1.48	8.3	26.0

Table 4.4: Chemical shifts of xenon in xenon and xenon in nitrogen for measurements C92-C103 according to Eq. (4.24) and (4.25).

[38]. The reason for these so-called *chemical shifts* (CS) lies in the fact that due to collisions with other atoms the electron sheet of the ^{129}Xe/^{3}He atoms gets deformed. This changes the diamagnetic shielding against the external field B_0, so that the nucleus experiences a slightly different field, which leads to a shift in the Larmor frequency, $\Delta\omega_{\mathrm{L,CS}}$. As the ^{3}He nucleus has only 2 surrounding electrons, the chemical shift is very small for helium. In [33] the pressure dependence of the ^{3}He chemical shift at standard temperature ($T_0 = 273.15$ K) is given to be about $0.1 \cdot 10^{-9} \frac{p}{p_0}$, where $p_0 = 1013.25$ mbar is the standard atmospheric pressure. This is more than three orders of magnitude smaller than the ^{129}Xe chemical shift (see below), so it can be neglected.

As the pressure p and the temperature T can be seen as constant in the course of the measurement, and also the magnetic guiding field (except for small changes in the order of less than 10^{-5}), the chemical frequency shift is constant to leading order, which leads to a linear term in the ^{129}Xe phase. The shift that results from collisions of ^{129}Xe atoms with each other is given by [69]:

$$\Phi_{\mathrm{CS,Xe-Xe}} = \Delta\omega_{\mathrm{CS,Xe-Xe}} \cdot t = \omega_{\mathrm{L,Xe}} \cdot t \cdot 5.66 \cdot 10^{-7} \frac{p}{p_0} \cdot \frac{T_0}{T} \ , \tag{4.24}$$

while the chemical shift of ^{129}Xe due to N_2 can be estimated from Ref. [38]:

$$\Phi_{\mathrm{CS,Xe-N2}} = \Delta\omega_{\mathrm{CS,Xe-N2}} \cdot t = \omega_{\mathrm{L,Xe}} \cdot t \cdot 2.1 \cdot 10^{-7} \frac{p}{p_0} \cdot \frac{T_0}{T} \ . \tag{4.25}$$

For the measurements C92 to C103 the shifts for the xenon Larmor frequency are listed in Tab. 4.4. They are all in the order of 10^{-7} rad/s. The fluctuations of up to $\pm 26\%$ from one

run to another are caused by the different pressures used.

Another term may arise due to the adsorption of ^{129}Xe atoms at the walls of the glass bulb [63]. As the average sticking time of ^{129}Xe at the cell walls is not known, it is not possible to give an estimation for this additional term. If we assume that it is in the same order as the shifts described above, i.e., between $1 \cdot 10^{-7}$ and $2 \cdot 10^{-7}$ rad/s, we get a total shift in the ^{129}Xe frequency in the range $4 \cdot 10^{-7}$ rad/s $< |\Delta\omega_{\mathrm{CS,Xe}}| < 6 \cdot 10^{-7}$ rad/s. Thus the chemical shift contributes to the linear term in the phase difference with

$$\Delta\Phi_{\mathrm{CS}} \approx \left| -\frac{\gamma_{\mathrm{he}}}{\gamma_{\mathrm{xe}}} \Phi_{\mathrm{CS,Xe}} \right| \leq 1.65 \cdot 10^{-6} \ \frac{\mathrm{rad}}{\mathrm{s}} \cdot \mathrm{t} \ . \tag{4.26}$$

4.3.3 Ramsey-Bloch-Siegert (RBS) shift due to demagnetization fields

As mentioned in Chap. 2.4, the magnetic field produced by the magnetic moments of polarized gases inside a non-spherical cell is not equal to zero anymore due to demagnetization effects. The components of the demagnetization field that are rotating in the plane perpendicular to B_0 can produce a shift in the spin precession frequency, the Ramsey-Bloch-Siegert (RBS) shift (see Eq. (2.23)). Let the magnetic guiding field B_0 be oriented in x-direction. The demagnetization field $\vec{B}_{\mathrm{demag}}(\vec{r}, t)$ that is produced by the magnetic moments in the appendix volume is rotating with the Larmor frequency $\omega_{\mathrm{r}} = \omega_{\mathrm{L,demag}}$ around the outer field $\vec{B}_0$, and its strength is decreasing exponentially with the T_2^* time. According to Eq. (2.23), the component of the demagnetization field that is rotating perpendicular to $\vec{B}_0$,

$$\begin{aligned} \vec{B}_{\mathrm{yz}}(\vec{r}, t) &= B_{\mathrm{yz}}(\vec{r}, t) \left(\hat{e}_{\mathrm{x}} \cos(\omega_{\mathrm{r}} t) + \hat{e}_{\mathrm{y}} \sin(\omega_{\mathrm{r}} t)\right) \\ &= B_{\mathrm{yz}}(\vec{r}, t_0) \cdot \exp\left(-\frac{t}{T_2^*}\right) \cdot \left(\hat{e}_{\mathrm{x}} \cos(\omega_{\mathrm{r}} t) + \hat{e}_{\mathrm{y}} \sin(\omega_{\mathrm{r}} t)\right) \ , \end{aligned} \tag{4.27}$$

leads to a RBS-shift of the Larmor frequency of the noble gas atoms in the spherical part of the cell. It is difficult to estimate the size of the demagnetization field, but as the appendix volume of the measurement cell (Z146) is roughly a factor 450 smaller than the total cell volume, it is assumed that the demagnetization field is about 450 times smaller than the main dipole field produced by the noble gas atoms. The dipole field for ^{3}He according to Eq. (2.26) at a distance of $r = 3$ cm (which is roughly the distance between the center of the cell and the appendix) for typical values of $P = 0.1$ and $p = 4.1$ mbar is $B_{\mathrm{He}} \approx 81.6$ pT. So the ^{3}He demagnetization field at the distance $r = 3$ cm, i.e., in the middle of the cell, can be estimated to be $B_{\mathrm{demag}}^{\mathrm{He}} \approx (81.6/450)$ pT ≈ 0.2 pT.

To get the mean RBS frequency shift, one has to integrate over the cell volume, i.e., with Eq. (2.23) and $\omega_{\mathrm{demag}}(\vec{r},t) = \gamma B_{\mathrm{yz}}(\vec{r},t)$ we get

$$\langle \Delta\omega_{\mathrm{RBS}}(\vec{r},t)\rangle = \begin{cases} +\int_{cell} dV' \left(\sqrt{(\Delta\omega_{\mathrm{L}}(\vec{r}'))^2 + (\omega_{\mathrm{demag}}(\vec{r}',t))^2} - \Delta\omega_{\mathrm{L}}(\vec{r}') \right) & \text{for } \Delta\omega_{\mathrm{L}} < 0, \\ -\int_{cell} dV' \left(\sqrt{(\Delta\omega_{\mathrm{L}}(\vec{r}'))^2 + (\omega_{\mathrm{demag}}(\vec{r}',t))^2} - \Delta\omega_{\mathrm{L}}(\vec{r}') \right) & \text{for } \Delta\omega_{\mathrm{L}} > 0. \end{cases} \tag{4.28}$$

Here $\Delta\omega_{\mathrm{L}}(\vec{r}')$ is the difference between the Larmor frequencies of the magnetic moments in the spherical part of the cell, $\omega_{\mathrm{L,sph}}(\vec{r}')$, and the rotation frequency of the demagnetization field ω_{r} (which is assumed to be constant), i.e.,

$$\Delta\omega_{\mathrm{L}}(\vec{r}') = \omega_{\mathrm{L,sph}}(\vec{r}') - \omega_{\mathrm{r}} \ . \tag{4.29}$$

As the Larmor frequency $\omega_{\mathrm{L,sph}}$ is proportional to the local magnetic field, $\Delta\omega_{\mathrm{RBS}}$ depends on the actual magnetic field gradients across the cell. Furthermore, motional narrowing effects due to particle diffusion should play a role. Because of the complexity of this problem it was not possible to give an estimation for the size of $\Delta\omega_{\mathrm{RBS}}$ within the scope of this work. Anyhow, with the help of the following considerations, one can draw conclusions about the qualitative developing of the frequency (and phase) shift and therewith the developing of the weighted phase difference.

Depending on the sizes of $\Delta\omega_{\mathrm{L}}$ and ω_{demag}, one can use different approximations for $\Delta\omega_{\mathrm{RBS}}$ (in the following, without loss of generality, we will assume that $\Delta\omega_{\mathrm{L}}$ is negative, so that we consider only the first part of Eq. (2.23).):

1. $$\begin{aligned} \Delta\omega_{\mathrm{RBS}} &= \omega_{\mathrm{demag}} \sqrt{1 + \left(\frac{\Delta\omega_{\mathrm{L}}}{\omega_{\mathrm{demag}}}\right)^2} - \Delta\omega_{\mathrm{L}} \\ &\approx \omega_{\mathrm{demag}} \left(1 + \frac{1}{2}\left(\frac{\Delta\omega_{\mathrm{L}}}{\omega_{\mathrm{demag}}}\right)^2 - \ ...\right) - \Delta\omega_{\mathrm{L}} \qquad \text{for } \Delta\omega_{\mathrm{L}} < \omega_{\mathrm{demag}}, \end{aligned} \tag{4.30}$$

2. $$\begin{aligned} \Delta\omega_{\mathrm{RBS}} &= \Delta\omega_{\mathrm{L}} \sqrt{1 + \left(\frac{\omega_{\mathrm{demag}}}{\Delta\omega_{\mathrm{L}}}\right)^2} - \Delta\omega_{\mathrm{L}} \\ &\approx \frac{1}{2}\left(\frac{\omega_{\mathrm{demag}}}{\Delta\omega_{\mathrm{L}}}\right)^2 - \ ... \qquad \text{for } \Delta\omega_{\mathrm{L}} > \omega_{\mathrm{demag}}. \end{aligned} \tag{4.31}$$

For the first case, the dominant term in $\Delta\omega_{\mathrm{RBS}}$ is linear in ω_{demag}, which is proportional to $\exp(-t/T_2^*)$, because B_{demag} decreases exponentially with T_2^*. For the second case, $\Delta\omega_{\mathrm{RBS}}$ shows a behavior proportional to $\exp(-2t/T_2^*)$.

Now it has to be distinguished between the frequency shift that one species evokes on the other (the RBS cross-shift $\Delta\omega_{\mathrm{RBS,c}}^{\mathrm{He(Xe)}}$), and the one that each species evokes on itself (the RBS self-shift $\Delta\omega_{\mathrm{RBS,s}}^{\mathrm{He(Xe)}}$). For the cross-shift, $|\Delta\omega_{\mathrm{L,c}}^{\mathrm{He(Xe)}}| = |\omega_{\mathrm{L,sph}}^{\mathrm{He(Xe)}} - \omega_{\mathrm{r}}^{\mathrm{Xe(He)}}| \approx (13.4 - 4.9)$ Hz $=$ 8.5 Hz is much greater than $\omega_{\mathrm{demag}}^{\mathrm{He(Xe)}}$, so the second formula is valid. With the estimated size of ≈ 0.2 pT for the ^{3}He demagnetization field we get $\omega_{\mathrm{demag}}^{\mathrm{He}} = \gamma B_{\mathrm{demag}}^{\mathrm{He}} \approx 3.7 \cdot 10^{-5}$ Hz, which would lead to a cross-shift for ^{129}Xe of $\Delta\omega_{\mathrm{RBS,c}}^{\mathrm{Xe}} = \frac{1}{2}\omega_{\mathrm{demag}}^{\mathrm{He}}/|\Delta\omega_{\mathrm{L,c}}^{\mathrm{Xe}}| \approx 9 \cdot 10^{-12}\ \frac{\mathrm{rad}}{\mathrm{s}}$. The cross-shift for ^{3}He is of similar size. Hence, the RBS cross-shift is many orders of magnitude smaller than the chemical shift of Eq. (4.26) and thus can be neglected.

For the self-shift, $\Delta\omega_{\mathrm{L,s}}^{\mathrm{He(Xe)}}(\vec{r}) = \omega_{\mathrm{L,sph}}^{\mathrm{He(Xe)}}(\vec{r}) - \omega_{\mathrm{r}}^{\mathrm{He(Xe)}}$ is much smaller and is strongly depending on $\vec{r}$. As the sizes of $\Delta\omega_{\mathrm{L,s}}^{\mathrm{He(Xe)}}$ and the demagnetization fields can not be predicted, we do not know a priori which of the two cases (Eq. (4.30) or (4.31)) is the dominating one for the self-shift. When looking at the weighted phase difference data, for example of run (1) in Fig. 4.14, one can conclude from the time constant of the exponential developing that the first case with $\Delta\omega_{\mathrm{L,s}}^{\mathrm{He(Xe)}}(\vec{r}) < \omega_{\mathrm{demag}}^{\mathrm{He(Xe)}}$ is more likely, i.e., that the RBS frequency shift, and thus the phase shift, is proportional to $\exp(-t/T_2^*)$. To prove this, we fitted the following model to the phase difference data:

$$f(t) = \Phi_0 + \Delta\omega_{\mathrm{lin}} t + E_{\mathrm{he}} \exp\left(\frac{-t}{\tau_{\mathrm{he}}}\right) + E_{\mathrm{xe}} \exp\left(\frac{-t}{\tau_{\mathrm{xe}}}\right) \ , \tag{4.32}$$

and compared the χ^2 and the residuals for $\tau_{\mathrm{he(xe)}} = T_{2,\mathrm{he(xe)}}$ and $\tau_{\mathrm{he(xe)}} = T_{2,\mathrm{he(xe)}}/2$. The fits with $\tau_{\mathrm{he(xe)}} = T_{2,\mathrm{he(xe)}}$ led to better results, thus we assume that $\Delta\omega_{\mathrm{L,s}}^{\mathrm{He(Xe)}}(\vec{r}) < \omega_{\mathrm{demag}}^{\mathrm{He(Xe)}}$ is fulfilled for the majority of the magnetic moments in the cell volume. Hence, for our model we assume that $\Delta\omega_{\mathrm{RBS}} \propto \exp(-t/T_2^*)$.

The strength of the RBS-shift mainly depends on the deviation of the cell's geometry from sphericity, as well as on the orientation of the cell with respect to the magnetic guiding field. The latter can be seen in Fig. 4.17, where the change of the remaining phase signal, after subtraction of the Earth's rotation effect, due to a 90° rotation of the cell is shown. The dominating exponential terms almost disappear for the case that the appendix is oriented almost perpendicular to $\vec{B}_0$. The glass cell used here had a larger bulge towards its appendix than the one used in the runs C92-C103, where we have already regarded the sphericity of our glass bulb to be an important factor to minimize demagnetization induced effects.

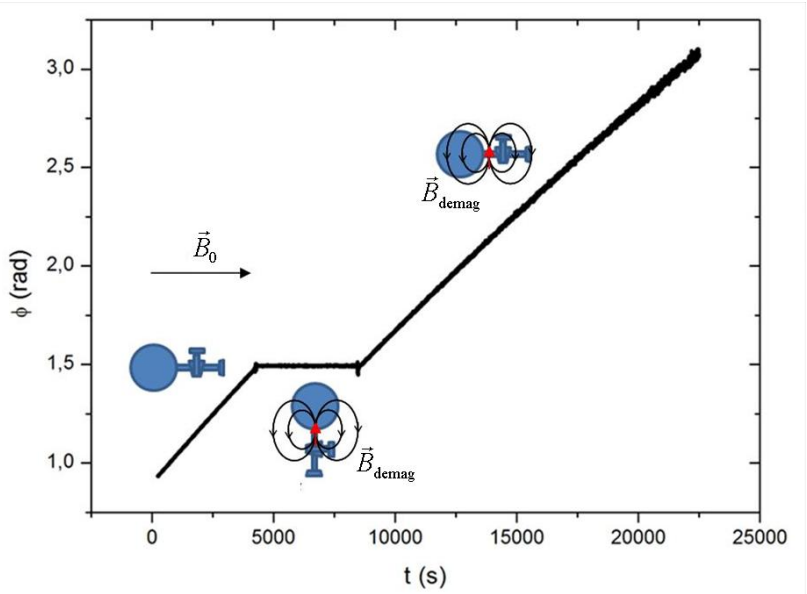

Figure 4.17: Position dependence of the remaining phase signal due to demagnetization fields for a non-ideal spherical cell oriented either parallel or perpendicular to the magnetic guiding field $\vec{B}_0$.

4.3.4 Field gradient induced shifts

In Ref. [17] Cates et al. derive shifts in the spin precession frequency due to static and oscillating magnetic field gradients for a spin polarized gas in a spherical volume of radius R. For a magnetic guiding field that is the sum of a static mean field $\vec{B}_0$ (which is oriented in x-direction), a static inhomogeneous field $\vec{B}_1(\vec{r})$ and an oscillating magnetic field $\vec{B}_2 = \vec{B}_2'(\vec{r})\cos(\omega t) + \vec{B}_2''(\vec{r})\sin(\omega t)$, i.e.,

$$\vec{B}(\vec{r},t) = \vec{B}_0 + \vec{B}_1(\vec{r}) + \vec{B}_2'(\vec{r})\cos(\omega t) + \vec{B}_2''(\vec{r})\sin(\omega t),$$

the frequency shift is given by

$$\begin{aligned}\Delta\omega_{\text{grad}} &= \omega_{\text{grad,stat}} + \omega_{\text{grad,osc}} \\ &= R^2\,\gamma B_0 \sum_n \frac{\gamma^2(|\vec{\nabla}B_{1,\text{y}}|^2 + |\vec{\nabla}B_{1,\text{z}}|^2)}{x_{1\text{n}}^2(x_{1\text{n}}^2-2)(D^2\,x_{1\text{n}}^4\,R^{-4}+\gamma^2 B_0^2)} \\ &\quad + \sum_n \frac{R^2\,\gamma^2}{x_{1\text{n}}^2(x_{1\text{n}}^2-2)}\left(\frac{|\vec{\nabla}B_{2-}|^2(\omega_0-\omega)}{D^2\,x_{1\text{n}}^4\,R^{-4}+(\omega_0-\omega)^2} + \frac{|\vec{\nabla}B_{2+}|^2(\omega_0+\omega)}{D^2\,x_{1\text{n}}^4\,R^{-4}+(\omega_0+\omega)^2}\right).\end{aligned} \tag{4.33}$$

Here γ is the gyromagnetic ratio, D the diffusion constant according to Eq. (2.31), $\omega_0 = \gamma B_0$ the mean Larmor frequency, x_{1n} (n = 1, 2, 3, ...) are the zeros of the derivative

of the spherical Bessel function ($\frac{d}{dx}j_1(x_{1n}) = 0$) and $B_{2\pm} = B_{2\mathrm{x}} \pm iB_{2\mathrm{y}}$.

The first term $\Delta\omega_{\mathrm{grad,stat}}$ of (4.33) describes the frequency shift due to the static, transverse field gradients. To estimate its size, we take the gradient that was estimated in Sec. 4.2.4 to be $G := |\vec{\nabla}B_{1,\mathrm{x}}| = |\vec{\nabla}B_{1,\mathrm{y}}| = |\vec{\nabla}B_{1,\mathrm{z}}| \approx 48.8$ pT/cm. Together with the pressures of measurement C92 (see Tab. 4.1), Eq. (4.33) gives $\Delta\omega^{\mathrm{he}}_{\mathrm{grad,stat}} \approx 2.0 \cdot 10^{-6}$ rad/s and $\Delta\omega^{\mathrm{xe}}_{\mathrm{grad,stat}} = 3.7 \cdot 10^{-7}$ rad/s. If the gradients stay constant during the measurement, this leads to a linear shift in the weighted phase difference of

$$\Delta\Phi_{\mathrm{grad,stat}} = \left(\Delta\omega^{\mathrm{he}}_{\mathrm{grad,stat}} - \frac{\gamma_{\mathrm{he}}}{\gamma_{\mathrm{xe}}}\Delta\omega^{\mathrm{xe}}_{\mathrm{grad,stat}}\right) \cdot t \approx 1 \cdot 10^{-6}\ \frac{\mathrm{rad}}{\mathrm{s}} \cdot \mathrm{t}\ , \tag{4.34}$$

which is in the order of the size of the chemical shift.

The second term $\Delta\omega_{\mathrm{grad,osc}}$ accounts for the gradients of the oscillating field, which can either be the demagnetization field of the own gas species (gradient self-shift), or the one of the other species (gradient cross shift). In Sec. 4.3.3 the size of the demagnetization fields was estimated to be in the order of 1 pT or smaller. Thus the gradients $|\vec{\nabla}B_{2\pm}|$ of the oscillating demagnetization field must be smaller than 1 pT/cm. For the cross-shift, with $(\omega_0 \pm \omega) = (\omega_{\mathrm{He(Xe)}} \pm \omega_{\mathrm{Xe(He)}})$ and with the pressures of measurement C92 (see Tab. 4.1), we get $\Delta\omega^{\mathrm{He}}_{\mathrm{grad,c}} \approx 1 \cdot 10^{-9}$ rad/s and $\Delta\omega^{\mathrm{Xe}}_{\mathrm{grad,c}} \approx -5 \cdot 10^{-11}$ rad/s. Thus the gradient cross-shift can be neglected.

Considering the gradient self-shift, one has to estimate the size of the difference $\Delta\omega$ between the Larmor frequencies of the magnetic moments in the spherical part of the cell, $\omega_{\mathrm{L,sph}}(\vec{r})$, and the frequencies of the magnetic moments in the appendix, i.e., the rotation frequency of the demagnetization field ω_{r}:

$$\Delta\omega = \omega_0 - \omega = \omega_{\mathrm{L,sph}}(\vec{r}) - \omega_{\mathrm{r}}\ . \tag{4.35}$$

As already discussed in the previous section, $\Delta\omega$ depends on the local magnetic field gradients across the cell, and on motional narrowing effects due to particle diffusion. To give a rough estimation, we assume again a mean static gradient of ≈ 50 pT/cm over the cell volume. So the maximum field difference between ^{3}He (^{129}Xe) atoms at a diametrical distance of 6 cm is $\Delta B = 50$ pT/cm $\cdot$ 6 cm $= 300$ pT. With $|\vec{\nabla}B_{2\pm}|$=1 pT/cm and the pressures of C92, the corresponding frequency difference, $\Delta\omega^{\mathrm{He(Xe)}} = \gamma_{\mathrm{He(Xe)}}\Delta B$ leads to a gradient self-shift of $\Delta\omega^{\mathrm{He}}_{\mathrm{grad,s}} < 2 \cdot 10^{-10}$ rad/s and $\Delta\omega^{\mathrm{Xe}}_{\mathrm{grad,s}} < 5 \cdot 10^{-11}$ rad/s. So these shifts can be neglected as well.

4.3.5 Other phase shifts

The following effects that can also shift the phase are quite small compared to the ones discussed in the previous sections, but for the sake of completeness they should be mentioned.

Gravitational shift

Another phase and frequency shift, that I will call the gravitational shift, is resulting from the difference in the molar masses of ^{3}He and ^{129}Xe ($M_{3\mathrm{He}} = 3.016\frac{g}{mol}$ and $M_{129\mathrm{Xe}} = 128.955\frac{\mathrm{g}}{\mathrm{mol}}$) that leads to a shift in the center of masses (the center of mass of ^{129}Xe lies deeper than the one of ^{3}He). Due to this imperfect geometrical overlap, ^{3}He and ^{129}Xe do not exactly see the same magnetic field, and thus the Zeeman term is not canceled out completely:

$$\Delta\omega_{\mathrm{grav}} = \omega_{\mathrm{he}} - \frac{\gamma_{\mathrm{he}}}{\gamma_{\mathrm{xe}}}\omega_{\mathrm{xe}} = \gamma_{\mathrm{he}} \cdot (B_{\mathrm{xe}} + \Delta B) - \gamma_{\mathrm{he}} \cdot B_{\mathrm{xe}} = \gamma_{\mathrm{he}} \cdot \Delta B \ . \tag{4.36}$$

The difference in the center of masses can be calculated using the barometric height formula that gives the pressure at height z for each gas:

$$p(z) = p_0 \exp\left(-\frac{z}{z_0}\right) \quad \text{with} \quad z_0 = \frac{RT}{Mg_0} \ , \tag{4.37}$$

where p_0 is the pressure at the bottom, R the molar gas constant ($R = 8.413\ \frac{\mathrm{J}}{\mathrm{mol\,K}}$), T the temperature, M the molar mass and $g_0 = 9.81\frac{\mathrm{m}}{\mathrm{s}^2}$ the gravitational acceleration. The center of mass then can be calculated by integrating over the z-direction of the cell volume (with radius R):

$$s = \frac{\frac{1}{2R}\int_0^{2R} z\, p(z)\, dz}{\frac{1}{2R}\int_0^{2R} p(z)\, dz}. \tag{4.38}$$

For the (inner) cell radius of $R = 2.9$ cm we then get a difference in center of masses of

$$CM_{\mathrm{he}} - CM_{\mathrm{xe}} \approx 1.5 \cdot 10^{-7}\ \mathrm{m}. \tag{4.39}$$

Taking the maximal measured field gradient in z-direction, $G = \frac{\Delta B}{\Delta z} \approx 47.8\ \frac{\mathrm{pT}}{\mathrm{cm}}$ (see App. C.2), the field difference amounts to $\Delta B \approx 0.7$ fT. Thus, we get an upper estimation for the gravitational phase shift of

$$|\Delta\Phi_{\mathrm{grav}}| = \gamma_{\mathrm{he}} \cdot \Delta B \cdot t = 1.4 \cdot 10^{-7}\ \frac{\mathrm{rad}}{\mathrm{s}} \cdot t \ . \tag{4.40}$$

This is about one order of magnitude smaller than the contribution due to static gradients

and chemical shifts (4.26) and thus can be neglected.

Flip angle $\neq 90°$

If the flip angle is not exactly 90°, which can easily happen if the two coil pairs are not positioned accurately perpendicular to each other, one gets additional static longitudinal field components of the ^{3}He and ^{129}Xe demagnetization fields in a non ideally spherical cell. This leads to a shift of the ^{3}He and ^{129}Xe Larmor frequencies, which should decrease exponentially with the corresponding T_1 times. In the weighted frequency or phase difference, however, this effect should be eliminated, because both the ^{3}He and ^{129}Xe atoms experience these additional fields (if we neglect the small difference in the center of masses discussed above). But problems could arise due to additional gradients that are produced by the longitudinal fields, which could lead to an increased T_2^* relaxation. For this reason the coils pairs should be aligned as accurately as possible.

Interaction between precessing spins and SQUID detectors

As the SQUID sensors are superconducting, dissipation should not happen, i.e., the SQUIDs should not withdraw energy from the precessing spin system. If this would be the case, the decay time of the precession signal would depend on the distance d between the sensor and the measurement cell. Due to the fact that the Dewar was slightly magnetized during the measurements, which also leads to a dependency of the T_2^* time on d, it cannot be completely excluded that an interaction exists between the precessing spins and the SQUID detectors, which would lead to an additional decrease of the decay time T_2^*.

4.3.6 Phase residuals

Now we can make an ansatz for a model to fit the remaining weighted phase difference $\Delta\Phi_{\mathrm{rem}}^{(\mathrm{j})}$ (after subtraction of the Earth's rotation term) for each run ($j = 1, \ldots, 7$). Assuming for now that there is no sidereal variation of the ^{3}He/ ^{129}Xe phases induced by Lorentz-violating couplings, the model contains a linear term with $\Delta\omega_{\mathrm{lin}}^{(\mathrm{j})}$ (due to chemical and field gradient induced shifts), two exponential terms with the amplitudes $E_{\mathrm{he/xe}}^{(\mathrm{j})}$ and the decay times $T_{2,\mathrm{he/xe}}^{*(\mathrm{j})}$ (RBS-shift), plus an offset term $\Phi_0^{(\mathrm{j})}$:

$$\Phi_{\mathrm{fit}}^{(\mathrm{j})}(t) = \Phi_0^{(\mathrm{j})} + \Delta\omega_{\mathrm{lin}}^{(\mathrm{j})}(t - t_{0,\mathrm{j}}) + E_{\mathrm{he}}^{(\mathrm{j})} \cdot \exp\left(\frac{-(t - t_{0,\mathrm{j}})}{T_{2,\mathrm{he}}^{*(j)}}\right) + E_{\mathrm{xe}}^{(\mathrm{j})} \cdot \exp\left(\frac{-(t - t_{0,\mathrm{j}})}{T_{2,\mathrm{xe}}^{*(j)}}\right), \tag{4.41}$$

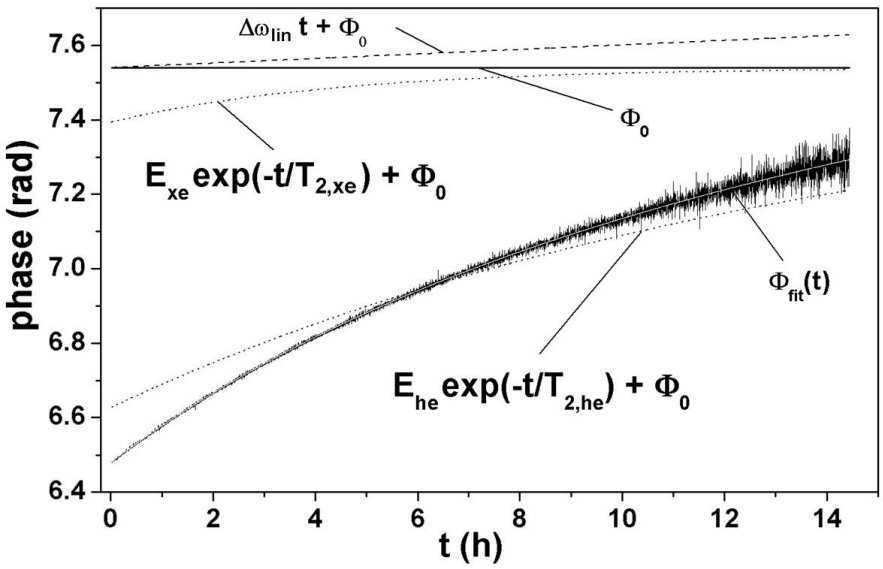

Figure 4.18: Contributions of the different terms to the remaining phase difference $\Delta\Phi^{(1)}_{\mathrm{rem}}$ for run (1).

where $t_{0,\mathrm{j}}$ is the starting time of each run (see Tab. 4.1). The T_2^* times were determined beforehand with a fit on the amplitudes (see Sec. 4.2.4) and are listed in Tab. 4.3. For the fit on the phase difference, $T^*_{2,\mathrm{he/xe}}$ was only varied within the errors determined by the amplitude fit, that were all in the order of $\delta T^*_{2,\mathrm{he/xe}} \approx 1\mathrm{s}$. Hence, the fit model is effectively a linear function in the parameters.

As an example, I will discuss the fit of $\Delta\Phi^{(1)}_{\mathrm{rem}}$, i.e., the remaining phase difference of measurement C92, to the model (4.41). Fig. 4.18 illustrates the sizes of the terms that contribute to the remaining phase difference. One can see that, after the subtraction of the Earth's contribution, the exponential terms are the dominant ones, while the remaining linear term is quite small (in the order of 10^{-6} rad/s). If now the fitted function is subtracted from $\Delta\Phi^{(1)}_{\mathrm{rem}}$, one gets the phase residuals as shown in Fig. 4.19. Due to the exponential decay of the signal amplitudes, mainly that of ^{129}Xe with the shorter $T^*_{2,\mathrm{xe}}$ of only 4.4 h, the signal-to-noise ratio decreases, which means an increase of the residual phase noise, i.e., $\sigma_{\Phi,\mathrm{res}} \propto \exp\left(t/T^*_{2,\mathrm{xe}}\right)$ [27].

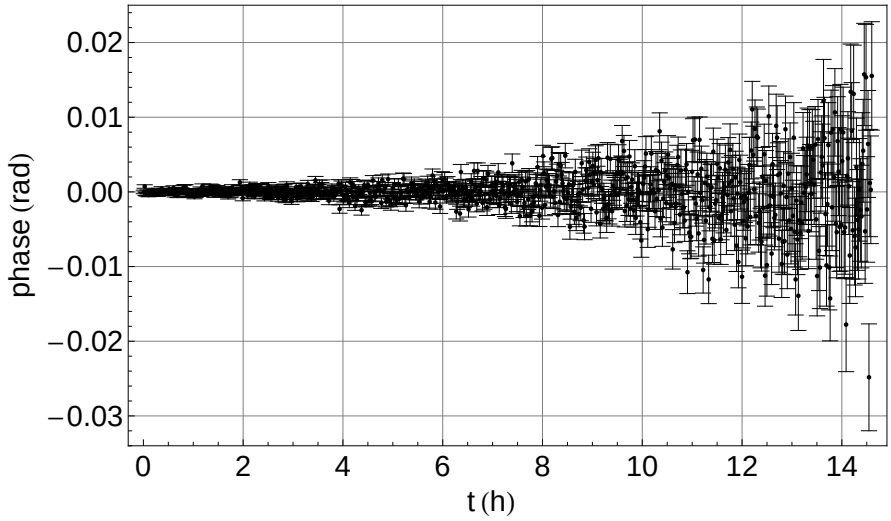

Figure 4.19: Phase residuals of run (1) after subtraction of the fitted function of Eq. (4.41) from $\Delta\Phi^{(1)}_{\mathrm{rem}}$ (one data point comprises 20 sub-data sets, i.e., $\Delta t = 64$ s).

4.4 Limit on Lorentz violation

The possible sidereal modulation due to Lorentz-violating couplings is described by sine/cosine terms with the Earth's rotation frequency Ω_{E} and the Lorentz-violating parameters a_{s} and a_{c} (see Chap. 1.1). So the complete model for the combined fit of the weighted phase difference of all runs ($j = 1, \ldots, 7$) is given by:

$$\begin{aligned} \Phi^{\mathrm{SD}}_{\mathrm{fit}}(t) &= \sum_{\mathrm{j}=1}^{7} \Phi^{'(\mathrm{j})}_{\mathrm{fit}}(t) + a_{\mathrm{s}} \sin\left(\Omega_{\mathrm{E}}(t-t_{0,1}) + \varphi^{1}_{\mathrm{SD}}\right) - a_{\mathrm{c}} \cos\left(\Omega_{\mathrm{E}}(t-t_{0,1}) + \varphi^{1}_{\mathrm{SD}}\right), \\ \text{with } \Phi^{'(\mathrm{j})}_{\mathrm{fit}}(t) &= \begin{cases} \Phi^{(\mathrm{j})}_{\mathrm{fit}}(t) & \text{for } t_{0,\mathrm{j}} \le t \le (t_{0,\mathrm{j}} + N_{\mathrm{j}} \cdot \tau) \\ 0 & \text{elsewhere,} \end{cases} \end{aligned} \tag{4.42}$$

where $\Phi^{(\mathrm{j})}_{\mathrm{fit}}$ is given in Eq. (4.41), $t_{0,\mathrm{j}}$ and N_{j} are the starting times and the number of sub-data sets for run (j), respectively, and $\tau = 3.2$ s is the length of one sub-data set. To be consistent with the coordinate system described in Chap. 1.1 and Ref. [44], the sidereal phase offset $\varphi^{1}_{\mathrm{SD}} = 2\pi \cdot t^{1}_{\mathrm{SD}}$ has to be added, where t^{1}_{SD} is the Local Sidereal Time[5] (in units of day) at the BMSR-2 in Berlin on 2009 March 21 at 20:52 UT, the starting time of run (1).

[5]The Local Sidereal Time has the same value as the right ascension (RA) of an celestial body that is crossing the local meridian (the imaginary circle on the celestial sphere going through the north pole, the zenith, the south pole and the nadir) at that moment (see Fig. 1.5). This means that at the moment when the vernal equinox point crosses the local meridian, the Local Sidereal Time is equal to zero.

Determination of the Local Sidereal Time

t^1_{SD} can be calculated with the help of Ref. [74]. At first the Julian date, i.e., the interval of time in days since January 1, 4713 BC Greenwich noon, is determined for 2009 March 21 20:52 UT to be $JD = 2454912.369444$. This value is now referred to the Julian date on 2000 January 1, 12:00 UT (coordinate system J2000, see Chap. 1.2), which is $JD_0 = 2451545.0$. Out of the difference $D = JD - JD_0 = 3367.369444$ the Greenwich mean sidereal time (GMST') can be calculated as [74]

$$\mathrm{GMST}' = (18.697374558 + 24.06570982441908 \cdot \mathrm{D})\ \mathrm{h} = (3377 \cdot 24 + 8.83327)\ \mathrm{h}\ . \quad (4.43)$$

The multiples of 24 h are neglected, so it rests GMST = 8.83327 h. To get the Berlin local sidereal time LST, the eastern longitude $\alpha = 13.320°$, where the BMSR2 is located, has to be considered:

$$\mathrm{LST} = \mathrm{GMST} + \alpha * 24\ \mathrm{h}/360° = 9.72127\ \mathrm{h}\ . \quad (4.44)$$

Expressed in units of sidereal day, this gives $t^1_{\mathrm{SD}} = 0.40505$.

4.4.1 Fit of single measurements

Before we did a combined fit of all 7 runs with the piecewise defined fit function given in Eq. (4.42), we first fitted every single measurement for its own using the model

$$\Phi^{\mathrm{SD,(j)}}_{\mathrm{fit}}(t) = \Phi^{(\mathrm{j})}_{\mathrm{fit}}(t) + a_{\mathrm{s}} \sin\left(\Omega_{\mathrm{E}}(t - t_{0,\mathrm{j}}) + \varphi^{(\mathrm{j})}_{\mathrm{SD}}\right) - a_{\mathrm{c}} \cos\left(\Omega_{\mathrm{E}}(t - t_{0,\mathrm{j}}) + \varphi^{(\mathrm{j})}_{\mathrm{SD}}\right)\ , \quad (4.45)$$

with (j = 1, ..., 7), $\Phi^{(\mathrm{j})}_{\mathrm{fit}}(t)$ given in Eq. (4.41), the Earth's rotation frequency Ω_{E}, the starting time $t_{0,\mathrm{j}}$ for run (j) (see Tab. 4.1), and the sidereal phase offset $\varphi^{(\mathrm{j})}_{\mathrm{SD}} = 2\pi \cdot t^{(\mathrm{j})}_{\mathrm{SD}}$, with $t^{(\mathrm{j})}_{\mathrm{SD}}$ being the Local Sidereal Time (in units of day) at the beginning of run (j). For these seven χ^2 fits, as well as for the combined fit described in the following section, the *Mathematica* fitting routine as described in Chap. 4.2.1 was used again. The fitting results for the χ^2 fits of runs C92-C103, i.e., the chi-square per degree of freedom, as well as the best-fit parameters with correlated and uncorrelated 1σ-errors, are shown in Tab. 4.5. The χ^2/dof value lies between 1.5 and 2.2, so it is always much greater than 1. Reasons for this could be an underestimation of the ^{3}He and ^{129}Xe phase errors, as well as an incompleteness of the fit model for the phase difference. These reasons are discussed in detail in Sec. 4.4.3. The higher χ^2/dof values were made allowance for by re-scaling the errors to reach a $\chi^2/dof = 1$. This means that the error $\delta a^{\mathrm{corr}}_{\mathrm{c(s)}}$ is the 1σ-error, scaled with the factor $S = \sqrt{\chi^2/dof}$.

Out of the values for a_c and a_s in Tab. 4.5, the corresponding weighted average and uncertainty can be calculated as

$$\bar{a}_{c(s)} \pm \delta\bar{a}_{c(s)} = \frac{\sum_i w_{c(s),i} a^{corr}_{c(s),i}}{\sum_i w_{c(s),i}} \pm \left(\sum_i w_{c(s),i}\right)^{-1/2} , \tag{4.46}$$

where the weight is given by $w_{c(s),i} = 1/\left(\delta a^{corr}_{c(s),i}\right)^2$. This uncertainty is the standard weighted least squares error (1σ-error) as described in the introduction of [2]. The results are

$$\bar{a}_c = (-0.22 \pm 1.12) \text{ mrad } (1\sigma) \text{ and } \bar{a}_s = (-3.41 \pm 1.70) \text{ mrad } (1\sigma). \tag{4.47}$$

Out of Eq. (1.27) one can calculate the Lorentz-violating term in the ^{3}He or ^{129}Xe phase via the time integral of the frequency as

$$\Phi_{LV} = \int_0^t 2\pi\nu_{LV}(t')\,dt' = 2\pi\int_0^t (\nu_X \cos(\Omega_E t') + \nu_Y \sin(\Omega_E t'))\,dt' \tag{4.48}$$

$$= \frac{2\pi}{\Omega_E}(\nu_X \sin(\Omega_E t) - \nu_Y \cos(\Omega_E t)) + \Phi_{0,LV} . \tag{4.49}$$

The Lorentz-violating part in the phase difference $\Delta\Phi = \Phi_{he} - \frac{\gamma_{he}}{\gamma_{xe}}\Phi_{xe}$ then becomes

$$\Delta\Phi_{LV} = (1 - \frac{\gamma_{he}}{\gamma_{xe}})\,\Phi_{LV} = (1 - \frac{\gamma_{he}}{\gamma_{xe}})\,\frac{2\pi}{\Omega_E}(\nu_X \sin(\Omega_E t) - \nu_Y \cos(\Omega_E t)) + \Phi'_{0,LV} . \tag{4.50}$$

If we now compare the coefficients of Eq. (4.50) and the fit model (4.42) and include further Eq. (1.28), we get a relation between the Kostelecký parameter $\tilde{b}^n_{X,Y}$ and the fit parameters $a_{s,c}$:

$$a_{s,c} = \left(1 - \frac{\gamma_{he}}{\gamma_{xe}}\right)\frac{2\pi}{\Omega_E}\,\nu_{X,Y} = \left(1 - \frac{\gamma_{he}}{\gamma_{xe}}\right)\frac{2\pi}{\Omega_E}\frac{2\sin\chi}{h}\,\tilde{b}^n_{X,Y} , \tag{4.51}$$

where χ is the angle between the Earth's rotation axis and the magnetic field axis (see Eq. (4.19)), and h the Planck constant. To give a limit for Lorentz violation, we are interested not only in the single parameters $\bar{a}_c$ and $\bar{a}_s$, but also in the rms magnitude of the sidereal phase variation, $\Phi_{SD} := \sqrt{\bar{a}_c^2 + \bar{a}_s^2}$. Before we can give the uncertainty of Φ_{SD} that corresponds to a confidence level of 95%, we have to know the probability distribution for Φ_{SD} that is formed by multiplying the distributions for a_c and a_s, converting to polar coordinates, and integrating over the polar angle. If a_c and a_s have zero mean value and the same error σ,

	χ^2/dof		Φ_0 (rad)	$\Delta\omega_{\rm lin}$ (μrad/s)	$E_{\rm He}$ (rad)	$E_{\rm Xe}$ (rad)	$a_{\rm s}$ (mrad)	$a_{\rm c}$ (mrad)
C92	1.705	value	0.691	5.76	-0.465	-0.214	-11.87	-2.58
		$\delta_{\rm corr}$	0.204	2.31	0.241	0.033	6.54	1.34
		$\delta_{\rm uncorr}$	3E-5	3E-3	3E-5	4E-5	0.07	0.03
C94	2.021	value	0.831	-2.74	-0.732	-0.088	-4.49	8.65
		$\delta_{\rm corr}$	0.185	2.85	0.262	0.073	12.43	4.18
		$\delta_{\rm uncorr}$	4E-5	4E-3	5E-5	6E-5	0.08	0.05
C95	2.058	value	1.263	-2.80	-1.093	-0.166	5.63	0.18
		$\delta_{\rm corr}$	0.105	1.59	0.148	0.041	5.72	5.49
		$\delta_{\rm uncorr}$	3E-5	4E-3	4E-5	5E-5	0.05	0.05
C99	1.750	value	0.916	-4.75	-0.947	0.030	-0.61	-14.39
		$\delta_{\rm corr}$	0.263	4.33	0.375	0.110	3.39	20.44
		$\delta_{\rm uncorr}$	4E-5	4E-3	5E-5	6E-5	0.05	0.09
C101	2.209	value	1.235	-5.17	-1.155	-0.078	-18.28	13.16
		$\delta_{\rm corr}$	0.095	1.68	0.123	0.028	8.60	5.25
		$\delta_{\rm uncorr}$	3E-5	4E-3	3E-5	4E-5	0.07	0.03
C102	1.864	value	1.637	-3.98	-1.535	-0.104	11.36	3.90
		$\delta_{\rm corr}$	0.099	1.55	0.125	0.024	7.14	3.52
		$\delta_{\rm uncorr}$	3E-5	3E-3	3E-5	4E-5	0.05	0.03
C103	1.495	value	0.687	-0.91	-0.672	-0.009	-5.85	-0.25
		$\delta_{\rm corr}$	0.084	1.20	0.106	0.021	2.46	5.08
		$\delta_{\rm uncorr}$	3E-5	3E-3	3E-5	4E-5	0.03	0.05

Table 4.5: Chi-square per degree of freedom and best-fit parameters with correlated and uncorrelated 1σ-errors for the single fits of runs C92-C103, determined by a χ^2 fit using the model (4.45).

the probability distribution takes the form [8]

$$P(\Phi_{\rm SD}) = \frac{\Phi_{\rm SD}}{\sigma^2} \exp\left(\frac{-\Phi_{\rm SD}^2}{2\sigma^2}\right) \ , \tag{4.52}$$

with the most probable value of $\Phi_{\rm SD}$ occurring at $\Phi_{\rm SD} = \sigma$. In our case, $\bar{a}_{\rm c}$ and $\bar{a}_{\rm s}$ do not have the same error, so as an approximation we take the average of both errors, $\sigma = \frac{\delta\bar{a}_{\rm c}+\delta\bar{a}_{\rm s}}{2}$. Now we can calculate $\Phi_{\rm SD}$ and the corresponding frequency, $\nu_{\rm SD}$, as well as their 95% confidence errors (which are not the 2-σ errors in this case, because the distribution is not normal!) by integrating over the probability distribution. We get

$$\Phi_{\rm SD} := \sqrt{\bar{a}_{\rm c}^2 + \bar{a}_{\rm s}^2} \quad = \quad (3.41 \pm 3.45) \text{ mrad} \quad (95\% \text{ CL}) \tag{4.53}$$

$$\text{and} \quad \nu_{\rm SD} = \Phi_{\rm SD} \cdot \frac{\Omega_{\rm E}}{2\pi} \quad = \quad (39.6 \pm 40.0) \text{ nHz} \quad (95\% \text{ CL}) \ . \tag{4.54}$$

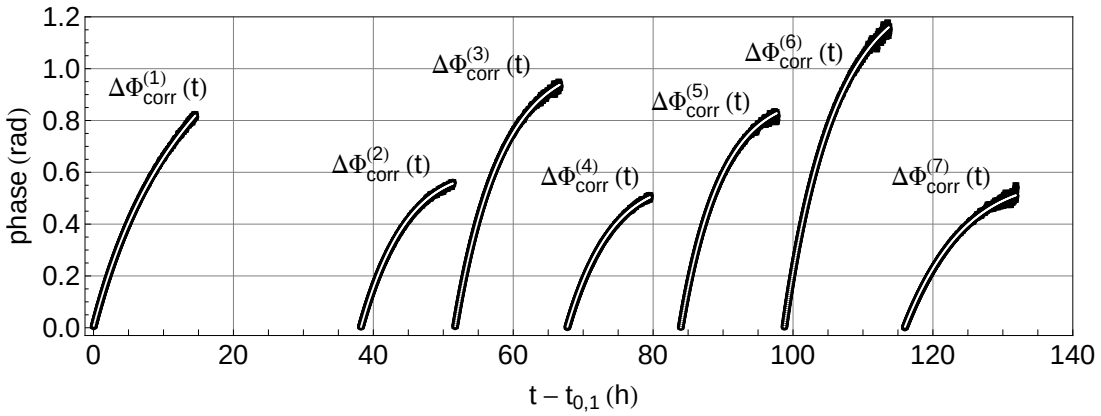

Figure 4.20: Weighted phase differences with fit function (white) for the combined fit of measurements C92-C103 (one data point comprises 50 sub-data sets).

The Lorentz-violating parameter that corresponds to this amplitude is

$$\tilde{b}_{\perp}^{\mathrm{n}} = \sqrt{(\tilde{b}_{\mathrm{X}}^{\mathrm{n}})^2 + (\tilde{b}_{\mathrm{Y}}^{\mathrm{n}})^2} = (5.55 \pm 5.61) \cdot 10^{-32} \text{ GeV} \quad (95\% \text{ CL}), \tag{4.55}$$

where the error $\delta\tilde{b}_{\perp}^{\mathrm{n}}$ is again the 95% confidence error. This error can be regarded as a limit for Lorentz-violating effects for the neutron. A more stringent limit we get from the combined fit of all measurements described in the next section.

4.4.2 Combined fit of all measurements

For the combined fit of the phase differences $\Delta\Phi_{\mathrm{rem}}^{(\mathrm{j})}(t)$ of all 7 runs, the piecewise defined fit function of Eq. (4.42) was used. Besides the two Lorentz-violating parameters a_{s} and a_{c}, it contains $(7 \cdot 6)$ parameters ($\Phi_0^{(\mathrm{j})}$, $\Delta\omega_{\mathrm{lin}}^{(\mathrm{j})}$, $E_{\mathrm{he}}^{(\mathrm{j})}$, $E_{\mathrm{xe}}^{(\mathrm{j})}$, $T_{2,\mathrm{he}}^{*(\mathrm{j})}$ and $T_{2,\mathrm{xe}}^{*(\mathrm{j})}$ with $j = 1, \ldots, 7$) that are defined for the individual runs, i.e., in the interval $t_{0,\mathrm{j}} \leq t \leq (t_{0,\mathrm{j}} + N_{\mathrm{j}} \cdot \tau)$, where $t_{0,\mathrm{j}}$ and N_{j} are the starting times and the number of sub-data sets for run (j), respectively. As before in the single fits, for the T_2^* times the values that were determined by the amplitude fit were used as starting parameters (see Tab. 4.3), and the fit routine was only allowed to vary the values within their errors ($\delta T_{2,\mathrm{he/xe}}^* \approx 1\mathrm{s}$). The weighted phase differences for all measurements together with the fitted function are shown in Fig. 4.20. The χ^2/dof for the fit was 1.868, so here again the errors are re-scaled such that the χ^2 per degree of freedom gets one. The fitting results for all parameters with the correlated and uncorrelated errors are shown in Tab. 4.6.

	value	δ_{corr}	δ_{uncorr}		value	δ_{corr}	δ_{uncorr}
a_{c} (mrad)	-0.882	0.814	0.015	a_{s} (mrad)	-2.067	1.057	0.019
$\Phi_0^{(1)}$ (rad)	0.999	0.035	3.01E-5	$E_{\text{xe}}^{(1)}$ (rad)	-0.159	0.007	4.30E-5
$\Phi_0^{(2)}$ (rad)	0.851	0.017	3.88E-5	$E_{\text{xe}}^{(2)}$ (rad)	-0.046	0.008	5.51E-5
$\Phi_0^{(3)}$ (rad)	1.183	0.014	3.31E-5	$E_{\text{xe}}^{(3)}$ (rad)	-0.182	0.006	4.68E-5
$\Phi_0^{(4)}$ (rad)	0.739	0.014	4.50E-5	$E_{\text{xe}}^{(4)}$ (rad)	-0.048	0.009	6.35E-5
$\Phi_0^{(5)}$ (rad)	1.036	0.011	2.62E-5	$E_{\text{xe}}^{(5)}$ (rad)	-0.128	0.005	3.71E-5
$\Phi_0^{(6)}$ (rad)	1.456	0.014	2.83E-5	$E_{\text{xe}}^{(6)}$ (rad)	-0.144	0.004	4.01E-5
$\Phi_0^{(7)}$ (rad)	0.720	0.014	2.97E-5	$E_{\text{xe}}^{(7)}$ (rad)	0.007	0.005	4.20E-5
$\Delta\omega_{\text{lin}}^{(1)}$ ($\frac{\mu\text{rad}}{\text{s}}$)	2.367	0.397	2.69E-9	$E_{\text{he}}^{(1)}$ (rad)	-0.835	0.042	3.46E-5
$\Delta\omega_{\text{lin}}^{(2)}$ ($\frac{\mu\text{rad}}{\text{s}}$)	-2.609	0.267	3.75E-9	$E_{\text{he}}^{(2)}$ (rad)	-0.803	0.025	4.74E-5
$\Delta\omega_{\text{lin}}^{(3)}$ ($\frac{\mu\text{rad}}{\text{s}}$)	-1.393	0.228	3.37E-9	$E_{\text{he}}^{(3)}$ (rad)	-0.998	0.020	4.02E-5
$\Delta\omega_{\text{lin}}^{(4)}$ ($\frac{\mu\text{rad}}{\text{s}}$)	-1.904	0.238	4.50E-9	$E_{\text{he}}^{(4)}$ (rad)	-0.690	0.023	5.53E-5
$\Delta\omega_{\text{lin}}^{(5)}$ ($\frac{\mu\text{rad}}{\text{s}}$)	-1.495	0.184	3.22E-9	$E_{\text{he}}^{(5)}$ (rad)	-0.911	0.015	3.15E-5
$\Delta\omega_{\text{lin}}^{(6)}$ ($\frac{\mu\text{rad}}{\text{s}}$)	-1.118	0.235	3.34E-9	$E_{\text{he}}^{(6)}$ (rad)	-1.313	0.018	3.34E-5
$\Delta\omega_{\text{lin}}^{(7)}$ ($\frac{\mu\text{rad}}{\text{s}}$)	-1.249	0.206	3.21E-9	$E_{\text{he}}^{(7)}$ (rad)	-0.725	0.019	3.49E-5

Table 4.6: Best-fit parameters for the combined fit of C92-C103 with correlated and uncorrelated 1σ-errors determined by a χ^2 fit using the model (4.42). The T_2^* times are not listed because they were only varied within their error of ≤ 1 s and thus do not differ nameable from the values in Tab. 4.3.

Now we can again calculate the rms magnitude of the sidereal phase Φ_{SD} and the corresponding frequency ν_{SD} from Eq. (4.53) and (4.54). We get

$$\begin{aligned} \Phi_{\text{SD}} &= (2.25 \pm 2.29)\ \text{mrad} \quad (95\%\ \text{CL}) && (4.56) \\ \text{and}\quad \nu_{\text{SD}} &= (26.1 \pm 26.6)\ \text{nHz} \quad (95\%\ \text{CL}), && (4.57) \end{aligned}$$

where the uncertainties are again the 95% confidence errors. Now the Lorentz-violating parameters for the neutron, $\tilde{b}_{\text{X}}^{\text{n}}$ and $\tilde{b}_{\text{Y}}^{\text{n}}$ according to Eq. (4.51), as well as $\tilde{b}_{\perp}^{\text{n}} = \sqrt{\tilde{b}_{\text{X}}^{\text{n}} + \tilde{b}_{\text{Y}}^{\text{n}}}$, can be given as:

$$\begin{aligned} \tilde{b}_{\text{X}}^{\text{n}} &= (3.36 \pm 3.44) \cdot 10^{-32}\ \text{GeV}\ (2\sigma), \\ \tilde{b}_{\text{Y}}^{\text{n}} &= (1.43 \pm 2.65) \cdot 10^{-32}\ \text{GeV}\ (2\sigma), \\ \tilde{b}_{\perp}^{\text{n}} &= (3.65 \pm 3.72) \cdot 10^{-32}\ \text{GeV}\ (95\%\ \text{CL}). \end{aligned} \qquad (4.58)$$

4.4.3 Errors, correlations and sensitivity

When we compare the 95% confidence limits for $\tilde{b}_{\perp}^{\mathrm{n}}$ achieved with the single fits (Eq. (4.55)) and the combined fit (Eq. (4.58)), we see that the latter one is a factor 1.5 smaller. So with the combined fit we are slightly more sensitive as with building the mean value for a_{c} and a_{s} out of the 7 single fits. The problem of both fits are the strong correlations between the Lorentz-violating parameters $a_{\mathrm{c,s}}$ and the other parameters, which lead to a high correlated error. For the single fits these correlations have a bigger effect than for the combined fit.

Tab. 4.5 and Tab. 4.6 show that, both for the single fits and the combined fit, the uncorrelated errors of a_{c} and a_{s} are about 2 orders of magnitude smaller than the correlated errors. This means that the sensitivity of our experiment is not limited by the uncorrelated error and therewith the signal-to-noise ratio, but only by the strong correlations between the parameters. This was confirmed also by repeating the analysis with only one SQUID channel instead of two channels in gradiometer configuration. Even though the noise is reduced significantly with the gradiometer (see Fig. 4.5), the comparison of both analyses showed that the correlated errors of the fit parameters do not differ a lot.

The correlations are caused by a piecewise similar time structure of the remaining phase difference and the sidereal phase modulation in the fit function of Eq. (4.42). On a closer look, this can be traced back to the relatively short T_2^* times of ^{129}Xe (compared to the sidereal period $T_{\mathrm{SD}} = \frac{2\pi}{\Omega_{\mathrm{E}}} = 23$ h 56 min 4.091 s) that enter in the argument of the exponential terms of Eq. (4.41). In order to show that longer $T_{2,\mathrm{xe}}^*$ times would increase the sensitivity significantly, we repeated the combined fit of the weighted phase differences and changed the fit-model of Eq. (4.42) replacing Ω_{E} by $\Omega_{\mathrm{E}}^{'} = g \cdot \Omega_{\mathrm{E}}$, i.e., the sidereal period T_{SD} changes to $T_{\mathrm{SD}}^{'} = T_{SD}/g$. In this way the time structure of the sidereal phase modulation is changed relative to the time structure of the weighted phase difference. Tab. 4.7 shows the results of the fits with multiples of Ω_{E}. The correlated error of $a_{\mathrm{c,s}}$ approaches the uncorrelated one already for $g \geq 3$. The uncorrelated error, however, is only marginally affected by this procedure, as expected. The data in Tab. 4.7 also show that with increasing g the magnitudes of a_{s} and a_{c} scale down, too, being consistent with zero within their $3\sigma_{\mathrm{corr}}$-errors. If we take, for example, the fit results for $\Omega_{\mathrm{E}}^{'} = 2 \cdot \Omega_{\mathrm{E}}$ and calculate again the rms magnitude of the sidereal variation, together with its 95% confidence level with help of Eq. (4.52), we get $\Phi_{\mathrm{SD}}^{\prime} = (0.16 \pm 0.28)$ mrad. This would mean an increase in sensitivity of a factor 8. Thus, it is very important to improve the relaxation properties for ^{129}Xe, because increasing $T_{2,\mathrm{xe}}^*$ by a factor of two should have the same effect as lowering the sidereal period T_{SD} by the same factor.

Ω'_{E}	a_{c} (mrad)	$\delta_{\mathrm{ac}}^{\mathrm{corr}}$ (mrad)	$\delta_{\mathrm{ac}}^{\mathrm{uncorr}}$ (mrad)	a_{s} (mrad)	$\delta_{\mathrm{as}}^{\mathrm{corr}}$ (mrad)	$\delta_{\mathrm{as}}^{\mathrm{uncorr}}$ (mrad)
$0.5{\cdot}\Omega_{\mathrm{E}}$	3.353	6.572	0.018	0.488	7.991	0.016
Ω_{E}	-0.882	0.814	0.015	-2.067	1.057	0.019
$2{\cdot}\Omega_{\mathrm{E}}$	-0.048	0.120	0.016	-0.149	0.112	0.017
$3{\cdot}\Omega_{\mathrm{E}}$	-0.184	0.052	0.019	-0.011	0.043	0.016
$4{\cdot}\Omega_{\mathrm{E}}$	-0.001	0.034	0.018	0.057	0.030	0.016

Table 4.7: Results for a_{c} and a_{s} out of the χ^2-fit of the weighted phase difference according to Eq. (4.42), where the angular frequency of the sidereal day Ω_{E} is replaced by multiples of Ω_{E}, i.e., $\Omega'_{\mathrm{E}} = g \cdot \Omega_{\mathrm{E}}$. The correlated errors are reduced significantly for higher multiples of Ω_{E}, where the time structures of the remaining phase difference and the sidereal phase modulation differ more and more.

The correlations can also be quantified with the help of the *linear correlation coefficient* $\rho_{\mathrm{x,y}}$ between two parameters x and y that is defined as [50]

$$\rho_{\mathrm{x,y}} = \frac{cov(x,y)}{\sigma_{\mathrm{x}}\sigma_{\mathrm{y}}} \ , \quad -1 \leq \rho_{\mathrm{x,y}} \leq 1 \ , \tag{4.59}$$

where $cov(x,y) =$ is the covariance[6] between the two parameters and $\sigma_{\mathrm{x(y)}}$ their standard (1σ-) error. $\rho_{\mathrm{x,y}}$ is a measure for the degree of linear dependence between the variables: the closer the coefficient is to either -1 or 1, the stronger the (anti-) correlation between the variables. As example, in Tab. 4.8 the correlation coefficients for the parameters of the single fits of C92 (run 1) and C99 (run 4) are listed. Many values of $|\rho_{\mathrm{x,y}}|$ are very close to 1, which leads to a large uncertainty in the parameters. The correlation coefficient $|\rho_{\mathrm{as/ac,y}}|$ between $a_{\mathrm{c/s}}$ and the other parameters ($y = \Phi_0,\ \Delta\omega_{\mathrm{lin}},\ E_{\mathrm{He}},\ E_{\mathrm{Xe}}$) strongly depends on the sidereal starting phase $\varphi_{\mathrm{SD}}^{\mathrm{j}}$ for the individual run. This can be seen when we compare $|\rho_{\mathrm{as/ac,y}}|$ for C92 and C99. For C92 ($\varphi_{\mathrm{SD}}^{1} = 2\pi \cdot 0.4051$) we have $|\rho_{\mathrm{as,y}}| \approx 1$, while $|\rho_{\mathrm{ac,y}}|$ is always smaller than 0.13. For C99 ($\varphi_{\mathrm{SD}}^{4} = 2\pi \cdot 0.2343$), in contrast, $|\rho_{\mathrm{as,y}}|$ is always smaller than 0.16, while $|\rho_{\mathrm{ac,y}}| \approx 1$. Tab. 4.9 shows the correlation coefficients for a_{c} and a_{s} for the combined fit, where 3 of them are ≥ 0.9, and 11 of them are ≥ 0.8. This is still a high correlation, but not as strong as in the single fits. This is the reason why the sensitivity is improved with the combined fit, compared to the averaged result of the 7 single fits.

[6]The covariance is defined as $cov(x,y) = E[(x-\mu_{\mathrm{x}})(y-\mu_{\mathrm{y}})]$, where E is the expected value operator and $\mu_{\mathrm{x(y)}}$ the mean value of $x(y)$.

		a_s	a_c	Φ_0	$\Delta\omega_\mathrm{lin}$	E_He	E_Xe
C92	a_s	1.000	-0.012	0.999	-0.998	-0.998	0.988
	a_c	-0.012	1.000	-0.003	0.034	-0.018	0.121
	Φ_0	0.999	-0.003	1.000	-1.000	-1.000	0.992
	$\Delta\omega_\mathrm{lin}$	-0.998	0.034	-1.000	1.000	0.999	-0.988
	E_he	-0.998	-0.018	-1.000	0.999	1.000	-0.994
	E_xe	0.988	0.121	0.992	-0.988	-0.994	1.000
C99	a_s	1.000	-0.031	0.056	-0.020	-0.095	0.159
	a_c	-0.031	1.000	-0.999	0.999	0.997	-0.990
	Φ_0	0.056	-0.999	1.000	-0.999	-0.999	0.994
	$\Delta\omega_\mathrm{lin}$	-0.020	0.999	-0.999	1.000	0.997	-0.990
	E_he	-0.095	0.997	-0.999	0.997	1.000	-0.998
	E_xe	0.159	-0.990	0.994	-0.990	-0.998	1.000

Table 4.8: Linear correlation coefficient $\rho_\mathrm{x,y}$ (see Eq. (4.59)) between the parameters for the fit of run (1) (C92) and run (4) (C99).

	a_c	a_s		a_c	a_s
a_c	1.00	0.06	a_s	0.06	1.00
$\Phi_0^{(1)}$	0.09	**0.94**	$E_\mathrm{xe}^{(1)}$	0.45	**0.82**
$\Phi_0^{(2)}$	-0.31	**-0.85**	$E_\mathrm{xe}^{(2)}$	-0.59	-0.59
$\Phi_0^{(3)}$	0.62	0.70	$E_\mathrm{xe}^{(3)}$	**0.82**	0.25
$\Phi_0^{(4)}$	-0.73	0.11	$E_\mathrm{xe}^{(4)}$	-0.46	0.48
$\Phi_0^{(5)}$	0.25	**-0.86**	$E_\mathrm{xe}^{(5)}$	-0.18	**-0.86**
$\Phi_0^{(6)}$	0.38	**0.85**	$E_\mathrm{xe}^{(6)}$	0.70	0.49
$\Phi_0^{(7)}$	-0.76	0.44	$E_\mathrm{xe}^{(7)}$	-0.33	**0.80**
$\Delta\omega_\mathrm{lin}^{(1)}$	0.02	**-0.94**	$E_\mathrm{he}^{(1)}$	-0.16	**-0.94**
$\Delta\omega_\mathrm{lin}^{(2)}$	0.18	**0.87**	$E_\mathrm{he}^{(2)}$	0.44	0.77
$\Delta\omega_\mathrm{lin}^{(3)}$	-0.48	-0.79	$E_\mathrm{he}^{(3)}$	-0.73	-0.56
$\Delta\omega_\mathrm{lin}^{(4)}$	0.73	0.10	$E_\mathrm{he}^{(4)}$	0.64	-0.30
$\Delta\omega_\mathrm{lin}^{(5)}$	-0.42	0.76	$E_\mathrm{he}^{(5)}$	-0.07	**0.89**
$\Delta\omega_\mathrm{lin}^{(6)}$	-0.24	**-0.88**	$E_\mathrm{he}^{(6)}$	-0.50	-0.77
$\Delta\omega_\mathrm{lin}^{(7)}$	**0.83**	-0.24	$E_\mathrm{he}^{(7)}$	0.64	-0.59

Table 4.9: Linear correlation coefficient $\rho_\mathrm{x,y}$ (see Eq. (4.59)) between the Lorentz-violating parameters $a_\mathrm{c/s}$ and the other parameters for the combined fit of runs (1) to (7). Values of $|\rho_\mathrm{x,y}|$ that are larger than 0.8, which means a relatively high correlation, are printed in bold type.

Chi-square

Both for the single fits and the combined fit, the chi-square per degree of freedom χ^2/dof was too large. This was made allowance for by re-scaling the errors such that $\chi^2/dof = 1$, i.e., multiplying the errors with the factor $S = \sqrt{\chi^2/dof}$. One reason for the large χ^2/dof lies in the fact that already the model for the raw data fit (4.3) is not perfect: The offset drift can also have higher order terms, there can be other frequency components in the signal due to microphonic effects that are not completely suppressed by the gradiometer (see Fig. 4.11), and there can be jumps in the SQUID offset (we can not be sure that all sub-data sets with jumps were discarded, because also very small jumps could happen). For these reasons, the data is not normally distributed. This leads to the fact that the errors for the amplitudes $A_{\mathrm{he/xe}}$ and $B_{\mathrm{he/xe}}$ are underestimated by the fit, which involves that the phase errors are underestimated as well. In addition, also the model for the fit of the weighted phase difference is only an approximation, as higher order terms of the RBS-shift discussed in Sec. 4.3.3 were neglected. But a more complex model that contains higher order terms of Eq. (4.28) would be difficult to fit without having appropriate starting values, because then the fit function would be nonlinear in the parameters. For this reason we have chosen the linear model of Eq. (4.42) for the fit of the weighted phase difference, using the T_2^* times out of the amplitude fit.

4.4.4 Residuals and comparison with other experiments

In Fig. 4.21 the residuals of the combined fit are shown: The function $\sum_{\mathrm{j}=1}^{7} \Phi_{\mathrm{fit}}^{\prime(\mathrm{j})}(t)$, i.e., the part of the model (4.42) *without* the sine/cosine term, is subtracted from the data to show the remaining phase variations. The gray curve is the sine/cosine term of (4.42) with the best-fit parameters for a_{s} and a_{c}, inside the error band that shows the correlated error at 95% confidence level. Although the plot suggests a sidereal variation, our result is consistent with the null hypothesis "no Lorentz-violation" within the 95% confidence error. The variations in the phase residuals are due to the strong correlations between the parameters, which can also be seen by doing a fit without the sine/cosine term, i.e., with the model $\Phi_{\mathrm{fit}}^{\prime}(t) = \sum_{\mathrm{j}=1}^{7} \Phi_{\mathrm{fit}}^{(\mathrm{j})}(t)$ (with $\Phi_{\mathrm{fit}}^{(\mathrm{j})}(t)$ of Eq. (4.41)). The chi-square for this fit is the same as in the fit before ($\chi^2/dof = 1.868$), which means that a set of parameters without $a_{\mathrm{s/c}}$ exists that fits as good as the parameter set that includes a_{s} and a_{c}. In Fig. 4.22 the residuals of this fit are plotted, where no sidereal variation can be seen.

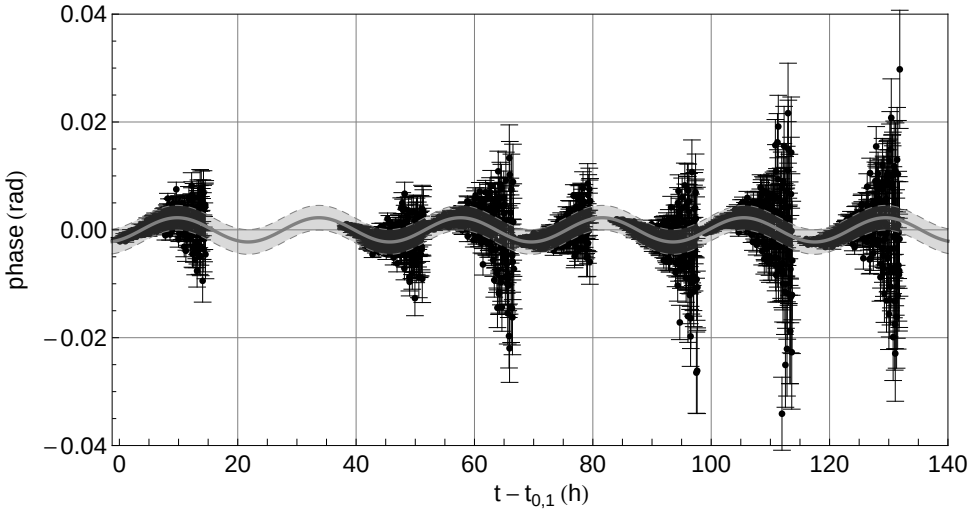

Figure 4.21: Residuals of the combined fit using the model (4.42) *with* sine/cosine term (one data point comprises 50 sub-data sets, i.e., $\Delta t = 64$ s). The function $\sum_{\mathrm{j}=1}^{7} \Phi_{\mathrm{fit}}^{\prime(\mathrm{j})}(t)$, i.e., the part of function (4.42) *without* the sine/cosine term, is subtracted from the data to show the remaining phase variations. The gray curve is the sine/cosine term of the fit function with the best-fit parameters for a_{s} and a_{s}, together with the error band at 95% CL.

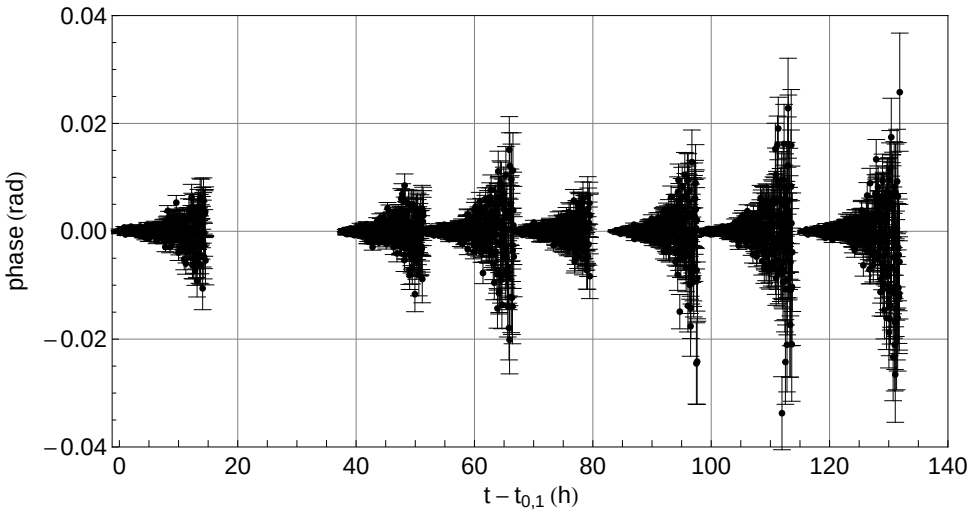

Figure 4.22: Residuals of the combined fit using the model $\sum_{\mathrm{j}=1}^{7} \Phi_{\mathrm{fit}}^{\prime(\mathrm{j})}(t)$, i.e., the part of Eq. (4.42) *without* sine/cosine term (one data point comprises 50 sub-data sets). The plot shows the remaining phase noise after the subtraction of the fit function from the data. No sidereal variation is visible.

Electron/Proton			Neutron		
$\tilde{b}_X^e$	$(-0.9 \pm 1.4) \cdot 10^{-31}$	[30]	$\tilde{b}_X^n$	$(0.1 \pm 3.2) \cdot 10^{-33}$	[14]
$\tilde{b}_Y^e$	$(-0.9 \pm 1.4) \cdot 10^{-31}$	[30]	$\tilde{b}_Y^n$	$(2.5 \pm 3.2) \cdot 10^{-33}$	[14]
$\tilde{b}_X^p$	$< 6 \cdot 10^{-32}$	[14]	$\tilde{b}_X^n$	$(2.2 \pm 7.9) \cdot 10^{-32}$	[15]
$\tilde{b}_Y^p$	$< 6 \cdot 10^{-32}$	[14]	$\tilde{b}_Y^n$	$(8.0 \pm 9.5) \cdot 10^{-32}$	[15]
			$\tilde{b}_X^n$	$(3.4 \pm 3.4) \cdot 10^{-32}$	[this work]
			$\tilde{b}_Y^n$	$(1.4 \pm 2.6) \cdot 10^{-32}$	[this work]

Table 4.10: Sensitivities of other experiments for the Lorentz-violating coefficients $\tilde{b}_X$ and $\tilde{b}_Y$ (in GeV) for electron, proton and neutron. The errors are the 2σ-errors.

Comparison with other experiments

Now the sensitivity of our experiment can be compared to the one reached in other experiments. In Tab. 4.10 the most sensitive measurements so far for $\tilde{b}_X$ and $\tilde{b}_Y$ for protons, neutrons and electrons are shown, where the values are given in GeV and the uncertainty is the 2σ-error [45]. The limit for the electron parameters is the one from the experiment with the spin polarized torsion pendulum that was described in Chap. 1.3.3. It is about a factor 5 larger than our limit for the neutron. The proton limit given in the table stems from a recent measurement with the K-^{3}He comagnetometer (see Chap. 1.3.2), and is twice as large as our value. The same experiment gives the currently best limit for Lorentz-violating effects for the neutron, which is roughly one order of magnitude smaller than the limit from our experiment. For comparison, the values determined by the ^{3}He/^{129}Xe maser experiment (see Chap. 1.3.1) are shown as well, which are a factor 2-3 larger than our values.

Chapter 5

Conclusion and outlook

In this thesis a clock-comparison experiment was presented, in which the free spin precession of co-located, spin polarized ^{3}He and ^{129}Xe atoms was monitored with the help of highly sensitive SQUID detectors. The spin coherence times were measured to be up to 4.4 hours for ^{129}Xe and 14.1 hours for ^{3}He at total pressures of 40 - 50 mbar. In a measurement with ^{3}He alone, at a smaller pressure of 4.5 mbar, a coherence time of about 60 hours was reached, which is the longest coherent spin relaxation time of a macroscopic sample measured so far.

The ^{3}He/^{129}Xe spin clock is sensitive to non-magnetic spin-dependent interactions, e.g., the coupling of the nuclear spin to a Lorentz-violating background field $\vec{\tilde{b}}^{\mathrm{n}}$ as described in the minimal Standard Model Extension [44], which would lead to a sidereal modulation of the relative ^{3}He/^{129}Xe phases or frequencies. Our experiment constrains the Lorentz-violating parameters $\tilde{b}^{\mathrm{n}}_{\mathrm{X(Y)}}$ for the neutron to be

$$\tilde{b}^{\mathrm{n}}_{\mathrm{X}} < 3.44 \cdot 10^{-32}\ \mathrm{GeV}\ , \quad \tilde{\mathrm{b}}^{\mathrm{n}}_{\mathrm{Y}} < 2.65 \cdot 10^{-32}\ \mathrm{GeV}\ ,$$

where the limit is the 2σ-error. This is about a factor 2-3 smaller than the values from the ^{3}He/^{129}Xe maser experiment [15]. In a recent experiment, where a K- ^{3}He co-magnetometer was used [14], the sensitivity of our experiment was exceeded by one order of magnitude. For their analysis 143 days of data were used, while we got our limit from 7 measurements of 12 - 16 hours length. If one considers the uncorrelated error for the combined fit, which follows the $\propto T^{-3/2}$ power law according to the Cramer Rao Lower Bound of Eq. (3.4), one can see that it is about a factor 50 smaller than the correlated error (see Tab. 4.6). This shows clearly that, for measurement times smaller than about 3 $T^*_{2,\mathrm{xe}}$, the sensitivity of the experiment is limited through the strong correlations between the fit parameters,

and not through the signal-to-noise ratio, which is $SNR \geq 1000$ at the beginning of each measurement and decreases exponentially due to the T_2^* relaxation. To reduce the correlations, it is necessary to change the time structure of the weighted phase difference relative to the time structure of the sidereal phase modulation. The fit of the weighted phase difference described in the previous section, where the sidereal frequency was changed to $\Omega_{\mathrm{E}}^{'} = g \cdot \Omega_{\mathrm{E}}$, showed that the correlated errors for a_{c} and a_{c} are reduced significantly with increasing g. Considering, for example, the fit results for $\Omega_{\mathrm{E}}^{'} = 2 \cdot \Omega_{\mathrm{E}}$ (see Tab. 4.7), the 95% confidence level of the rms magnitude of the sidereal phase $\Phi_{\mathrm{SD}}^{\prime}$ becomes a factor 8 smaller. Increasing the ^{129}Xe relaxation time by a factor 2 should have the same effect as multiplying the sidereal frequency Ω_{E} by the same factor. Thus, to increase the sensitivity of the experiment, it will be necessary to improve the relaxation properties for ^{129}Xe.

Optimizing the transverse relaxation time of ^{129}Xe

As the SNR does not limit the sensitivity of our experiment at the moment, one possibility to improve the ^{129}Xe relaxation time is to decrease the ^{129}Xe and N_2 pressures. In Chap. 4.2.4, the field gradient $G := |\vec{\nabla} B_{1,\mathrm{x}}| = |\vec{\nabla} B_{1,\mathrm{y}}| = |\vec{\nabla} B_{1,\mathrm{z}}|$ and the wall relaxation time for ^{129}Xe were estimated out of the measured transverse relaxation times to be $G = 48.8$ pT/cm and $T_{1,\mathrm{wall}}^{\mathrm{xe}} \approx 7.7$ h. Based on these values, the transverse relaxation time for ^{129}Xe due to gradient and van der Waals relaxation, i.e., $T_{2,\mathrm{xe}} = \left(\frac{1}{T_{2,\mathrm{field}}^{\mathrm{xe}}} + \frac{1}{T_{2,\mathrm{vdW}}^{\mathrm{xe}}}\right)^{-1}$, can now be optimized by varying the pressures for ^{129}Xe and N_2. The ^{3}He pressure effects $T_{2,\mathrm{xe}}$ only marginally and thus is kept fixed at 1 mbar. In Fig. 5.1 the relaxation time $T_{2,\mathrm{xe}}$ is shown as function of the N_2 pressure for ^{129}Xe pressures of 1 mbar, 2 mbar and 4 mbar. With decreasing p_{xe}, the relaxation time increases, and reaches its maximal value of $T_{2,\mathrm{xe}} = 35.1$ h for $p_{\mathrm{xe}} = 1$ mbar and $p_{\mathrm{N2}} \approx 17$ mbar. Comprising again the wall relaxation time $T_{1,\mathrm{wall}}^{\mathrm{xe}} \approx 7.7$ h (the binary relaxation can be neglected here), one gets a total relaxation time of $T_{2,\mathrm{xe}}^{*} \approx 6.3$ h, which is already a factor 1.4 larger than the 4.4 h reached in run (1). Assuming equal ^{129}Xe polarizations, reducing the ^{129}Xe pressure to 1 mbar would mean a factor 8 loss in the SNR compared to run C92 where the ^{129}Xe pressure was 8.3 mbar. But as the correlated error for $a_{\mathrm{c(s)}}$ was about a factor 50 larger than the uncorrelated error, this should still not constrain the sensitivity of the experiment.

However, the limiting relaxation mechanism for ^{129}Xe is the wall relaxation. From Eq. (2.29) we know that the wall relaxation time $T_{1,\mathrm{wall}}$ is proportional to the volume-to-surface ratio V/S, i.e., $T_{1,\mathrm{wall}}(R) = c \cdot \frac{V}{S} = c \cdot \frac{4/3\pi R^3}{4\pi R^2} = c \cdot \frac{R}{3}$. Let us assume for the moment that

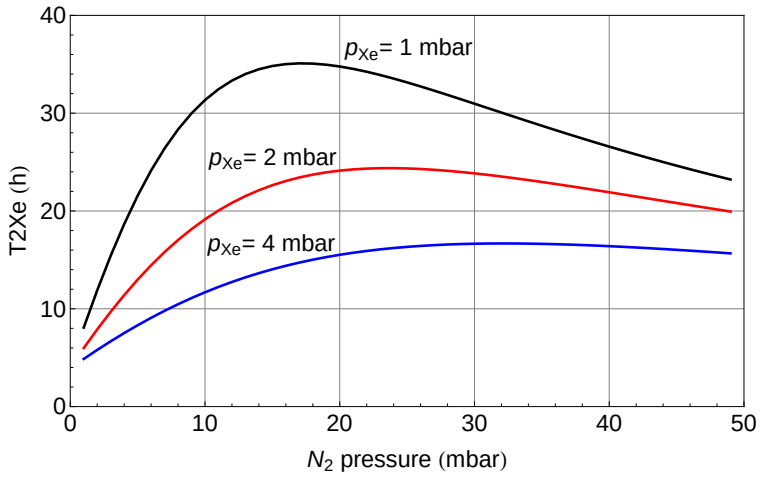

Figure 5.1: Calculated ^{129}Xe relaxation time $T_{2,\mathrm{xe}} = \left(\frac{1}{T^{\mathrm{xe}}_{2,\mathrm{field}}} + \frac{1}{T^{\mathrm{xe}}_{2,\mathrm{vdW}}}\right)^{-1}$ due to gradient and van der Waals relaxation for 3 different ^{129}Xe pressures as a function of the nitrogen buffer-gas pressure in a ^{3}He/^{129}Xe/N_2 gas mixture ($p_{\mathrm{he}} = 1$ mbar).

one could build a cell that has exactly the same characteristics as the one used for the clock-comparison measurements, but a different radius R'. Then the ^{129}Xe wall relaxation time of this cell would be $T^{\mathrm{xe}}_{1,\mathrm{wall}}(R') = 7.7\ \mathrm{h} \cdot \frac{\mathrm{R'}}{2.9\ \mathrm{cm}}$. Based on this assumption, we can optimize again the total transverse relaxation time reached with the parameters above ($p_{\mathrm{xe}} = p_{\mathrm{xe}} = 1$ mbar, $p_{\mathrm{N2}} \approx 17$ mbar and $G = 48.8$ pT/cm.), now varying the cell radius. The best value $T^*_{2,\mathrm{xe}} \approx 6.53$ h is reached for $R' = 3.4$ cm. So for these field gradients we cannot gain much by enlarging the cell, as the radius contributes in the 4th power to the gradient relaxation (see Eq. (2.40)). But if we could reduce the gradients by, e.g., a factor of two, we would get a $T^*_{2,\mathrm{xe}}$ time of already 8.4 h for a cell radius of 4.5 cm, where $T_{1,\mathrm{wall}} \approx 12$ h. The field homogeneity could be improved by optimizing the coil positioning, or by further demagnetizing the Dewar (see App. C.2).

These considerations show that there is still room for improvements concerning the transverse relaxation time of ^{129}Xe. Besides the reduction of the correlations between the fit parameters, an enlargement of $T^*_{2,\mathrm{xe}}$ would also lead to longer observation times T and therewith an additional increase in sensitivity due to the $\propto T^{-3/2}$ dependence according to CRLB (Eq. (3.4)). A further improvement is reached by increasing the total measurement time to a period of about 100 days. In addition to the gain in statistics, the long time span provides an important separation between sidereal and possible diurnal variations.

Appendix A

Chi-square minimization

This appendix is a short summary of Chap. 15 of Ref. [62]. Given a set of N measured data points $(x_\mathrm{i}, y_\mathrm{i})$ with i = 0, ..., N-1, the problem is now to fit the data to a model (fit function)

$$y(x) = y(x; a_0, ..., a_{M-1}) \tag{A.1}$$

that has M free parameters a_j with j = 0, ..., M-1. One method to do this is the so-called *maximum-likelihood estimation*, which means that one has to find those values for the parameters that maximize the likelihood of the parameters to give the measured data points, or, in other words, that maximize the probability of the measured data set to give these parameters. They are then called the *best-fit parameters*. Suppose that each data point y_i has an independent and normally distributed measurement error with standard deviation σ_i. Then the probability of the data set is the product of the probabilities of the single data points,

$$P \propto \prod_{\mathrm{i}=0}^{\mathrm{N}-1} \exp\left[-\frac{1}{2}\left(\frac{y_\mathrm{i} - y(x_\mathrm{i})}{\sigma_i}\right)^2\right] \Delta y \ , \tag{A.2}$$

where Δy is some constant factor. Maximizing Eq. (A.2) is equivalent to minimizing its negative logarithm,

$$\sum_{\mathrm{i}=0}^{\mathrm{N}-1} \frac{[y_\mathrm{i} - y(x_\mathrm{i})]^2}{2\sigma_i^2} - N \log \Delta y \ . \tag{A.3}$$

Since N and Δy are constant, one just has to minimize the quantity

$$\chi^2 \equiv \sum_{\mathrm{i}=0}^{\mathrm{N}-1} \left(\frac{y_\mathrm{i} - y(x_\mathrm{i})}{\sigma_i}\right)^2 \ , \tag{A.4}$$

which is called *chi-square*. So maximizing the likelihood is equal to minimizing the chi-square. The chi-square function is one representation of a so-called *figure-of-merit function* that measures the agreement between the data and the model: small values represent a close agreement. The probability distribution for the chi-square in Eq. (A.4) is given by the chi-square distribution for $\nu = N - M$ degrees of freedom[1] (*dof*). The probability density function (PDF) of the chi-square distribution is given by

$$PDF(x;\nu) = \frac{e^{-\mathrm{x}/2}\ x^{\nu/2-1}}{2^{\nu/2}\ \Gamma(\nu/2)}\ , \tag{A.5}$$

where $\Gamma(x)$ is the Euler gamma function given by $\Gamma(x) = \int_0^\infty t^{\mathrm{x}-1} e^{-\mathrm{t}}\, dt$. In Fig. 4.8 the PDF for $\nu = 15000$ was shown (in the fits described in Chap. 4.4 the degrees of freedom were between $\nu = 13300$ and $\nu = 18000$). For such large values of ν, the chi-square distribution approaches a normal distribution with the mean value $\langle \chi^2/\nu \rangle = 1$ and the standard deviation $\sigma_{\chi^2/\nu} = \sqrt{2\nu - 1}/\nu$.

The probability Q that the minimal chi-square value χ^2_{min} calculated for an experiment with ν degrees of freedom is due to chance was given in Eq. (4.5) (see as well Fig. 4.8). It gives a quantitative measure for the *goodness-of-fit* of the model. If Q is a very small probability, one can conclude that either (i) the model is wrong/incomplete, or (ii) the measurement errors are underestimated, or (iii) the measurement errors may not be normally distributed. As the last case happens quite often, it is not unusual to accept models with $Q > 0.001$.

From the derivatives of Eq. (A.4) with respect to the parameters a_{k} one obtains a set of M (generally nonlinear) equations that must hold at the chi-square minimum χ^2_{min},

$$0 = \sum_{\mathrm{i}=0}^{\mathrm{N}-1} \left(\frac{y_{\mathrm{i}} - y(x_{\mathrm{i}})}{\sigma_i^2} \right) \left(\frac{\partial y(x_{\mathrm{i}}; ...a_{\mathrm{k}}...)}{\partial a_{\mathrm{k}}} \right), \quad k = 0, ..., M-1\ . \tag{A.6}$$

To solve these equations there exist many procedures, for example the often used *Levenberg-Marquardt-algorithm* (see, for example, [58], Chap. 8.6).

Confidence Limits

Solving Eq. (A.6), one gets the minimal chi-square χ^2_{min} and the best-fit-parameters. To

[1] Strictly seen, this is only valid for models that are linear in the parameters, but in most cases one can assume that the chi-square distribution holds also for models that can be linearized in a region around the minimal chi-square χ^2_{min}.

judge about the goodness-of-fit, one can calculate the probability Q. What misses now is some information about the uncertainties of the best-fit-parameters, or what is called the *confidence limits*.

Let us first make some principal considerations: When an experimenter measures some data set $D_{(0)}$, this can be seen as a statistical representation of the true parameter set $\vec{a}_{\text{true}}$ that is unknown to the experimenter. The experimenter now fits the data to a model by doing, e.g., a χ^2 minimization. From this he or she gets best-fit values for the M parameters, $\vec{a}_{(0)}$. Because the data set $D_{(0)}$ has random measurement errors (in addition to possible systematic errors), $D_{(0)}$ is not the only realization of the true parameters $\vec{a}_{\text{true}}$. Every new measurement $D_{(1)}$, $D_{(2)}$, ... would give a slightly different set of best-fit-parameters $\vec{a}_{(1)}$, $\vec{a}_{(2)}$, ... So one can say that these parameter sets are distributed according to some probability distribution in the M-dimensional space of all possible parameter sets $\vec{a}$. The actual measured (fitted) set $\vec{a}_{(0)}$ is one member drawn from this distribution. A *confidence region* (CR) now is a region of that M-dimensional space (normally an M-dimensional ellipsoid), centered around the best-fit-parameters $\vec{a}_{(0)}$, that contains a certain fraction of the total probability distribution. This fraction is called the *confidence level* (CL), and of course it is wishful that it is quite large (e.g. 90 %), because this means to have a "good confidence" in the measured data, i.e., you then could say that "with 90 % probability, the true parameter values lie inside the CR". The confidence *region*, on the other hand, should be small, because this corresponds to small uncertainties (errors) of the parameters. Frequently used CLs in science are 68.3 %, 90%, 95.4%, 99.73% or higher ones. For a normal distribution, a 68.3 %, 95.4% or 99.73% confidence level corresponds to a 1-σ, 2-σ or 3-σ (standard) error, respectively. But also for non-normal distributions these CLs are often used for matters of convention.

Correlated and uncorrelated error

In most cases one is interested in the confidence region, or confidence interval, of one single parameter, say a_1. When a chi-square minimization is used for parameter estimation, this confidence interval is determined as follows: The parameter a_1 is varied by an arbitrary value δa_1, while the other parameters are varied in such a way that the χ^2 is minimized. If we call this minimum χ^2_{a1}, we can define our confidence region by the difference $\Delta\chi^2 \equiv \chi^2_{\text{a1}} - \chi^2_{\text{min}}$. For normally distributed data, the region within which $\Delta\chi^2 < 1$ defines the confidence region for a_1 that contains 68.3% of the probability distribution. In this case the confidence region is equal to the standard error $\sigma_1 = \sqrt{C_{11}}$, that is given by the square root of the corresponding diagonal element of the covariance matrix of the fit. This is what we also call the *correlated error*, because here the correlation between the parameters is accounted

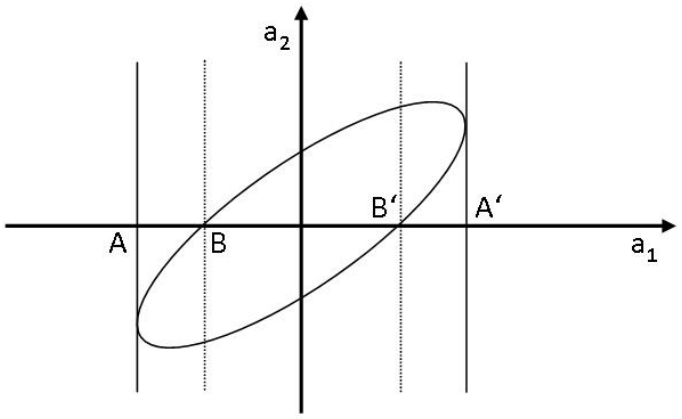

Figure A.1: Confidence region ellipse for the case of two parameters: The projection on the a-axis (interval AA') gives the confidence interval for parameter a that contains 68.3% of normally distributed data, i.e., this interval corresponds to the 1-σ error, or what we call the correlated error. The uncorrelated error is given by the interval BB'. If the principal axes of the confidence region ellipse would be parallel to the coordinate axes, the correlated and uncorrelated errors would be equal, which means that there exist no correlation between the parameters a and b.

for. In Fig. A.1 a confidence region ellipse is shown for the case of two parameters. The projection on the a-axis (interval AA') corresponds to the 1-σ error, i.e., the confidence interval for parameter a_1 that contains 68.3% of normally distributed data.
To determine what we call the *uncorrelated error*, only δa_1 is varied away from the minimum to find the region where $\Delta\chi^2 < 1$, while the other parameters remain fixed. Using this method, the correlations between the parameters are neglected. In the confidence region ellipse in Fig. A.1, this error corresponds to the interval BB'. The uncorrelated error is calculated only to get an idea about the strength of the correlations between the parameters. If the correlated and uncorrelated error are of equal size, it means that the parameters are weakly correlated. In Fig. A.1 this would correspond to the case where the principal axes of the confidence ellipse is parallel to the coordinate axes.

Appendix B

Polarization losses

To estimate the polarization losses during filling and transport into the shielded room, one has to know the polarization in the ^{3}He and ^{129}Xe storage cells at the time of filling, $P_{\text{fill}}^{\text{he/xe}}$, and the polarization at the beginning of the measurement, $P_{\text{meas}}^{\text{he/xe}}$. The latter can be determined out of the amplitudes of the ^{3}He and ^{129}Xe SQUID signals according to Eq. 2.26. For ^{129}Xe the polarization at the time of filling, $P_{\text{fill}}^{\text{xe}}$, is assumed to be equal to the one reached at the ^{129}Xe polarizer, which is about 13 to 14%. This can be done because the ^{129}Xe is always polarized directly before each measurement, and the losses during the transport from the polarizer to the filling station, that takes only about 10 minutes, can assumed to be negligible.

To determine the ^{3}He polarization, $P_{\text{fill}}^{\text{he}}$, one has to consider the losses during the transport from Mainz to PTB, and the losses during the time where the storage cell lies in the Helmholtz field at PTB, i.e., the time between the arrival of the gas and the measurement. The ^{3}He gas that was filled into the storage cells in Mainz always had a pressure of $p_{\text{stor}} \approx 2.1$ bar and a polarization P_{Mz} of about 70%. The T_1 time during transport depends on the wall relaxation time of the storage cell used, $T_{1,\text{stor}}$, the gradient relaxation time in the field of the transport box, $T_{1,\text{box}}$, the relaxation time $T_{1,\text{bin}}$ due to binary collisions, and the duration of the transport, t_{trans}. With these parameters the polarization at the time of arrival of the storage cell at PTB, P_{arr}, can be calculated as:

$$P_{\text{arr}}(t_{\text{trans}}) = P_{\text{Mz}} \cdot e^{-\frac{t_{\text{trans}}}{T_1}} \tag{B.1}$$

$$\text{where} \quad \frac{1}{T_1} = \frac{1}{T_{1,\text{box}}} + \frac{1}{T_{1,\text{stor}}} + \frac{1}{T_{1,\text{bin}}} \, . \tag{B.2}$$

For measurements C92-C95 the storage cell St-1 was used with $T_{1,\text{stor}} \approx 189 \pm 8$ h, while the storage cell for measurements C99-C103, St-14, had a relaxation time of $T_{1,\text{stor}} \approx 231 \pm 7$ h.

	t_{Helm} (h)	$P^{\mathrm{he}}_{\mathrm{fill}}$ (%)	$P^{\mathrm{he}}_{\mathrm{meas}}$ (%)	loss factor	$P^{\mathrm{xe}}_{\mathrm{fill}}$ (%)	$P^{\mathrm{xe}}_{\mathrm{meas}}$ (%)	loss factor
C92	36.42	42.3	8.6	4.9	13.0	7.1	1.8
C94	73.00	31.7	6.2	5.1	14.0	4.9	2.9
C95	86.58	28.5	10.5	2.7	14.0	5.7	2.4
C99	6.50	54.4	14.0	3.9	14.0	4.2	3.3
C101	22.97	48.2	25.5	1.9	14.0	8.0	1.8
C102	37.17	43.7	25.7	1.7	14.0	7.8	1.8
C103	54.83	38.70	11.0	3.5	14.0	7.1	2.0

Table B.1: Overview over the polarization losses for ^{3}He and ^{129}Xe for the measurements C92-C103. t_{Helm} is the duration the storage cell is laying in the Helmholtz field, $P^{\mathrm{he/xe}}_{\mathrm{fill}}$ the estimated polarization of the gas in the storage cell at the time of filling and $P^{\mathrm{he/xe}}_{\mathrm{meas}}$ the polarization determined out of the measured SQUID signal at the beginning of each measurement. In the fifth and eighth column the loss factors are listed for ^{3}He and ^{129}Xe, respectively.

The transport boxes used in both cases had T_1 times of $T_{1,\mathrm{box}} \approx 300$ h at the given pressure of 2.1 bar. The binary relaxation time at this pressure, calculated according to Eq. (2.35) for a temperature of $T = 293$ K, is $T_{1,\mathrm{bin}} = 385$ h. The duration the storage cells were laying in the transport boxes was $t_{\mathrm{trans}} = 19.33$ h for C92-C95, and $t_{\mathrm{trans}} = 20.83$ h for C99-C103. Using these values the polarization in the ^{3}He storage cells at the time of arrival becomes $P_{\mathrm{arr}} = 56.3$ h for C92-C95, and $P_{\mathrm{arr}} = 56.5$ h for C99-C103. For the storage cell St-1 that was used for C92-C95, the polarization was also measured on the day after the arrival at PTB, with a method that is described in [83]: The cell with the polarized ^{3}He is alternately held close to and far away from a magnetic field sensor[1]. The measured field difference then corresponds to the field that is produced by the ^{3}He magnetic moments. Knowing the distance between the sensor and the cell (which was $r = 5.9$ cm), one can then calculate the polarization according to Eq. (2.26). With this method the polarization in cell St-1 25 hours after the arrival was determined to be 46.3%. The calculated polarization, using the values from above, is 47.0%. So this is a quite good agreement.

After arriving at PTB, the storage cell is taken out of the storage box and connected to the filling system, i.e., it is laying in the Helmholtz field during the time t_{Helm} until it is filled into the measurement cell. As explained above, the homogeneity of this field is good enough to neglect the gradient relaxation, so that the polarization in the storage cell at the time of

[1]The three axis magnetometer MAG-03 MS from Bartington with a sensitivity of 10^{-6} Gauss

filling can be calculated as

$$P_{\text{fill}}(t) \quad = \quad P_{\text{arr}} \cdot e^{-\left(\frac{t_{\text{Helm}}}{T_{1,\text{stor}}} + \frac{t_{\text{Helm}}}{T_{1,\text{bin}}}\right)} . \tag{B.3}$$

In Tb. B the calculated ^{3}He and ^{129}Xe polarizations and the corresponding loss factors $P_{\text{fill}}/P_{\text{meas}}$ for each measurement are listed. For ^{129}Xe the loss factor lies between 1.8 and 3.3, for ^{3}He between 1.9 and 5.1. Even though it was paid attention to the reproducibility of the filling and transport process, and care was taken on the critical points discussed in Sec. 4.1.3, for some measurements more than 50% of the polarization was lost. So far it is not clear where these great losses come from, and why in the average more polarization was lost for ^{3}He than for ^{129}Xe. But as the polarization in the storage cell St-1 was measured as decribed above, one can say that the main losses for ^{3}He do happen during the filling and transport at PTB and not during the transport from Mainz to PTB.

Appendix C

Magnetic field: simulations and measurements

C.1 Simulations

To simulate the magnetic field of the B_{x}-coils inside the BMSR-2 (see Fig. 3.6), the program "Comsol 32" was used, which is a simulation environment based on the finite element method. The field was calculated using a 3-dimensional magnetostatic model inside "Comsol 32", where the two quadratical B_{x}-coils were simulated as homogeneously magnetized cuboids with the edge lengths $a = b = 180$ cm and $c = 2$ cm and the magnetization M. The absolute value of the magnetic moment of a coil with n windings and the cross-section area $A = a \cdot b$ is given by $m = n \cdot I \cdot A = n \cdot I \cdot a \cdot b$, where I is the current through the coil. In our case ($n = 20$, $I = 20$ mA) we get a magnetization

$$M = \frac{m}{a \cdot b \cdot c} = \frac{n \cdot I}{c} = 20 \ \frac{\mathrm{A}}{\mathrm{m}} \ . \tag{C.1}$$

For the simulation only the inner mu-metal layer of the BMSR-2 shielding was considered, with the dimensions (3208 x 3208 x 3224) mm^3, the thickness $d = 4$ mm and the relative magnetic permeability $\mu_r = 13000$ [12]. Outgoing from the Helmholtz condition for quadratical coils ($d \approx a/1.837$ [42]), the distance d between the coils was varied. The best distance was found to be at $d = 97$ cm, quite near to the Helmholtz distance of ≈ 98 cm. The reason for the approximate agreement lies in the mu-metal shielding that slightly changes the field characteristics.

During the measurements described in Chap. 3 and 4, the center of the 6 cm diameter measurement cell was positioned at (0, 0, -6.6 cm), where the coordinate origin (0, 0, 0) corresponds to the center of the shielding. So this is the region where the field should be most homogeneous. For symmetry reasons it would have been better to center the cell as well as the coils also in the z-direction, but this was not possible due to the dimensions of the Dewar which was already shifted up to its highest position. Without the mu-metal the best position for the coil center would be identical with the cell center, i.e., at (0, 0, -6.6 cm). However, if one considers the mu-metal, which serves as mirror for the magnetic field lines, this simple fact does no longer hold. For this reason the z-position for the coils was varied to find the optimum distance Δz between the coil center and the center of the shielding (in the x- and y-direction the coils were centered). A good field homogeneity was found for $\Delta z = -2$ cm.

In Fig. C.1 the simulated field distribution relative to the field at the cell center $\vec{B}_{\mathrm{cc}} = (401.923\ \mathrm{nT}, 0.612\ \mathrm{pT}, -0.385\ \mathrm{pT})$ is shown. From left to right, the three components ΔB_{x}, ΔB_{y} and ΔB_{z} are plotted, first against y and z at x = 0 (upper row), then against x and z at y = 0 (mean row), and against y and x at z = -6.6 cm (lower row). The 6 cm diameter measurement cell around (0, 0, -6.6 cm) is marked with a black circle. One can see that the field difference over the size of the cell is less then 1 pT for ΔB_{y} at x = 0 and y = 0, and for ΔB_{z} at x = 0. For $\Delta B_{\mathrm{y,z}}$ at z = -6.6 cm, for ΔB_{z} at y = 0 and for ΔB_{x} the field difference is still less than 20 pT over the size of the cell. For the gradient this means that all components $\frac{\partial B_{\mathrm{x}}}{\partial x,y,z}$, $\frac{\partial B_{\mathrm{y}}}{\partial x,y,z}$ and $\frac{\partial B_{\mathrm{z}}}{\partial x,y,z}$ are smaller than 4 pT/cm.

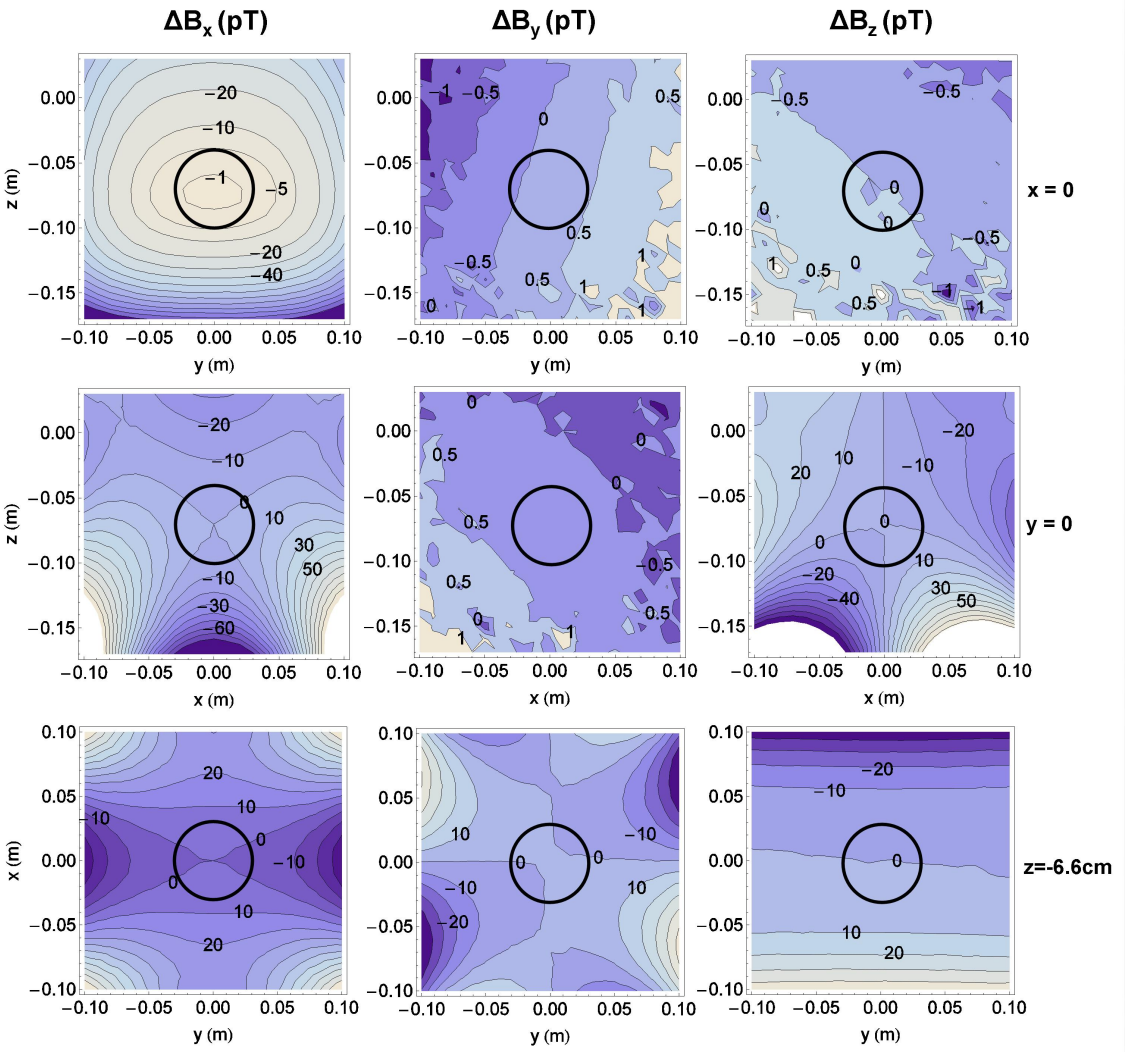

Figure C.1: Relative field distribution (in pT) of the simulated field of the B_{x}-coils inside the BMSR-2, referred to the field at the cell center $\vec{B_{\mathrm{cc}}} = (401.923\ \mathrm{nT}, 0.612\ \mathrm{pT}, -0.385\ \mathrm{pT})$. The position of the measurement cell around (0, 0, -6.6 cm) is marked with a black circle. *From left to right:* Relative field components ΔB_{x}, ΔB_{y} and ΔB_{z}. *Upper row*: Field dependence of y and z at x = 0. *Mean row*: Field dependence of x and z at y = 0. *Lower row:* Field dependence of y and x at z = -6.6 cm. The coils are centered in x- and y-direction, while in z-direction they are shifted 2 cm below the center of the shielding.

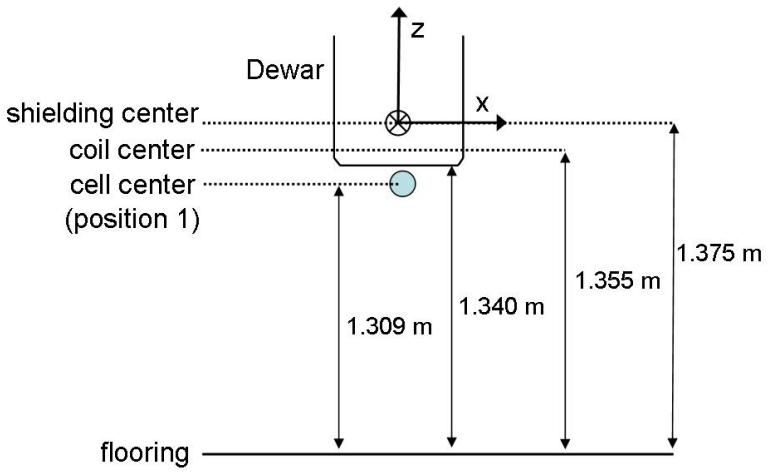

Figure C.2: Position of the Dewar, the center of the mu-metal shielding, the center of the B_x-coils and the cell relative to the flooring during the measurements in February 2009. The zero-point of the coordinate system used for the measurements lies in the center of the shielding.

C.2 Field measurements in February 2009

In February 2009, some weeks before the clock-comparison experiments, the magnitude $B(\vec{r}) = |\vec{B}(\vec{r})|$ of the magnetic field produced by the B_x-coils inside the BMSR-2 (see Fig. 3.6) was measured. Therefore the coils as well as the Dewar were centered in the x- and y-direction, while in the z-direction the coil center was shifted 2 cm below the center of the shielding[1]. The positions of the coil center, the Dewar and the cell are shown in Fig. C.2. The measurement was done with the help of a spherical cell (Z92, diameter 6 cm) filled with spin polarized ^{129}Xe, together with ^{4}He which served as buffer gas, at a total pressure of ≈ 360 mbar ($[^{129}\text{Xe}]/[^4\text{He}] \approx 1:1$). The magnitude of the magnetic field was determined out of the ^{129}Xe Larmor precession frequency ν_{xe} via

$$B = \frac{2\pi\nu_{\text{xe}}}{\gamma_{\text{xe}}} \,, \tag{C.2}$$

where γ_{xe} is the gyromagnetic ratio. The measurement was done at 2 different heights, $z = -6.6$ cm (position 1 in Fig. C.2) and $z = -8.7$ cm, where the coordinate origin (0, 0, 0) corresponds to the center of the shielding. To change the height to $z = -8.7$ cm the cell holder was screwed down relative to the Dewar, while the Dewar remained fixed, i.e., the cell

[1]Here the center of the mu-metal shielding is meant, which is not equal to the room center, because of the thickness of the flooring of 7 cm.

	$y \downarrow \quad x \rightarrow$	-5 cm	0	+5 cm	
z=-6.6 cm	10.210 cm	4.0276E-07		4.02876E-07	$\leftarrow B$ (T)
	6.495 cm		4.0282E-07		$\leftarrow B$ (T)
	2.165 cm	4.0275E-07		4.02838E-07	$\leftarrow B$ (T)
z=-8.7 cm	10.210 cm	4.0282E-07		4.02934E-07	$\leftarrow B$ (T)
	6.495 cm		4.0283E-07		$\leftarrow B$ (T)
	2.165 cm	4.0282E-07		4.02938E-07	$\leftarrow B$ (T)

Table C.1: Field values measured with a 6-cm ^{129}Xe cell

was shifted away from the Dewar, and at the same time away from the most homogeneous region of the magnetic field. For each z-position, the cell was shifted to 5 different positions in the x-y plane (see Fig. C.3). The measured field magnitudes for the different positions are listed in Tab. C.1. The gradient component $G_{\mathrm{i,j}}$ for the region between two measurement points $\vec{r}_{\mathrm{i}}$ and $\vec{r}_{\mathrm{j}}$ was calculated by building the difference between the two corresponding field values, divided by the distance between these points, i.e.,

$$G_{\mathrm{i,j}} = \frac{|B(\vec{r}_{\mathrm{i}}) - B(\vec{r}_{\mathrm{j}})|}{|\vec{r}_{\mathrm{i}} - \vec{r}_{\mathrm{j}}|} \ , \tag{C.3}$$

where the vector $\vec{r}_{\mathrm{i(j)}}$ points to the cell center. The results are shown in Fig. C.3: The light blue circles A, B, C, etc. are the SQUID modules. The zero-point of the coordinate system lies in the middle of the K module, which sits in the center of the Dewar. The dark blue dots mark the measurement positions, and the number in the white circle gives the gradient in pT/cm between the corresponding measurement points. The first two pictures show the gradients in the x-y-plane for $z = -6.6$ cm (upper picture) and $z = -8.7$ cm (middle picture). In the lower picture the gradients in z-direction between these two levels, i.e., for $z = -7.65$ cm are plotted. For the level $z = -6.6$ cm, the measured gradients in the x-y-plane are between 1.1 and 11.5 pT/cm, while for $z = -8.7$ cm they are between 0.6 and 17.2 pT/cm. The biggest field inhomogeneity we have in the z-direction (lower picture), where values between 2.3 and 47.8 pT/cm were measured. From these measurements it can be seen that the gradients are in reality much bigger than in the simulation, and show large irregularities. The reason for this could be an incorrect alignment of the coils, as well as additional fields produced by the Dewar that was slightly magnetized. For future measurements it is important to optimize the alignment and the z-position of the coils, and to demagnetize the Dewar as good as possible.

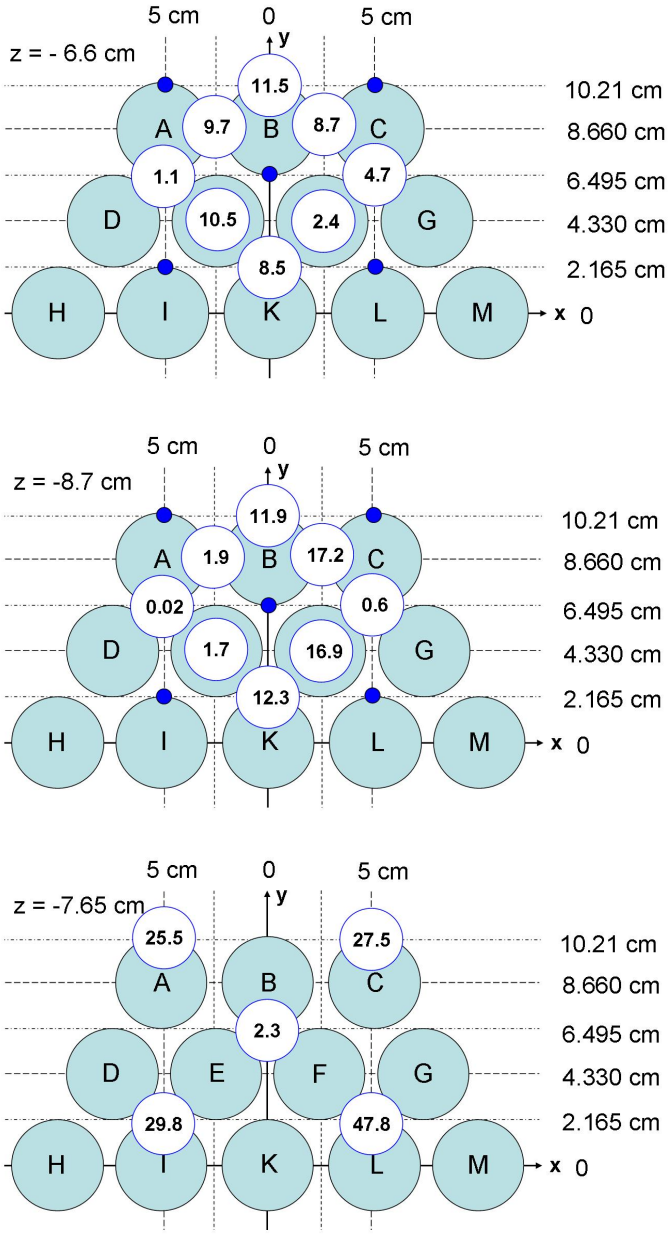

Figure C.3: Gradients in pT/cm of the field produced by the B_x-coils inside the BMSR-2, measured with a 6-cm-diameter cell filled with polarized ^{129}Xe. The light blue circles that are named A, B, C, etc. are the SQUID modules. The zero-point of the coordinate system is the center of the mu-metal shielding. The dark blue dots mark the measurement positions, and the number in the white circle gives the gradient in pT/cm between the corresponding measurement points. The upper picture shows the gradients for $z = -6.6$ cm, the middle one the gradients for $z = -8.7$ cm. In the lower picture the gradients between these two levels, i.e., for $z = -7.65$ cm are plotted.

Bibliography

[1] I. Altarev et al. Towards a new measurement of the neutron electric dipole moment. *Nucl. Instr. and Meth. in Phys. Res. A*, 611(2-3):133 – 136, 2009. doi:10.1016/j.nima.2009.07.046.

[2] C. Amsler et al. *Phys. Lett. B*, 667(1), 2008.

[3] S. Appelt et al. Theory of spin-exchange optical pumping of ^{3}He and ^{129}Xe. *Phys. Rev. A*, 58(2):1412–1439, 1998.

[4] J. C. Baez. Higher-dimensional algebra and planck scale physics. In C. Callender and N. Huggett, editors, *Physics meets philosophy at the Planck scale*. Cambridge University Press, 2001.

[5] D. Bear et al. Improved frequency stability of the dual-noble-gas maser. *Phys. Rev. A*, 57(6), 1998.

[6] D. Bear, R. E. Stoner, R. L. Walsworth, V. A. Kostelecký, and C. D. Lane. Erratum: Limit on Lorentz and CPT Violation of the Neutron Using a Two-Species Noble-Gas Maser. *Phys. Rev. Lett.*, 89(20), 2002.

[7] D. Bear, R. E. Stoner, R. L. Walsworth, V. Alan Kostelecký, and C. D. Lane. Limit on Lorentz and CPT Violation of the Neutron Using a Two-Species Noble-Gas Maser. *Phys. Rev. Lett.*, 85(24):5038–5041, 2000.

[8] D. C. Bear. *Fundamental Symmetry Tests Using a $^{129}Xe/^3He$ Dual Noble Gas Maser*. PhD thesis, Harvard University Cambridge, 2000.

[9] G. Bison, U. Schläpfer, G. Di Domenico, H. Saudan, and A. Weis. A new optical magnetometer for MCG measurements in a low-cost shielding room. *International Congress Series*, 1300:561 – 564. Proceedings of the 15th International Conference on Biomagnetism, Vancouver, Canada, 2006. doi:10.1016/j.ics.2007.02.039.

[10] C. Bizouard. IERS: International Earth Rotation and Reference Systems Service. Available from: `http://hpiers.obspm.fr/eop-pc/models/constants.html` [cited Nov. 08, 2010].

[11] F. Bloch and A. Siegert. Magnetic Resonance for Nonrotating Fields. *Phys. Rev.*, 57(6), 1940. `doi:10.1103/PhysRev.57.522`.

[12] J. Bork, H.-D. Hahlbohm, R. Klein, and A. Schnabel. The 8-layered magnetically shielded room of the PTB: design and construction. *Biomag2000; Proceedings, 12th International Conference on Biomagnetism, Helsinki*, pages 970–973, 2000.

[13] S. R. Breeze et al. Coatings for optical pumping cells and extending the lifetime of hyperpolarized xenon. *J. of Appl. Phys.*, 86(7), 1999.

[14] J. M. Brown, S. J. Smullin, T. W. Kornack, and M. V. Romalis. New Limit on Lorentz- and CPT-Violating Neutron Spin Interactions. *Phys. Rev. Lett.*, 105(15), 2010. `doi:10.1103/PhysRevLett.105.151604`.

[15] F. Canè et al. Bound on Lorentz and CPT Violating Boost Effects for the Neutron. *Phys. Rev. Lett.*, 93(23):230801, 2004. `doi:10.1103/PhysRevLett.93.230801`.

[16] G. D. Cates, S. R. Schaefer, and W. Happer. Relaxation of spins due to field inhomogeneities in gaseous samples at low magnetic fields and low pressure. *Phys. Rev. A*, 37, 1988.

[17] G. D. Cates, D. J. White, T. Chien, S. R. Schaefer, and W. Happer. Spin relaxation due to inhomogeneous static and oscillating magnetic fields. *Phys. Rev. A*, 38, 1988.

[18] B. Chann, I. A. Nelson, L. W. Anderson, B. Driehuys, and T. G. Walker. ^{129}Xe-Xe Molecular Spin Relaxation. *Phys. Rev. Lett.*, 88(11), 2002. `doi:10.1103/PhysRevLett.88.113201`.

[19] C. Cohen-Tannoudji, J. DuPont-Roc, S. Haroche, and F. Laloë. Detection of the Static Magnetic Field Produced by the Oriented Nuclei of Optically Pumped ^{3}He Gas. *Phys. Rev. Lett.*, 22(15):758–760, 1969.

[20] Online coordinate converter. Available from: `http://www.roman-britain.org/astronomy/astro.htm` [cited Nov. 08, 2010].

[21] E. Coutarde. *Pompage optique de l'hélium dans des conditions non-standard.* PhD thesis, École Normale Supérieure Paris (France), 2001.

[22] H. B. Dang, A. C. Maloof, and M. V. Romalis. Ultra-high sensitivity magnetic field and magnetization measurements with an atomic magnetometer. 2009. Available from: `http://arxiv.org/abs/0910.2206v1`.

[23] A. Deninger et al. Paramagnetic relaxation of spin polarized ^{3}He at coated glass walls. *Eur. Phys. J. D*, 38:439 – 443, 2006. Available from: `http://dx.doi.org/10.1140/epjd/e2006-00051-1`.

[24] R. W. P. Drever. A search for anisotropy of inertial mass using a free precession technique. *Philosophical Magazine*, 6(65), 1961. `doi:10.1080/14786436108244418`.

[25] A. Fink, D. Baumer, and E. Brunner. Production of hyperpolarized xenon in a static pump cell: Numerical simulations and experiments. *Phys. Rev. A*, 72(5):053411, 2005. `doi:10.1103/PhysRevA.72.053411`.

[26] C. Gemmel. *Voruntersuchungen zu Lorentzinvarianz-Tests mit Hilfe eines ^{3}He-Magnetometers*. Dipl. thesis, Universität Mainz, 2006.

[27] C. Gemmel et al. Ultra-sensitive magnetometry based on free precession of nuclear spins. *Eur. Phys. J. D*, 57(3):303–320, 2010. `doi:10.1140/epjd/e2010-00044-5`.

[28] K. C. Hasson et al. Spin relaxation due to magnetic-field inhomogeneities: Quartic dependence and diffusion-constant measurements. *Phys. Rev. A*, 41(7):3672–3688, 1990.

[29] S. Hawking. *Das Universum in der Nußschale*. Hoffmann und Campe, 2001.

[30] B. R. Heckel et al. Preferred-frame and CP-violation tests with polarized electrons. *Phys. Rev. D*, 78(9):092006, 2008. `doi:10.1103/PhysRevD.78.092006`.

[31] S. Herrmann et al. Rotating optical cavity experiment testing Lorentz invariance at the 10^{-17} level. *Phys. Rev. D*, 80(10), 2009. `doi:10.1103/PhysRevD.80.105011`.

[32] S. Hiebel et al. Magnetized boxes for housing polarized spins in homogeneous fields. *J. of Magn. Res.*, 204(1), 2010. Available from: `http://www.sciencedirect.com/science/article/B6WJX-4YCWNP1-1/2/01cb25aa5692c37766e956c272bfea72`.

[33] R. E. Hoffman and E. D. Becker. Temperature dependence of the ^{1}H chemical shift of tetramethylsilane in chloroform, methanol, and dimethylsulfoxide. *J. of Magn. Res.*, 176(1):87 – 98, 2005.

[34] D. M. Hopstock. A reexamination of the performance of demagnetizing coils on finely ground natural magnetite. *Int. J. Miner. Process.*, 59:45–68, 1999.

[35] V. W. Hughes, H. G. Robinson, and V. Beltran-Lopez. Upper limit for the anisotropy of inertial mass from nuclear resonance experiments. *Phys. Rev. Lett.*, 4(7), 1960.

[36] E. R. Hunt and H. Y. Carr. Nuclear Magnetic Resonance of ^{129}Xe in Natural Xenon. *Phys. Rev.*, 130(6), 1963. doi:10.1103/PhysRev.130.2302.

[37] J. D. Jackson. *Classical Electrodynamics*. John Wiley and Sons, 1998.

[38] C.J. Jameson, A.K. Jameson, and H. Parker. *J. Chem. Phys.*, 8(68), 1978.

[39] S. M. Kay. *Fundamentals of Statistical Signal Processing*. Prentice Hall PTR, 1993.

[40] W. Kilian. *Erzeugung von hyperpolarisiertem ^{129}Xe-Gas und Nachweis mittels in vivo NMR-Bildgebung, NMR-Spektroskopie sowie SQUID-Messtechnik*. PhD thesis, Freie Universität Berlin, 2001.

[41] S. Knappe. *Optimierte SQUID-Sensoren für Anwendungen in zerstörungsfreier Werkstoffprüfung, Umweltgeophysik und Biomagnetismus*. PhD thesis, Universität Hamburg, 1998.

[42] V. Kniese. *Polarisation und Relaxation eines polarisierten ^{3}He-Targets im Elektronenstrahl*. Dipl. thesis, Universität Mainz, 1992.

[43] T. W. Kornack. *A test of CPT and Lorentz Symmetry Using a K-3He Comagnetometer*. PhD thesis, Princeton University, 2005.

[44] V. A. Kostelecký and C. D. Lane. Constraints on Lorentz violation from clock-comparison experiments. *Phys. Rev. D*, 60(11):116010, 1999.

[45] V. A. Kostelecký and N. Russell. Data Tables for Lorentz and CPT Violation. January 2010. Available from: http://arxiv.org/abs/0801.0287v3.

[46] V. A. Kostelecký and S. Samuel. Spontaneous breaking of Lorentz symmetry in string theory. *Phys. Rev. D*, 39(2):683 – 685, 1989. doi:10.1103/PhysRevD.39.683.

[47] W. Lorenzon, T. R. Gentile, H. Gao, and R. D. McKeown. NMR calibration of optical measurement of nuclear polarization in ^{3}He. *Phys. Rev. A*, 47(1):468–479, 1993.

[48] C. Ludwig. *Voruntersuchungen zu Lorentzinvarianz-Tests mit Hilfe eines ^{3}He-^{129}Xe-Komagnetometers*. Dipl. thesis, Universität Mainz, 2008.

[49] B.R. Martin and G. Shaw. *Particle Physics*. Wiley, 2002.

[50] Stuart L. Meyer. *Data Analysis for Scientists and Engineers*. John Wiley & Sons, 1975.

[51] A. A. Michelson and E. W. Morley. On the relative motion of the earth and the luminiferous Æther. *Philosophical Magazine Series*, 5(24), 1887.

[52] A. E. Morbach. *Diffusionsgewichtete Helium-3 Magnetresonanztomographie zur Untersuchung der Lunge*. PhD thesis, Universität Mainz, 2006.

[53] P.J. Nacher and M. Leduc. Optical pumping in ^{3}He with a laser. *J. Physique*, 46:2057–2073, 1985.

[54] NASA. HEASARC: NASA's High Energy Astrophysics Science Archive Research Center. Available from: `http://heasarc.gsfc.nasa.gov/` [cited Nov. 08, 2010].

[55] J. W. Negele and E. W. Vogt. *Advances in Nuclear Physics*, volume 27. Springer, 2003.

[56] N. R. Newbury, A. S. Barton, G. D. Cates, W. Happer, and H. Middleton. Gaseous ^{3}He-^{3}He magnetic dipolar spin relaxation. *Phys. Rev. A*, 48(6), 1993. `doi:10.1103/PhysRevA.48.4411`.

[57] NIST (National Institute of Standards and Technology). Latest (2006) values of the constants. Available from: `http://physics.nist.gov/cuu/constants/` [cited Nov. 08, 2010].

[58] D. K. Robinson P. R. Bevington. *Data Reduction and Error Analysis for the Physical Sciences*. McGraw-Hill, 2003.

[59] L. A. Pedrós. *Diffusion of laser polarized gases in MRI*. PhD thesis, Universität Mainz, 2007.

[60] M. Pfeffer and O. Lutz. ^{129}Xe Gas NMR Spectroscopy and Imaging with a Whole-Body Imager. *Journal of Magnetic Resonance A*, 108:106–109, 1994.

[61] A. Pich. Effective field theory. Available from: `http://arxiv.org/abs/hep-ph/9806303v1`.

[62] W. H. Press. *Numerical Recipes in C++: the art of scientific computing*. Cambridge University Press, 2003.

[63] D. Raftery et al. Spin-polarized ^{129}Xe NMR study of a polymer surface. *J. Phys. Chem.*, 97(8), 1993.

[64] N. F. Ramsey. A New Molecular Beam Resonance Method. *Phys. Rev.*, 76(7):996, 1949. doi:10.1103/PhysRev.76.996.

[65] S. D. Rosner and F. M. Pipkin. Hyperfine Structure of the 2^3S_1 state of ^{3}He. *Phys. Rev. A*, 1:571–586, 1970.

[66] J. Schmiedeskamp et al. Paramagnetic relaxation of spin polarized ^{3}He at bare glass surfaces. *Eur. Phys. J. D*, 38:427 – 438, 2006. Available from: http://dx.doi.org/10.1140/epjd/e2006-00050-2.

[67] J. Schmiedeskamp et al. Paramagnetic relaxation of spin polarized ^{3}He by magnetized ferromagnetic contaminants. *Eur. Phys. J. D*, 38:445 – 454, 2006. Available from: http://dx.doi.org/10.1140/epjd/e2006-00052-0.

[68] F. Schwabl. *Quantenmechanik*. Springer, 2004.

[69] N. Segebarth et al. Novel Method for the Measurement of Xenon Gas Solubility Using ^{129}Xe NMR Spectroscopy. *J. Phys. Chem. A*, 110:10770–10776, 2006.

[70] C. P. Slichter. *Principles of Magnetic Resonance*. Springer, 1978.

[71] L. Smolin. An invitation to Loop Quantum Gravity. 2005. Available from: http://arxiv.org/abs/hep-th/0408048v3.

[72] G. F. Smoot and D. Scott. Cosmic background radiation. *Eur. Phys. J. C*, 15(1-4), 2000. doi:10.1007/BF02683415.

[73] Daniel Sudarsky, Luis Urrutia, and Héctor Vucetich. Observational Bounds on Quantum Gravity Signals using Existing Data. *Phys. Rev. Lett.*, 89(23), 2002. doi:10.1103/PhysRevLett.89.231301.

[74] The United States Naval Observatory. Naval Oceanography Portal. Available from: http://www.usno.navy.mil/USNO/astronomical-applications/astronomical-information-center/approx-sider-time [cited Nov. 08, 2010].

[75] F. Thiel, A. Schnabel, S. Knappe-Grüneberg, D. Stollfuss, and M. Burghoff. Demagnetization of magnetically shielded rooms. *Review of Scientific Instruments*, 78:035106, 2007.

[76] B. Tschumy. The Galactic Coordinate System. Available from: http://www.thinkastronomy.com/M13/Manual/common/galactic_coords.html [cited Nov. 08, 2010].

[77] K. Tullney. *Test der Lorentzinvarianz mit Hilfe eines ^{3}He-^{129}Xe-Komagnetometers.* Dipl. thesis, Universität Mainz, 2009.

[78] University of Colorado at Boulder. CASA: Center for Astrophysics and Space Astronomy. Available from: `http://casa.colorado.edu/` [cited Nov. 08, 2010].

[79] B. Vatant. Find latitude and longitude with google maps. Available from: `http://pagesperso-orange.fr/universimmedia/geo/loc.htm` [cited Nov. 08, 2010].

[80] H. Vucetich. Testing Lorentz Invariance Violation in Quantum Gravity Theories. 2005. Available from: `http://arxiv.org/abs/gr-qc/0502093v1`.

[81] J. H. Wesenberg and K. Mølmer. Field Inside a Random Distribution of Parallel Dipoles. *Phys. Rev. Lett.*, 93(14), 2004.

[82] Wikipedia. Galactic coordinates. Available from: `http://en.wikipedia.org/wiki/File:Galactic_coordinates.JPG` [cited Nov. 08, 2010].

[83] E. Wilms, M. Ebert, W. Heil, and R. Surkau. Polarimetry on dense samples of spin-polarized ^{3}He by magnetostatic detection. *Nucl. Instr. and Meth. A*, 401:491–498, 1997.

[84] M. Wolf. *Erzeugung höchster ^{3}He-Kernspinpolarisation durch metastabiles optisches Pumpen.* PhD thesis, Universität Mainz, 2004.